INAUGURAL-DISSERTATION

zur

Erlangung der Doktorwürde

der

Naturwissenschaftlich-Mathematischen Gesamtfakultät

der

Ruprecht-Karls-Universität

Heidelberg

vorgelegt von

M.Sc. Chemiker Hao Lu

aus Jilin, China

Tag der mündlichen Prüfung: 08.11.2013

A Study of Specific Factors Affecting Molecular Self-Assembly on GaAs (001) Substrate

Gutachter: Prof. Dr. Michael Zharnikov

Prof. Dr. Hans-Robert Volpp

Kurzfassung:

Motivation dieser Arbeit ist es, ein tieferes Verständnis von Struktur und Mechanismus molekularer Selbstorganisation organischer Thiole auf Galliumarsenid (GaAs)-Substraten zu erlangen. Dazu werden als Modellsystem selbstaggregierende Monolagen (SAMs) auf diesen technischen wichtigen GaAs-Halbleitern hergestellt. Als Adsorbatmoleküle zur Präparation hochgeordneter, dichtgepackter SAMs werden unsubstituierte, bi- und terphenylsubstituierte sowie teilweise fluorierte Alkanthiole auf einer GaAs(001)-Oberfläche verwendet. Die SAMs werden detailliert mittels oberflächensensitiver Techniken charakterisiert, um sowohl die molekulare Orientierung als auch die Eigenschaften dieser Filme zu untersuchen.

Zunächst wurde für alle untersuchten Systeme ein ausgeprägter Effekt der Kettenlänge der Adsorbatmoleküle auf die Qualität der Monolagen gefunden. Dieser äußerte sich in einer Verschlechterung der Packungsdichte mit abnehmender Länge der Molekülkette begleitet von einer partiellen Oxidation des GaAs-Substrats durch die verminderte Schutzwirkung des SAMs.

Ferner konnte anhand einer Serie bi-und terphenylsubstituierter Alkanthiole die Existenz eines Verformungspotentials (engl. *bending potential*) an der Grenzfläche von Kopfgruppen und Substrat nachgewiesen werden. Dabei ist die GaAs-S-C-Bindung bevorzugt unter einem Winkel von 104° ausgerichtet. Bei den oben genannten SAMs spielt das Verformungspotential in der Bilanz der strukturbildenden Kräfte eine dominierende Rolle und führt damit zur Ausbildung eines Odd-Even-Effekts bezüglich molekularer Orientierung und Packungsdichte. Dieses Ergebnis zeigt, dass das Verformungspotential bei der Herstellung funktionaler, molekularer Filme auf GaAs stets berücksichtig werden muss.

Der Einfluss der oben genannten Faktoren wie Kettenlängeneffekt und die Verformungspotential wird zusätzlich am Beispiel von zum Teil (partially) fluorierten Alkanthiol (PFAT) SAMs mit unterschiedlichen Längen der Fluorkohlenstoffkette untersucht $CF_3(CF_2)_{n-1}(CH_2)_{11}SH$ (FnH11SH, n= 6, 8, und 10). Zum besseren Verständnis der Struktur und Organisation der neuen Filme wurden zunächst entsprechende Studien an den PFAT/Au-Referenzmonolagen durchgeführt, um so eine Vielzahl wertvoller allgemeiner Erkenntnisse über das Gleichgewicht der strukturbildenden Wechselwirkungen in komplexen Systemen zu gewinnen. Wie bei dem PFAT/GaAs-System waren die entsprechende SAMs hochgeordnet und dichtgepackt und damit in der Lage, die GaAs-Oberfläche vor Oxidation zu schützen. Auch bei diesen SAMs war bei einer kürzeren Fluorkohlenstoffkette aufgrund einer geringeren Filmqualität der Schutz der Oberfläche vor Oxidation weniger wirksam. Ferner

wurde mit abnehmender Länge des Fluorkohlenstoffkette eine fortschreitende Verschlechterung der Orientierung und ein geringfügiger Rückgang in der Packungsdichte beobachtet. Im Gegensatz dazu zeigten die Kohlenwasserstoff-Segmente in FnH11SH/GaAs ähnlicher Ausrichtung, mit einem durchschnittlichen Tiltwinkel nahe am Optimum einer durch das Verformungspotential bestimmt. Dies unterstreicht einmal mehr die wichtige Rolle des Verformungspotentials in der Bilanz der strukturbildenden Wechselwirkungen in aliphatischen SAMs auf GaAs.

Abstract:

The major goal of this thesis is to gain a better understanding of the molecular self-assembly on GaAs, which can be useful for design of functional self-assembled monolayers (SAMs) on this technologically important semiconductor substrate. For this purpose, high quality SAMs of non-substituted alkanethiols and some specially designed molecules, including 4,4´-terphenyl-substituted alkanethiols, ω-(4´-methyl-biphenyl-4-yl)-alkanethiols, partially fluorinated alkanethiols (PFAT), and dihexadecyl diselenide have been prepared on GaAs (001) through the optimization and careful control of the rigorous experimental conditions. These SAMs were investigated in detail by a combination of advanced surface characterization techniques, providing a deep insight into the molecular organization and properties of these films.

In the first place, pronounced chain length effect for all studied SAM systems on GaAs was elucidated, viz. deterioration of the film quality occurs with decreasing length of the molecular chain, accompanied by a partial oxidation of the GaAs substrate, due to the less effective protection property.

In the second place, by using the series of the 4,4´-terphenyl-substituted alkanethiols and ω-(4´-methyl-biphenyl-4-yl)-alkanethiols, the existence of so called bending potential at the headgroup-substrate interface in the SAM/GaAs(001) system with a preferable GaAs-S-C angle of ~104° was demonstrated. For the above SAMs, this potential plays the dominant role in the balance of the structure-building forces, mediating the odd-even behavior in the molecular orientation and packing density. This result suggests that the bending potential should always be taken into account at the design of functional molecular films on GaAs substrate.

The influence of the above factors, viz. the chain length effect and the bending potential, were additionally studied by the example of PFAT SAMs with variable length of the fluorocarbon chain, viz. $CF_3(CF_2)_{n-1}(CH_2)_{11}SH$ (denoted as FnH11SH, n = 6, 8, and 10). To better understand the structure and organization of these films, the corresponding study of the reference PFAT/Au system was performed first, resulting in a variety of valuable general findings regarding the balance of the structure-building interactions in complex monomolecular films. As for the PFAT/GaAs system, the respective SAMs were found to be highly ordered and densely packed, and consequently able to protect the GaAs surface from

the oxidation. This protection depended on the chain length and was less effective for the films with shorter fluorocarbon chain due to their lower quality. Indeed, with decreasing length of the fluorocarbon segment, progressive deterioration of the orientation order accompanied by a slight decrease in the packing density was observed in the fluorocarbon part. In contrast, the hydrocarbon segments in FnH11SH/GaAs exhibited similar orientation, with the average tilt angles close to the optimum one determined by the bending potential. This underlines once more the important role of bending potential in the balance of structure-building interactions in aliphatic SAMs on GaAs.

Contents

Chapter 1: Introduction - 1 -
Chapter 2: Basic Theory - 9 -
2.1 X-ray Photoelectron Spectroscopy (XPS) - 9 -
2.1.1 Elemental specificity - 9 -
2.1.2 Surface sensitivity of XPS - 10 -
2.1.3 Attenuation length - 10 -
2.1.4 Intensity of the XPS signal and thickness calculation - 11 -
2.1.5 Enhancing the surface sensitivity - 11 -
2.2 Near Edge X-ray Absorption Fine Structure (NEXAFS) spectroscopy - 13 -
2.2.1 Basic principles - 13 -
2.2.2 Angular dependence of the NEXAFS signal - 14 -
2.3 InfraRed Reflection Absorption Spectroscopy (IRRAS) - 15 -
2.4 Ellipsometry - 15 -
2.5 Contact angle goniometry - 16 -
2.5.1 Basic Principle - 16 -
2.5.2 Advancing and static contact angle - 16 -
Chapter 3: Experimental Parts - 17 -
3.1 Substrates - 17 -
3.2 Chemicals - 17 -
3.3 SAM preparation on GaAs (001) - 18 -
3.3.1 NSAT SAMs: - 18 -
3.3.2 TPn and BPn SAMs: - 18 -
3.3.3 PFAT (FnH11SH) SAMs: - 19 -
3.3.4 C16Se SAM: - 19 -
3.4 SAM preparation on Au (111) - 19 -
3.4.1 NSAT SAMs: - 19 -
3.4.2 TPn SAMs: - 19 -
3.4.3 PFAT (FnH11SH) SAMs: - 19 -
3.5 SAM characterization - 20 -
3.5.1 XPS (Max-200) - 20 -
3.5.2 High Resolution X-ray Photoelectron Spectroscopy (HRXPS) - 21 -
3.5.3 NEXAFS spectroscopy - 22 -
3.5.4 InfraRed (IR) spectroscopy - 23 -
3.5.5 Ellipsometry - 24 -

3.5.6 Contact angle measurement - 24 -
3.5.7 Atomic Force Microscope (AFM) - 24 -
Chapter 4: SAMs of Non-Substituted Alkanethiols on GaAs (001) - 25 -
4.1 ODT SAM - 25 -
4.1.1 HRXPS - 25 -
4.1.2 NEXAFS spectroscopy - 29 -
4.1.3 IRRAS - 31 -
4.1.4 Ellipsometry: monolayer thickness - 32 -
4.1.5 Contact angle: monolayer wetting property - 32 -
4.2 HDT SAM: comparable film quality with ODT SAM - 33 -
4.3 DDT SAM - 35 -
4.3.1 Film quality of DDT SAM - 35 -
4.3.2 Optimizing preparation procedure for DDT SAM - 36 -
4.4 Discussion - 37 -
4.4.1 As-S bonding - 37 -
4.4.2 Chain length dependence of the film quality - 38 -
Chapter 5: TPn and BPn SAMs on GaAs (001) - 41 -
5.1 TPn SAMs - 41 -
5.1.1 Optimization of the preparation procedure for TPn/GaAs SAMs - 41 -
5.1.2 Spectroscopy characterization of TPn SAMs: HRXPS - 44 -
5.1.3 Spectroscopy characterization of TPn SAMs: NEXAFS spectroscopy - 47 -
5.1.4 Probing the twist angle for TPn SAMs using TP1-CN SAM - 51 -
5.1.5 Odd-even effect for TPn SAMs - 54 -
5.1.6 Odd-even effect for TPn SAMs on Au (111) - 56 -
5.1.7 Discussion of TPn SAMs - 57 -
5.2 BPn SAMs - 59 -
5.2.1 Spectroscopy characterization of BPn SAMs: HRXPS - 59 -
5.2.2 Spectroscopy characterization of BPn SAMs: NEXAFS spectroscopy - 61 -
5.2.3 Odd-even effect for BPn SAMs - 63 -
5.2.4 Discussion of BPn SAMs - 64 -
Chapter 6: Structure of SAMs of Partially Fluorinated Alkanethiols with a Fluorocarbon Part of variable Length on Au (111) - 67 -
6.1 Results - 68 -
6.1.1 HRXPS - 68 -
6.1.2 XPS: Film thickness and packing density - 71 -
6.1.3 IRRAS - 72 -

6.1.4 NEXAFS spectroscopy - 76 -
6.2 Discussion - 81 -
Chapter 7: Structure of Self-Assembled Monolayers of Partially Fluorinated Alkanethiols on GaAs (001) substrate - 85 -
7.1 Results - 85 -
7.1.1 HRXPS and XPS - 85 -
7.1.2 IRRAS - 90 -
7.1.3 NEXAFS spectroscopy - 92 -
7.2 Discussion - 97 -
Chapter 8: SAM of Non-substituted Alkaneselenolate on GaAs (001) - 101 -
8.1 Results - 102 -
8.1.1 HRXPS - 102 -
8.1.2 NEXAFS spectroscopy - 104 -
8.1.3 Contact Angle Measurements - 105 -
8.2 Discussion - 106 -
Chapter 9: Conclusion - 109 -
Bibliography - 113 -
Appendix - 129 -
A1: Synthesis of the FnH11SH compounds - 129 -
A2: Additional IR dataset for FnH11SH SAMs on Au - 132 -
A3: Abbreviations - 135 -
A4: List of Figures - 136 -
A5: List of Tables - 140 -
A6: List of Publications in PhD Period - 141 -
Acknowledgement - 143 -

Chapter 1: Introduction

Control and adjustment of surface and interfacial properties on microscopic and macroscopic length scales are important scientific and technological issues. An efficient approach in this regard is surface functionalization with specifically designed monomolecular films, denoted usually as self-assembled monolayers (SAMs).[1,2] These films represent 2D polycrystalline assemblies of semi-rigid, rod-like molecules that are chemically anchored to the substrate.[1-6]

Typical SAM precursors can be divided into three essential parts: the headgroup (anchoring moiety), molecular backbone (spacer), and specific terminal (tail) group. The headgroup guides the self-assembly process on a solid support, binding the molecule to the substrate surface through a specific bond. The interactions between the molecular chains mediated by the van der Waals, hydrophobic, and electrostatic forces ensures an efficient packing of the monolayer and stabilizes its structure. The terminal group confers specific properties to the surface such as the wetting properties, protein repelling, etc.; it can also be used to link different moieties, in particular biomolecules by weak interactions or covalent bonds.[6]

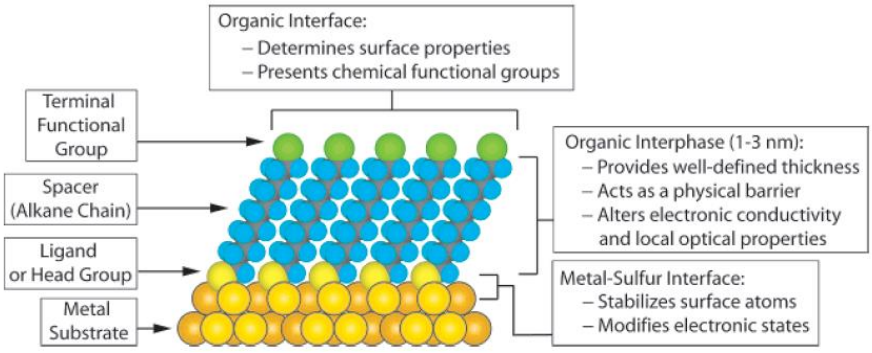

Figure 1.1: Schematic diagram of an ideal, single-crystalline SAM of alkanethiolates supported on a gold surface with a (111) texture. The anatomy and characteristics of the SAM are highlighted. The Figure is taken from Love *et al.*[6]

The flexibility of the SAM design and the possibility to prepare such films on almost any substrate result in a variety of applications, such as tailoring surface properties (wetting, adhesion, lubrication, corrosion, and biocompatibility), sensor fabrication, molecular and organic electronics, as well as conventional and chemical lithography.[6] Among different kinds

of SAMs, the most popular systems are alkanethiolates on coinage metal substrates, such as Au(111), Ag(111), and Cu(111),[1-7] mainly due to the well established preparation route and the versatility of the molecular design.[6] Figure 1.1 shows a schematic diagram of a densely packed alkanethiolate SAM on Au (111); the different building blocks as well as their functions are highlighted.

The packing density and structure of SAMs are generally determined by a complex interplay of a variety of factors which include intermolecular interaction, strength of the headgroup-substrate bond, corrugation of the binding energy hypersurface, and mismatch between the optimal molecular lattice and the substrate.[2] It was generally believed that in many SAMs, in particular, in SAMs of alkanethiols (ATs) on the Au (111) and Ag (111) substrates, intermolecular interaction plays a predominant role.[2,3,7,8] The substrate was assumed to affect only the packing density of alkanethiol (AT) moieties, through a corrugation of the sulfur-metal binding energy surface,[2,3,8] which results in an incommensurate structure for the thiolate head groups on Ag with a lattice constant of ~4.67 – 4.77 Å in the case of the weak corrugation, and in a commensurate lattice with a larger intersite spacing of ~5.0 Å on Au in the case of the strong corrugation.[2,3,8] The proposed predominant role of the intermolecular interaction is then primarily reflected in the different orientation of the AT molecules on Au and Ag, with tilt angles of 10 – 12° and 27 – 35°, respectively.[2,3,6-13] The substrate-S-C unit is assumed to behave as a "free joint", enabling a necessary tilt of the alkyl chains to achieve their most effective arrangement with an optimal bulk-like chain-chain spacing of ~4.4 Å.[2,14] (the chain-chain spacing is equal to the 2D-lattice constant multiplied by the cosine of the respective tilt angle)

In contrast to the "free joint" model, which as mentioned above assumes that the metal-S-C joint can take any orientation driven by the intermolecular interaction, a different model, assuming the existence of a strong bending potential at the headgroup in AT SAM on coinage metal substrates was derived. Within this model, the bending potential of the anchoring group is believed to be one of the dominant factors determining the molecular orientation and structure of AT SAMs. Unambiguous proofs are in particular so called odd-even effects in phenyl-,[15] methyl-terminated biphenyl-,[16-20] and terphenyl-[21-23] substituted AT SAMs. In these films, the packing density and orientation of the SAM constituents exhibit obvious odd-even variation rather than a simple persistence with varying number of the methylene units in the alkyl linker. Higher packing density, associated with smaller inclination of the SAM constituents, is observed for the SAMs with odd (even) number of methylene units on Au

(Ag) substrate. As an example, the schematic drawing of the odd-even behavior in terphenyl-substituted AT SAMs is illustrated in Figure 1.2. The observed odd-even effects in these films were explained by the substrate-dependent bending potential, which favors a certain bond angle of the substrate-S (Se)-C joint, determining the orientation of the alkyl chains and consequently the structure of the SAMs.[16-23] This angle depends on the substrate, and is ~104° and ~180° for Au (111) and Ag (111), respectively.[16,17,24,25] In addition, it should be mentioned that similar odd-even effect was also observed in the alkaneselenolate SAMs on Au and Ag,[24,25] with the same dependence on the alkyl chain parity; this underlines once more an important role of the substrate-dependent bending potential in the balance of the structure-building forces.

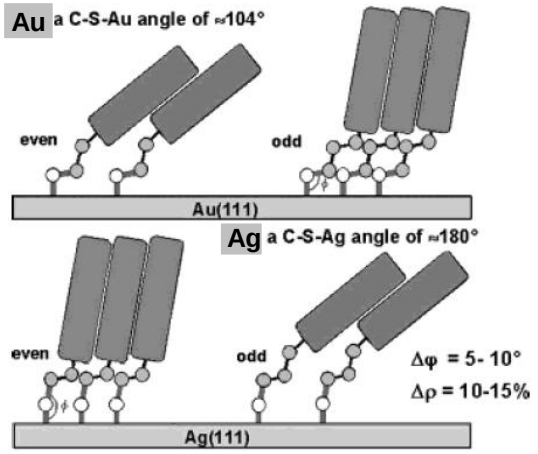

Figure 1.2: Schematic drawing of the orientation and packing of the terphenyl-substituted AT SAMs on Au and Ag. The Figure is taken from Shaporenko *et al*.[21]

As mentioned above, SAMs on coinage metal substrates have been studied extensively in the past years, in particular in terms of the structure-building interactions. However, the metal substrates are technologically limited for certain applications. In this context, surface self-assembly on semiconductor substrates has also attracted significant attention, particularly on the group IV and III-V semiconductors, taking into account their potential applications in the fields of electronic devices and sensors. In the case of the group IV semiconductors, assembly of monomolecular films on Si and Ge substrates through Si-O-Si,[2,26] Si-C,[27-29] Ge-C,[29,30] and Ge-S covalent bonds[31,32] has been reported. However, almost all these cases, except probably Ge-S, involve high energy bonds which hinder the most favorable self-organization of the grafted molecules. It can be understood that the molecules are strongly bonded to the silicon surface in deep wells with energies >> k_BT, thus suppressing adsorbate translational mobility.[33] In contrast, in the case of the III-V semiconductors, organothiol molecules were

found to be able to form densely packed SAMs on the oxide free surface through thiolate bond, which is the same type of bond appearing in the most popular alkanethiolate SAMs on Au.[6] The most potentially useful III-IV substrates for the thiolate based SAMs include GaAs,[34] InP,[35,36] and InAs[37,38].

Among the above III-IV semiconductors, GaAs is especially promising for the fabrication of nanostructure devices and sensors, because it permits a flexible band-gap engineering and is well suitable for heteroepitaxy.[39-43] Nevertheless, some of its applications are severely restricted because of the chemical instability of the GaAs surface both at ambient conditions and in physiological electrolytes. A proper way to address this problem is to functionalize the GaAs surface with suitable monomolecular films, namely functional SAMs which can passivate and protect the surface as well as simultaneously modify its properties in a desired way. In this context, a variety of different SAMs have been prepared and studied to some extent, including non-substituted ATs (NSATs) of different lengths ($C_nH_{2n+1}SH$),[33,34,44-49] substituted ATs,[50-53] as well as non-substituted and substituted aromatic thiols.[51,54-59]

Despite a large variety of the organothiol molecules used for the monolayer preparation on the GaAs substrate, high quality SAMs could only be reproducibly prepared under quite rigorous conditions, which is related to the strong proneness of the GaAs surface towards oxidation and to its complex surface chemistry.[34] In this context, SAM fabrication on GaAs substrate is a task in its own, and many factors should be taken into account during the preparation procedure, such as removal of the native oxide, control of humidity, and rigorous use of anaerobic conditions to prevent oxide regrowth during the preparation steps. Probably the most reliable preparation method has been brought out by D. L. Allara et al.;[34] using this method, NSAT SAMs of high quality could be formed on GaAs surface in a reproducible fashion.[33,34] In addition, this method is also suitable for the monolayer preparation from some substituted ATs.[52,60]

Despite the above achievements, most of the previous studies have not dealt with the mechanism behind the self-assembly process, in particular, in terms of the structure-building factors. Notable exceptions are recent publications by D. L. Allara et al., in which this issue was considered in very detail by the example of NSAT SAMs, in particular octadecanethiol (ODT) monolayer on GaAs (001).[33,45] The respective film represents pseudohexagonal overlayer with nearly vertically oriented alkyl chains (14°),[34] and the packing density is given by ~21.2 $Å^2$ per molecule.[45] However, the above ordered structure could only be formed in much smaller domain size of ~74 Å[45] as compared to ~250 Å[45] and ~120 Å[9] for AT SAMs on

Au(111) and Ag(111), respectively. Based on the analysis of the experimental data, the smaller domain size was attributed to the inherent mismatch between the substrate spacing (3.995 and 5.65 Å for NN and NNN spacing of As (or Ga) atoms) and symmetry of the square lattice pinning sites and the ideal molecular lattice spacing (4.70 and 5.02 Å) and hexagonal symmetry for crystalline packing of vertically oriented chains.[45] The incommensurate structure of ODT SAM on GaAs (001) is shown in Figure 1.3. To obtain the preferred hexagonal molecular packing, the above mismatch is overcome by distortion of the GaAs (001) surface lattice, which is driven primarily by the kinetic factor of the intermolecular interaction.

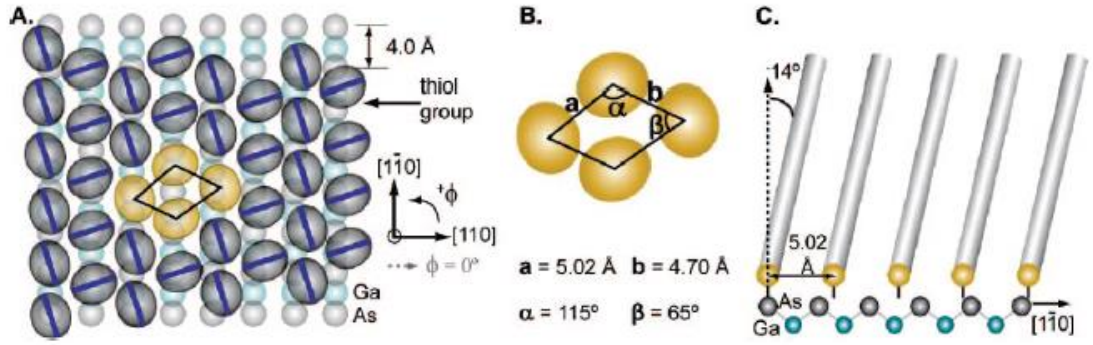

Figure 1.3: (A) The molecular unit cell embedded in a larger, ideal monolayer overlayer structure. The monolayer structure is shown in real space with respect to an ideal intrinsic As-terminated (001) GaAs surface. The gray ellipses represent top down vertical projections of untilted thiolate chains onto the substrate plane with the C–C–C planes indicated as blue bars. The relative twists of the chains show the herringbone pattern deduced from the IRS data. (B) Representation of a unit subcell and the associated lattice parameters. (C) Schematic side view representation of the monolayer structure along the [110] substrate direction. Note that the 5.02 Å adsorbate spacings determined from GIXRD do not match the ideal As atom spacings along the [110] direction in the intrinsic (001) substrate plane. Given the presence of S–As chemical bonds, this mismatch implies the As atoms must shift and reorganize during chemisorption of the alkanethiols to accommodate the molecular spacing. The Figure is taken from McGuiness *et al.*[45]

Comparing the results for GaAs and coinage metal substrates, one finds a structure discrepancy between the molecular orientation and packing density in the case of GaAs. The alkyl chains of the ODT molecules tilt (~14°)[34] similarly like those in AT SAMs on Ag (111) (~10 – 12°),[2,3,7-9] but have the lateral spacing (~5 Å) and reciprocal packing density (~21.2 Å^2 per molecule)[45] which are comparable to those for AT SAMs on Au (111). (~5 Å and ~21.62 Å^2 per molecule, respectively)[2,3,7,8,61] Neither the "free joint" nor "bending potential" models can explain the observed molecular organization unless GaAs has a strong bending potential which is similar to that on Ag (111).

This suggests that the molecular organization on GaAs (001) should be studied in more detail, if possible, in terms of the structure-building factors behind it. For this purpose, SAMs of NSATs with different chain lengths and some specially designed molecules, including terphenyl- and methyl-terminated biphenyl-substituted ATs (scheme 1.1), partially fluorinated

alkanethiols (PFAT) (scheme 1.2), and dihexadecyl diselenide (scheme 1.3) were prepared on GaAs (001) with high quality under rigorous experimental conditions. A variety of advanced surface characterization techniques, such as synchrotron-based High Resolution X-ray Photoelectron Spectroscopy, Near Edge X-ray Absorption Fine Structure spectroscopy, and Infrared Reflection Absorption Spectroscopy were applied to investigate these SAMs, providing a deep insight into their molecular organization. After unraveling the structure of these films, some basic structure-building factors of molecular assembly on GaAs were clarified; understanding of these factors can help one to design functional SAMs on this technological important semiconductor substrate, and, thus to realize its promising applications in the future.

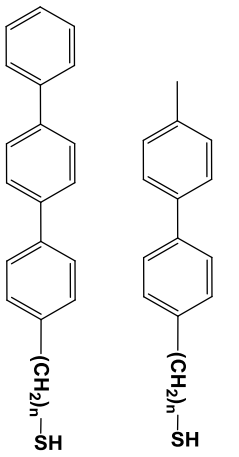

Scheme 1.1: The structures of the TPn (n=0-6), and BPn (n=1-6) precursors studied.

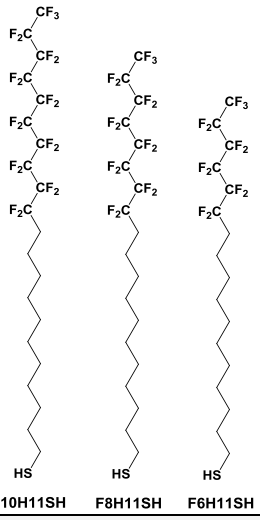

Scheme 1.2: The structures of the FnH11SH SAM precursors studied, along with their abbreviations.

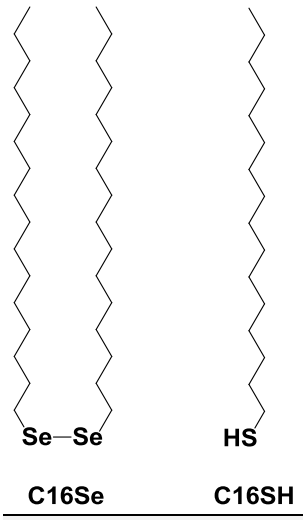

Scheme 1.3: molecular structure of C16Se and C16SH.

Based on the literature results,[33,34,45] ODT SAM was selected to serve as a starting reference model for the more complex systems. Thus, firstly, a full set of surface characterization techniques were applied to check this monolayer, which was prepared using the method reported by D. L. Allara et al..[34] The results were described in chapter 4, it was found the quality of the prepared ODT SAM was comparable to the best reported one,[34] which was essential to perform further work of molecular assembly on this complex semiconductor surface. Afterwards, pronounced chain length effect existing also for all other studied SAM systems on GaAs was elucidated through comparing the structure of the NSAT SAMs with different chain lengths.

In addition to the chain length effect, another important structure-building factor, viz. the existence of the bending potential, which, as mentioned above, is essential for thiolate and

selenolate SAMs on metal substrates, was demonstrated by studying the odd-even effects in the specially designed terphenyl- and methyl-terminated biphenyl-substituted AT (scheme 1.1) SAMs in chapter 5. These selected TPn (n = 0 – 6) and BPn (n = 1 – 6) monolayer systems are well suitable for the given purposes as discussed above and shown by the analogous studies for coinage metal substrates.[16-23]

To extend the family of functional SAMs on GaAs and to have a better understanding of the interplay of the two structure-building factors discussed above, viz. chain length effect and bending potential, novel PFAT SAMs with variable length of the fluorocarbon segment, viz. $CF_3(CF_2)_{n-1}(CH_2)_{11}SH$ (FnH11SH, n = 6, 8, and 10) (scheme 1.2) were prepared on Au (reference) and GaAs (001) substrates, and characterized in detail. In these films, the attachment of the bulky fluorocarbon part with a van der Walls (vdW) diameter of 5.67 Å[62,63] as compared to 4.4 Å[14] for the hydrocarbon part leads to an increase in the chain-chain spacing for the hydrocarbon moieties, which consequently results in a significant (by a factor of 2–3 as compared to AT SAMs) reduction of the intermolecular vdW interaction between the hydrocarbon segments. Thus, it is interesting to study the bending potential effect for the structure of these segments under this situation. By contrast, the interaction between the fluorocarbon segments also occurs separately from the hydrocarbon parts due to their inherent helical conformation,[64-66] correlated with the larger vdW diameter of these segments. In the given FnH11SH series, the length of the fluorocarbon segment was varied, thus, the chain length effect was examined in the case of fluorocarbon chain instead of the hydrocarbon chain. As a reference system, the FnH11SH SAMs on Au were first addressed in chapter 6, providing a variety of valuable general finding regarding the balance of the structure-building forces in these systems. Afterwards, the characterizations of the analogous (FnH11SH) films on GaAs (001) were presented in chapter 7, the two structure building factors were highlighted after clarifying the structure of these FnH11SH films.

In chapter 8, the characterization of one non-substituted alkaneselenolate SAM was presented, the results indicated the suitability of selenol anchor for the molecular assembly on GaAs. In addition, the structure of the formed selenolate SAM was compared with the analogous thioalte one.

Finally, the results of this thesis are summarized in chapter 9.

Chapter 2: Basic Theory

2.1 X-ray Photoelectron Spectroscopy (XPS)

XPS is one of the most widely used surface analyzing techniques.[67] Using XPS, the elemental composition of a sample up to a depth of 10-20 nm can be quickly obtained. During an XPS measurement, the atoms in the sample of interest, which can be solid, liquid or gas, are excited with X-rays of a given energy $h\nu$, thus leading to ionization of the atoms and emission of photoelectrons with defined kinetic energies. The kinetic energy of the ejected photoelectron is characteristic of the element under study and is given by equation 2−1.

$$KE = h\nu - BE - \phi_{spec} \qquad (2-1)$$

Where KE is the kinetic energy of the photoelectrons, $h\nu$ is the excitation energy, ϕ_{spec} is the work function of the spectrometer and BE is the binding energy of the corresponding core level. The energy scale of an XPS spectrum is typically in binding energy units (Figure 2.1 as an example). The intensity of the XPS signal for a given element is described by the following equation:

$$I = N \times \sigma \times \lambda \times cos(\theta) \times K \qquad (2-2)$$

where N is the average atomic concentration of the atom under consideration, σ is the ionization cross-section as defined by Scofield,[68] λ is the inelastic mean free path length, θ is the take-off angle and K an instrument constant that depends on several experimental factors such as the transmission function of the analyzer, the yield of the detector and the photon flux.

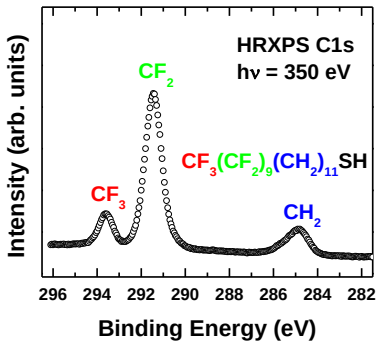

Figure 2.1: C 1s HRXPS of F10H11SH SAM on GaAs (001) acquired at a photo energy of 350 eV.

2.1.1 Elemental specificity

As explained above, XPS is element specific. More importantly, it is also sensitive to the environment of the atom under study (Figure 2.1); this can be understood that one can not only distinguish between the different elements in a sample but also between the different species of the studied element. For example, as shown in Figure 2.1, it is easy to distinguish between the different carbon atoms, which are bound to hydrogen or fluorine atoms. Moreover, it is possible to distinguish the different CF_n species, like the $-CF_2-$ and $-CF_3$ terminal moiety. The same is true for all the elements.

2.1.2 Surface sensitivity of XPS

As illustrated in Figure 2.2, while X-rays can readily travel through solids, electrons exhibit significantly less ability to do so. In fact, for X-rays of 1 KeV (1254 eV and 1487 eV for Mg and Al excitation sources, respectively), the X-rays will penetrate 1000 nm or more into matter while electrons of this energy will only penetrate approximately 10 nm. Because of this difference, XPS, in which only emitted electrons are measured, is surface sensitive. Photoelectrons emitted from X-ray citation below the uppermost surface zone can not penetrate far enough to escape from the sample and reach the detector.

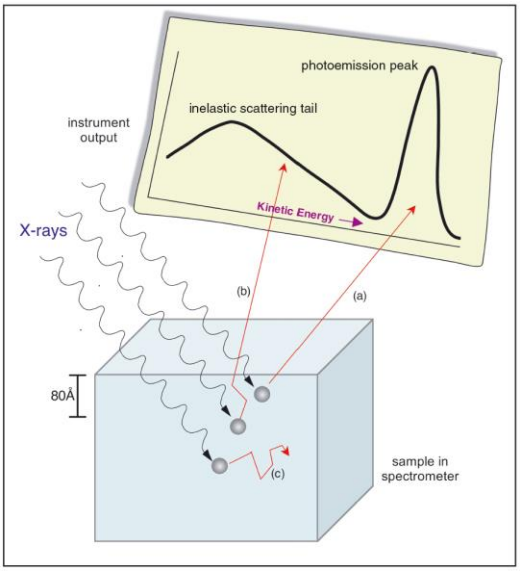

Figure 2.2: X-rays will penetrate deeply into a sample, and stimulate electron emission throughout the specimen. Only those electrons emitted from the surface zone that have suffered no energy loss will contribute to the photoemission peak (a). Electrons emitted from the surface zone that have lost some energy due to inelastic interactions will contribute to the scattering background (b). Electrons emitted deep within a sample will lose all their kinetic energy to inelastic collisions and will not be emitted (c). The Figure is taken from Ratner *et al.*[67]

In XPS, only the electrons that have not lost energy contribute to the peak signal; while the electrons, which suffer from energy loss, but still have sufficient energy to escape from the surface, will contribute to the background.[67] The sample depth ($d \approx 3\lambda$) is referred to the characteristic, average length over which the electron can travel with no loss of energy. The quantitative evaluation of the surface sensitivity, correlated with the sample depth, is described by the attenuation length, as talked below.

2.1.3 Attenuation length

The attenuation length "λ" is defined as the average distance travelled by an electron between two inelastic collisions.[67] It is derived using a model in which elastic collisions are neglected and thus differs from the inelastic mean free path (IMFP).[69] λ varies with the kinetic energy of the photoelectrons for one given material. In this thesis, the material focuses on organic molecular films, so the attenuation length λ is given by equation 2−3, which applies for a wide variety of carbon-containing organic layers on kinds of substrates.[70,71]

$$\lambda = 0.3 \times KE^{0.64} \qquad (2-3)$$

2.1.4 Intensity of the XPS signal and thickness calculation

The photoemission signal can be attenuated with the upper overlayer, and its intensity is directly related to the attenuation length of the photoelectrons; this situation is quantitatively described in Figure 2.3.

Thus, according to Figure 2.3, the thickness of overlayers can also be calculated. In this thesis, the thickness of organic monolayers on Au and GaAs substrates is calculated using the intensity ratio between the C1s emission and the emission from the core level atom of the substrate, i.e. Au 4f and As 3d for Au and GaAs substrate, respectively, and the equation is described as below:

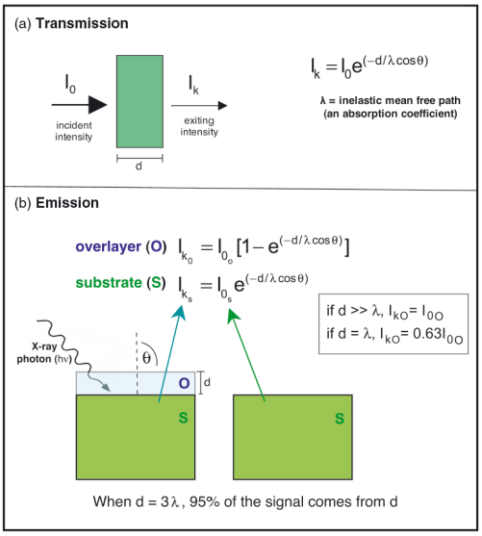

Figure 2.3: (a) For electrons transmitted through a sample, Beer's law of molecular absorption explains the total intensity loss for electrons that lose no energy in traversing the sample. (b) For electron emission from a thick sample, modifications of Beer's law can explain the photoemission intensity from an overlayer or from the substrate covered by an overlayer. The Figure is taken from Ratner *et al.*[67]

$$\frac{\frac{I_c}{I_{sub}}(sample)}{\frac{I_c}{I_{sub}}(refer)} = \frac{1-exp\frac{-d_{sample}}{\lambda_{C1s}(E_C)}}{exp\frac{-d_{sample}}{\lambda_{sub}(E_{sub})}} \times \frac{exp\frac{-d_{refer}}{\lambda_{sub}(E_{sub})}}{1-exp\frac{-d_{refer}}{\lambda_{C1s}(E_C)}} \qquad (2-4)$$

In equation 2−4, I_c and I_{sub} are the intensities of the C1s emission and the emission from the core level atom of the substrate, the attenuation length "λ" of different photoelectrons (C1s, As3d, Au4f) depends on the kinetic energy. In addition, one proper reference film with a well known thickness value is required for the thickness evaluation.

2.1.5 Enhancing the surface sensitivity

In some cases, the sample depth (~3λ) of XPS might still be too large, and one typical case is just in the present thesis, viz. SAMs on GaAs (001) substrate. Some problems happen in the routine XPS measurement, such as: (1) the detailed component information of the target element (like the different As or Ga components) in the near surface (e.g. SAM-GaAs interface) can not be fully obtained; (2) the interested emission peak is interfered (like C1s) or even totally covered (like S2p) by other emissions from the GaAs substrate. These issues would also be described more in later chapters. However, the above limitations can be overcome through enhancing the surface sensitivity of XPS measurement, which can be realized mainly by two ways, as introduced below:

2.1.5.1 Variation of the take-off angle

As clearly seen in Figure 2.4, by tilting the sample, the effective sample depth decreases by a factor of cosθ ; in the lab-XPS (Max-200) measurement, normally a take-off angle (θ) of 60° is applied to achieve a better surface sensitivity for samples on GaAs (001) substrate.

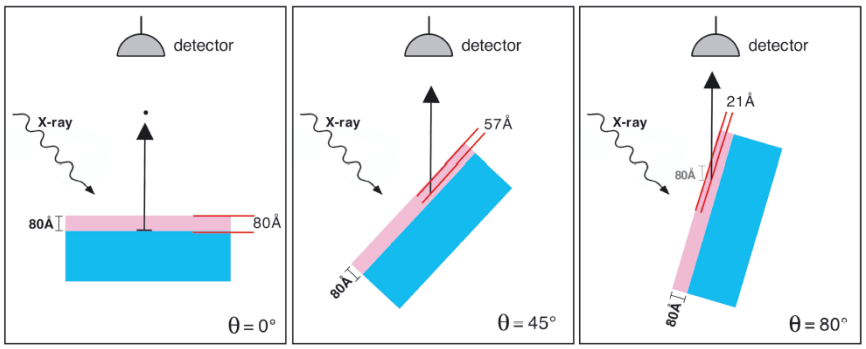

Figure 2.4: As the sample is rotated, maintaining the X-ray source and detector in fixed positions, the effective sampling depth decreases by a factor of cosθ. Note that the emitted photoelectron travels 80 Å through matter at all take-off angles. The take-off angle, θ, is defined relative to the normal to the surface. The Figure is taken from Ratner *et al.*[67]

2.1.5.2 Variation of the excitation energy

According to equation 2−3, by reducing the excitation energy ($h\nu$), the *KE* of the photoelectrons would decrease simultaneously, thus resulting smaller λ. This allows us to probe the sample composition up to a smaller sample depth ($d \approx 3\lambda$). The variation of the excitation energy can be realized in the synchrotron-based High Resolution XPS measurement.

2.2 Near Edge X-ray Absorption Fine Structure (NEXAFS) spectroscopy

In a NEXAFS experiment, core level electrons are excited into non-occupied molecular orbitals, which are characteristic of specific bonds, functional groups, or the entire molecule. The respective absorption resonances provide then a clear signature of these entities. Moreover, the orientation of the molecular constituents, averaged over the probed ensemble, can be derived from the NEXAFS data since the cross-section of the resonant photoexcitation process depends on the orientation of the electric field vector of the linearly polarized synchrotron light with respect to the molecular orbital of interest, so called linear dichroism in X-ray absorption.[72] This section only presents a brief overview of the basic principles of NEXAFS spectroscopy; for a complete review of the NEXAFS technique, including the mathematics behind it, please refer to the book by Joachim Stöhr.[72]

2.2.1 Basic principles

The sample is irradiated with monochromatic X-rays (synchrotron light) of varying energies below and up to 50 eV above the ionization potential (IP e.g. ~291 eV for the carbon K-edge).[74] Figure 2.5a illustrates several distinct processes that can occur during the generation of the NEXAFS spectrum. The incident photon beam excites an electron from a core state into an unoccupied electronic state and the subsequent relaxation of the excited molecule results in the ejection of either an Auger electron or an energetic photon with the cross-section of each process being atomic number dependent.[73] Indeed, it is generally possible to monitor each of these processes, as shown in Figure 2.5b, and thus there are several ways of obtaining a NEXAFS spectrum. Among them, partial electron yield (PEY) and Auger electron yield (AEY) are the most surface sensitive detection methods. In a NEXAFS experiment, unlike XPS, both elastically and inelastically scattered electrons are collected. In the PEY method, which is also used throughout this thesis work, heavily scattered and low kinetic energy electrons are excluded by applying a threshold voltage thus making this technique more surface sensitive.

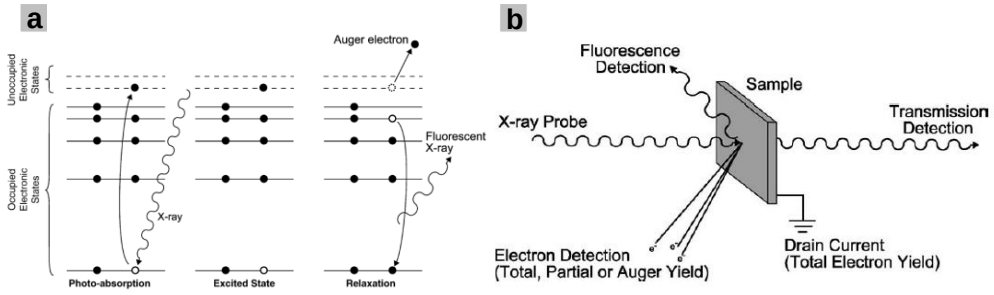

Figure 2.5 a: Schematic representation of the processes occurring during a NEXAFS experiment; **b:** Schematic representation of the different NEXAFS measurement methods. Figure 2.5 was taken from Watts *et al.*[73]

2.2.2 Angular dependence of the NEXAFS signal

The absorption resonance intensity, i.e. of a C1s → π_1^* transition, depends on the orientation of the electric field vector of the synchrotron light with respect to the molecular orbital of interest (Figure 2.6). The absorption resonance intensity is proportional to the square of the dot product of the electric field vector of the X-rays ($\vec{E}$) and the orbital vector ($\vec{O}$).

$$I \propto \left|\vec{E} \cdot \vec{O}\right|^2 \tag{2-5}$$

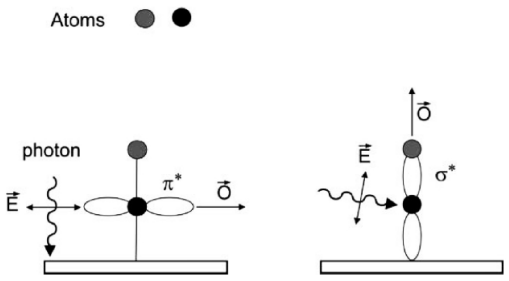

Figure 2.6: Schematic representation of the interaction of X-rays with π^* (left) and σ^* (right) orbitals of a diatomic molecule standing perpendicular to a surface. The intensity of the resonance associated with the π^* resonance is maximum if the X-ray is perpendicular to the surface (θ = 90°). By contrast, the intensity of the resonance associated with the σ* resonance is maximum if the X-ray is in the grazing incidence geometry (θ < 30°). The Figure was taken from Hähner.[74]

A fingerprint of the orientation of the molecular orbitals is the linear dichroism, which is conveniently monitored by plotting the difference of the NEXAFS spectra acquired at normal (90°) and grazing (20°) angles of X-ray incidence. In contrast, a spectrum acquired at the so-called magic angle of X-ray incidence (55°) is not affected by any effects related to the molecular orientation and only gives information about the chemical identity of the investigated samples.[72]

In addition, the average tilt angle of the respective molecular orbital can be quantitatively calculated based on the linear dichroism of the NEXAFS spectra.[72] The detailed evaluation process for different types of orbitals, like vector type of π_1^* orbital or plane type of R^* orbital, would be introduced in later chapters.

2.3 InfraRed Reflection Absorption Spectroscopy (IRRAS)

IRRAS is a kind of infrared spectroscopy performed on the surface. As in a typical infrared (IR) experiment, the IR signal results from the interaction of the electromagnetic field of an infrared radiation with the oscillation dipole associated with a particular normal vibration mode. If the transition dipole moment (TDM) associated with the vibration of interest lies perpendicular to the surface or has a major component perpendicular to the surface, it will give rise to an absorption band in the IR spectrum. By contrast, if the TDM lies parallel to the surface, then no absorption band will be visible for the associated vibration. Thus, following this, high incidence angle (> 80°) of the IR light is required to achieve high signal to noise ratio.

2.4 Ellipsometry

Ellipsometry measures the change of polarization upon reflection. The exact nature of the polarization change is determined by the sample's properties, such as thickness, complex refractive index or dielectric function tensor. Although optical techniques are inherently diffraction limited, ellipsometry exploits phase information and the polarization state of light, and can achieve Angstrom (Å) resolution. In its simplest form, the technique is applicable to thin films with thickness less than a nanometer to several micrometers. The sample must be composed of a small number of discrete, well-defined layers that are optically homogeneous and isotropic. The schematic setup of the typical ellipsometry measurement is shown in Figure 2.7.

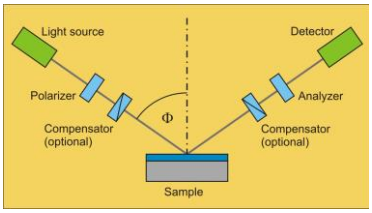

Figure 2.7: Schematic setup of an ellipsometry experiment.

2.5 Contact angle goniometry

2.5.1 Basic Principle

In contact angle goniometry, one measures the angle (θ in Figure 2.8a) between a drop of liquid and a surface at equilibrium. The shape of the drop is defined by the properties of the liquid (L), the surface (S) and the vapor (V) as described in Figure 2.8a. This is described by the Young equation:

$$\gamma_{SV} = \gamma_{SL} + \gamma \cdot \cos\theta \qquad (2-6)$$

where γ_{SV} is the interfacial energy between the solid and the vapor, γ_{SL} is the interfacial energy between the solid and the liquid, γ is the interfacial energy between the liquid and the vapor, and θ is the equilibrium contact angle.[75]

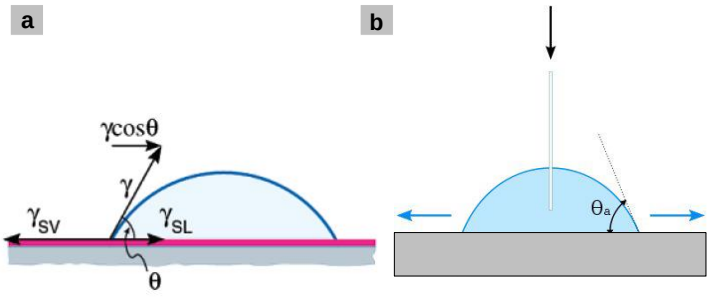

Figure 2.8a: Schematic representation of a drop on a surface; **b:** Schematic representation of the advancing contact angle. Figure 2.8a was taken from Tadmor.[75]

2.5.2 Advancing and static contact angle

As shown in Figure 2.8b, small enough amount of liquid (Milli Q water in this thesis) is added to a drop until the contact line can not be pinned, the maximum contact angle is defined as advancing contact angle.

Chapter 3: Experimental Parts

3.1 Substrates

GaAs (001): Single side polished n^+-type doped GaAs (001) wafers (Si dopant density (Ne) = 1.5~1.6 × 10^{18} cm^{-3}) were purchased from American Xtal Technologies, Guangzhou, China; and they were used for all studies throughout this thesis work.

Au (111): The standard gold substrates were prepared by thermal evaporation of 100 nm of gold (99.99% purity) onto polished single-crystal silicon (100) wafers (Silicon Sense) that had been precoated with a 5 nm titanium adhesion layer. Such evaporated films are polycrystalline in nature with a grain size of 20-50 nm as observed by atomic force microscopy. The grains predominantly exhibit a {111} orientation.[76]

3.2 Chemicals

Octadecanethiol (ODT, $CH_3(CH_2)_{17}SH$) and Hexadecanethiol (HDT, C16SH, $CH_3(CH_2)_{15}SH$) were purchased from Fluka Chemika, Dodecanethiol (DDT, $CH_3(CH_2)_{11}SH$) was purchased from Sigmal-Aldrich. These NSAT molecules were used without further purification.

4,4´-terphenyl-substituted alkanethiols, $C_6H_5(C_6H_4)_2(CH_2)_nSH$ (TPn, n = 0 − 6), molecules were custom synthesized;[21] 4´´-(mercaptomethyl)terphenyl-4-yl-carbonitrile $CN–C_6H_5(C_6H_4)_2(CH_2)SH$ (TP1CN) was synthesized according to Ref [79]; ω-(4´-methyl-biphenyl-4-yl)-alkanethiols, $CH_3(C_6H_4)_2(CH_2)_nSH$ (BPn, n = 1 − 6), were custom synthesized,[17] the structure of the TPn and BPn molecules can be be found in Scheme 1.1.

PFAT precursors, $CF_3(CF_2)_{n-1}(CH_2)_{11}SH$ abbreviated as FnH11SH (n = 6, 8, and 10), (molecular structure shown in Scheme 1.2) were prepared following literature procedures[77,78] with slight modifications. See more in the Appendix (A1).

Hexadecyl diselenide, $C_{16}H_{33}SeSeH_{33}C_{16}$ abbreviated as C16Se, (molecular structure shown in Scheme 1.3) was custom synthesized according to Ref [81].

3.3 SAM preparation on GaAs (001)

3.3.1 NSAT SAMs: The optimum procedure for preparing high quality NSAT SAMs on GaAs substrates has already been reported[33,34] and was also used in the experiment of this thesis. The procedure briefly follows as: the native oxide of GaAs was removed by immersing the substrates in concentrated NH_4OH (PROLABO, 30% NH_4OH in water) from 1 to 5 min. Immediately after immersion, the sample was rinsed with degassed absolute ethanol (Sigma Aldrich) and dried with a Ar stream. The substrates were then immersed in degassed ethanolic solutions (degassed through multiple freeze-pump-thaw cycles) containing 3 mM NSAT precursors (ODT, HDT, or DDT) and 10 mM NH_4OH, and transferred into a nitrogen-purged glovebox for incubation of 24 hours at room temperature. After incubation, the samples were taken out of the solutions, rinsed carefully with Abs ethanol, and blow dry with Ar.
In this thesis, ODT SAM is used as a reference to calculate the film thickness and packing densities for other SAMs.

3.3.2 TPn and BPn SAMs: The preparation for TPn (n=0 – 6, also TP1–CN) and BPn (n=1 – 6) SAMs were carried out under inert (Ar) atmosphere to reduce surface oxidation. The optimum procedure follows briefly as: After the pretreatment, the GaAs substrates were etched in concentrated HCl (37%) for 1 min to remove the native oxide layer. This resulted in a As:Ga surface ratio of ~86%, as measured by XPS and in agreement with other studies,[50] and a root mean square (rms) value of 0.35 nm (scan area 1 × 1 μm2), as compared to 0.21 nm for the pristine GaAs. Thus, the etching step only roughens the initial substrate topography to a rather small extent, which is supported by the AFM results in Figure 3.1. The freshly etched substrates were immediately immersed into 0.1mM target solutions (TPn or BPn) in anhydrous ethanol, and incubated there for 24h at room temperature. Note that both the etching and immersion steps were carried out under Ar atmosphere using the schlenk-line setup. After the SAM formation, the samples were taken out of the reactor, rinsed softly with different organic solvents (in a sequence of abs ethanol, acetone, chloroform, and abs ethanol) to remove physisorbed molecules, dried by Argon flow and then preserved in Ar filled glass container.

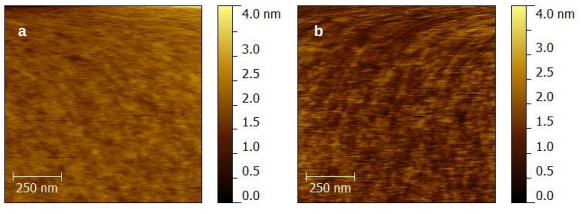

Figure 3.1: AFM contacting mode topography of the GaAs(001) surface: (a) starting native oxide covered substrate, (b) after HCl etching.

3.3.3 PFAT (FnH11SH) SAMs: The optimum procedure for preparing PFAT SAMs was based on the developed one for TPn and BPn precursors above, with only slight modification in the rinsing step: After the SAM formation, the samples were taken out of the reactor, rinsed extensively with absolute ethanol to remove physisorbed molecules, dried by Argon flow and preserved in Ar filled glass containers.

3.3.4 C16Se SAM: The optimum procedure for preparing C16Se SAM was also based on the developed one for TPn and BPn precursors, two modifications were made here: (1) The concentration of the incubation solution (C16Se) is 5 μM since a μM concentration is crucial for growing high quality selenolate SAMs.[81-83] (2) After the SAM formation, the samples were taken out of the reactor, rinsed extensively with absolute ethanol to remove physisorbed molecules, dried by Argon flow and preserved in Ar filled glass containers.

3.4 SAM preparation on Au (111)

3.4.1 NSAT SAMs: HDT and DDT SAMs were prepared using the standard protocol:[61] Freshly prepared gold substrate was immersed into 1 mM solution of HDT (or DDT) in Abs ethanol for 24 h at room temperature. After immersion, the sample was thoroughly rinsed with pure Abs ethanol, and blown dry with Ar. DDT and HDT SAMs were used as reference to calculate the film thickness and packing densities for other SAMs on Au, respectively.

3.4.2 TPn SAMs: The TPn (n=0 – 6) SAMs were prepared according to Ref [21], which follows as: the freshly prepared substrates were immersed into 1 mM TPn solution in THF at room temperature for 24 h. After immersion, the samples were carefully rinsed with pure solvent and blown dry with argon. No evidence for impurities or oxidative degradation products was found in the XPS spectra.

3.4.3 PFAT (FnH11SH) SAMs: The PFAT SAMs were prepared by immersion of the fresh substrates in 1 mM PFAT solutions in analytical grade dichloromethane for 24 h at room temperature. After immersion, the films were rinsed with the solvent and blown dry with argon. Extensive characterization showed no evidence of impurities or oxidative degradation products.

3.5 SAM characterization

The fabricated SAMs on Au and GaAs (001) were characterized by a variety of surface analyzing techniques, including XPS, synchrotron-based HRXPS and NEXAFS spectroscopy, IRRAS, ellipsometry, and contact angle goniometry. All these measurements were performed at room temperature. Ellipsometry and contact angle measurements were taken within 3 minutes after the SAM formation; for other measurements, in particular the synchrotron-based measurements, the samples were preserved in Ar filled container until the measurements were carried out.

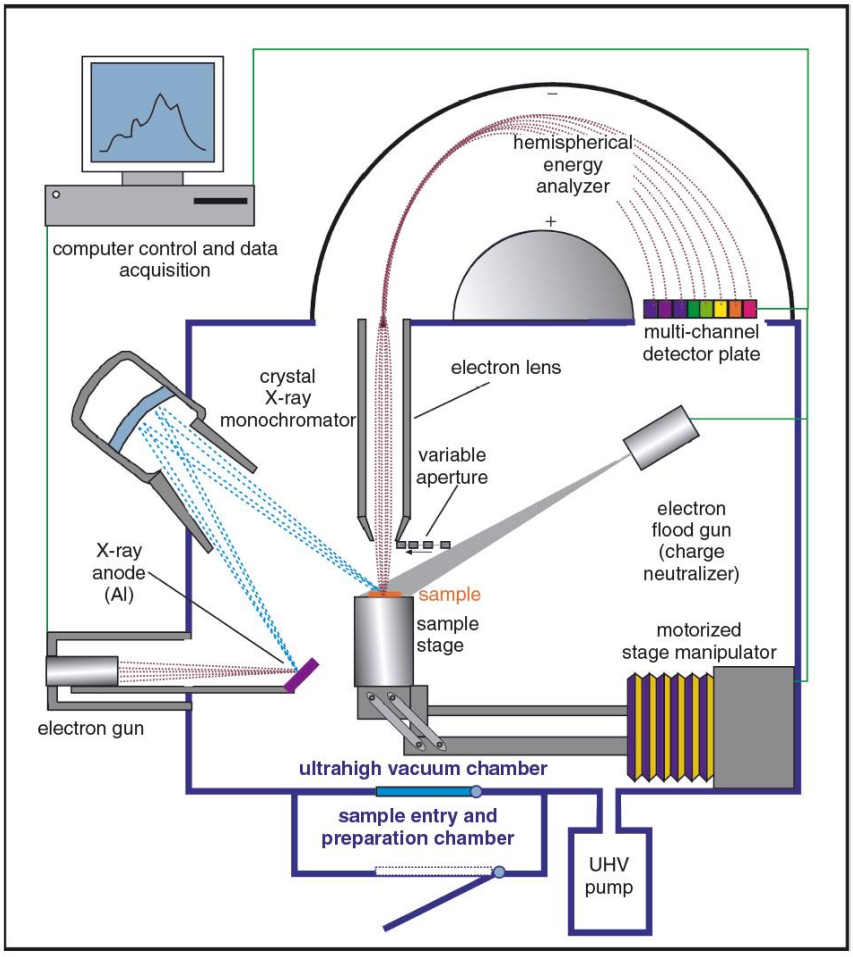

Figure 3.2: A schematic diagram of an XPS spectrometer using a monochromatized X-ray source. The key components of a modern spectrometer are identified. The Figure was taken from Ratner *et al.*[67]

3.5.1 XPS (Max-200)

The schematic diagram of one XPS spectrometer with the key components is illustrated in Figure 3.2. The XPS measurements in our lab were carried out under UHV conditions (less than 2×10^{-8} mbar) with a MAX200 (Leybold-Heraeus) spectrometer equipped with an Mg Kα

X-ray source (200 W) and a hemispherical analyzer. The recorded spectra were corrected for the spectrometer transmission.

Despite the GaAs wafers used throughout this thesis are conductive, the surface charging may still take place on this semiconductor surface during the X-ray irradiation (assuming to occur in a small extent). To avoid this, the binding energy (BE) scale was referenced to $As3d_{5/2}$ assigned for bulk GaAs component at 41.1 eV when evaluating the XPS spectra of SAMs on GaAs (001).[44,55,58] By contrast, the surface charging can be avoided in the case of Au substrate because of the associated conductivity of metal. The BE scale was referenced to $Au4f_{7/2}$ at 84 eV.[84]

3.5.2 High Resolution X-ray Photoelectron Spectroscopy (HRXPS)

In this thesis, the HRXPS measurements were carried out in two synchrotron radiation centers: 1. Max-Lab in Lund, Sweden; 2. Bessy II in Berlin. The synchrotron-based HRXPS measurements at these two places would be introduced below:

1. Max-Lab: The HRXPS measurements were carried out at the D1011 beamline of the synchrotron storage ring MAX II at MAX-Lab in Lund, Sweden, at room temperature and a base pressure lower than 1.5×10^{-9} Torr. The spectra were collected by a SCIENTA analyzer in normal emission geometry. The energy resolution was ~0.1 eV.

2. Bessy II: The HRXPS measurements were carried out at the HE-SGM beamline (bending magnet) of the synchrotron storage ring BESSY II in Berlin, Germany, using a Scienta R3000 spectrometer. The energy resolution was ~0.3 eV.

During the HRXPS measurements in the beamtime at Max-lab (1) and Bessy II (2), the choice of photon energy (PE) for a particular spectrum was based on the optimization of the photoionization cross section for the corresponding core level and on adjustment of either surface or bulk sensitivity.[85-87] The spectra acquisition time was selected in such a way that no noticeable damage by the primary X-rays occurred during the measurements.[88-91]

The HRXPS spectra calibration was performed in the same way as routine XPS: The BE scale was referenced to $As3d_{5/2}$ for the bulk GaAs component at 41.1 eV[44,55,58] and to $Au4f_{7/2}$ at 84 eV[84] for samples on GaAs and Au substrates, respectively.

The decomposition of the HRXPS spectra was performed self-consistently over the entire data set. The spectra were fitted using Voigt peak profiles and a Shirley background. In the thesis work, to fit the doublets for Ga 3d, As 3d, S 2p and Se 3d emissions, we used two peaks with the same full width at half-maximum (fwhm), a reasonable spin-orbit splitting, and branching ratios of 2:1 ($2p_{3/2}/2p_{1/2}$) and 3:2 ($3d_{5/2}/3d_{3/2}$). The S.O.S. (Spin Orbital Splitting)

values for As 3d, Ga 3d, S 2p, Se 3d orbitals are 0.69, 0.43, 1.18, and 0.86 eV, respectively, these values were set according to literature data.[44,55,58,81] Due to the ultimate energy resolution and the presence of the spectra dominated by a single doublet, we were also able to derive the initial setting for the respective parameters directly from the spectra taken at lower PE (PE ≤ 350 eV). The resulting accuracy of the binding energies and fwhm reported here is 0.04-0.05 eV. These values are noticeably lower than the ultimate accuracy of the experimental setup (see, e.g., Ref [18]), but mostly reflect the distribution of the resulting fit parameters over the spectra of different samples.

3.5.3 NEXAFS spectroscopy

Like HRXPS, the NEXAFS measurements in this thesis were carried out at two synchrotron radiation centers: 1. Max-Lab in Lund, Sweden; 2. Bessy II in Berlin, which are individually introduced as below:

1. Max-Lab: The NEXAFS measurements were conducted at the synchrotron storage ring MAX II at MAX-Lab in Lund, Sweden, using the bending magnet beamline D1011 and an experimental station equipped with a SCIENTA SES200 electron energy analyzer and a partial electron yield (PEY) detector. The experiments were carried out under UHV conditions at a base pressure < 1.5×10^{-10} mbar. Spectra acquisition was carried out at the Carbon and Nitrogen *K*-edges in the PEY mode with retarding voltages of −150 V and −350 V, respectively. Linear polarized synchrotron light with a polarization factor of ~95% was used. The spectra acquisition time was selected in such a way that no noticeable damage by the primary X-rays occurred during the measurements.[88-91]

2. Bessy II: The NEXAFS spectroscopy measurements were performed at the HE-SGM beamline of the synchrotron storage ring BESSY II in Berlin, Germany, using a specially designed experimental station.[92] During analysis the samples remained at room temperature with a base pressure < 1.5×10^{-9} mbar. Spectra acquisition was carried out at the Carbon *K*-edge and Fluorine *K*-edge in the PEY mode with a retarding voltage of −150 V and −350 V, respectively. Linear polarized synchrotron light with a polarization factor of ~91% was used. The energy resolution was ~0.30 eV at the C *K*-edge and ~0.6–0.7eV at the F *K*-edge. The spectra acquisition time was selected in such a way that no noticeable damage by the primary X-rays occurred during the measurements.[88-91]

For the NEXAFS measurements at both Max-lab and Bessy II, the incidence angle of the light was varied from 90° (normal incidence geometry; ***E***-vector in surface plane) to 20° (grazing incidence geometry, ***E***-vector near surface normal) in steps of 10-20° to monitor the

orientational order within the molecular films, the approach is based on the linear dichroism in X-ray absorption.[72] The raw NEXAFS spectra were normalized to the incident photon flux by division through a spectrum of a clean, freshly sputtered GaAs sample. Before the normalization, a spectrum of freshly etched GaAs was subtracted from the raw spectrum of the varieties of SAMs on GaAs. The energy scale was referenced to the pronounced π_1^* resonance of highly oriented pyrolytic graphite at 285.38 eV.[93]

The decomposition of the NEXAFS spectra in the full dataset was performed with the WinXAS (version 3.2) software.

3.5.4 InfraRed (IR) spectroscopy

3.5.4.1 IR Measurement

IR measurements were performed with a dry-air-purged Thermo FTIR spectrometer model NICOLET 6700 equipped with a liquid-nitrogen-cooled mercury cadmium telluride semiconductor detector. The spectra of the neat substances were measured employing a diamond attenuated total reflection (ATR) unit. For each substance, 64 scans were averaged. The spectra of the SAMs were recorded using *p*-polarized light directed at an angle of 80° with respect to the sample surface normal and are reported in absorbance units, $A= -\log R/R_0$, where R is the reflectivity of the substrate with the monolayer and R_0 is the reflectivity of the reference. A gold substrate covered with a perdeuterated dodecanethiolate SAM was used as reference for SAMs on Au substrate, whereas the freshly etched GaAs substrate was used as reference for SAMs on GaAs (001) surface. For every SAM, at least 1000 scans were averaged. A smooth baseline correction was applied to the IRRAS spectra. All spectra were measured at a resolution of 4 cm^{-1}.

3.5.4.2 Density functional theory (DFT) calculation

In chapter 6, DFT calculation was used to better analyze the IR dataset for PFAT SAMs on Au, the assignment of the vibrational bands and the estimation of the orientation of their transition dipole moments (TDMs) were conducted with the help of DFT calculations of the isolated PFAT molecules at BP86/svp level employing Gaussian 09.[94] The combination of the BP86 density functional[95,96] and the svp[97] basis set usually yields suitable vibrational spectra, combined with a relatively low consumption of computing time.

Linear PFAT molecules with *all trans* (zig-zag) CH_2-chains and CF_2-helices with 168° dihedral angles between the C-atoms (equivalent to 15/7 conformation) were used as input structures, since the PFAT molecules in the SAM were expected to exhibit this or a similar

conformation. After geometry optimization, vibrational frequencies were calculated using the Hessian matrix (as implemented in the Gaussian program package). Upon geometry optimization, the dihedral angles in the CF_2 helices became slightly smaller (ca. 162°). This small difference is probably due to the fact that single molecules were calculated, whereas 168° is the dihedral angle of the stable helix in an assembly of many molecules in a solid polymer for a certain temperature range. A change in the dihedral angle can also be due to the overestimation of dispersion interactions, a well known problem of DFT. It should also be noted that because of their free electron pairs, F atoms turn out to be significantly more difficult to treat with quantum chemical methods than H atoms. Note that for all three PFAT molecules the calculated dihedral angles were almost identical.

3.5.5 Ellipsometry

The ellipsometry measurements were performed with an M-44 spectroscopic ellipsometer (J.A. Woollam Co. Inc., USA) at a fixed light incidence angle of ~75° under ambient conditions. Thickness calculations were performed using a single-layer Cauchy model with a refractive index of 1.5.

3.5.6 Contact angle measurement

The advancing and static contact angles of Millipore water were measured on freshly prepared samples with a Krüss goniometer Model G1. The measurements were performed under ambient conditions with the needle tip in contact with the drop. The drop volume was about 2 μL. At least three measurements at different locations on each sample were made. The averaged values are reported. Deviations from the average were less than 2°.

3.5.7 Atomic Force Microscope (AFM)

In the thesis, AFM results were only used to check the surface roughness of GaAs substrate before and after etching. Contacting mode AFM was performed with a SOLVER NEXT scanning probe microscope, using commercially available etched n-doped Si cantilevers with a force constant of 0.1~0.5 N/m. The roughness values (rms) were obtained from height images using the Gwyddion software (version 2.31).

Chapter 4: SAMs of Non-Substituted Alkanethiols on GaAs (001)

Based on the literature results,[33,34,45] ODT SAM on GaAs (001) can serve as a starting reference model for more complex systems. However, as introduced in chapter 1, highly oriented and closely packed ODT SAM can only be formed under rigorous experimental conditions. Therefore, the first aim in this thesis was to prove that the quality of the prepared ODT SAM was comparable to the best reported one.

Beyond ODT monolayer, two other NSAT monolayers with shorter chain length, namely HDT and DDT SAMs, were characterized. Through comparing the structure of these NSAT SAMs with different lengths, a pronounced "chain length effect" existing for all SAM systems on GaAs was elucidated.

4.1 ODT SAM

4.1.1 HRXPS

The As 3d and Ga 3d HRXPS spectra of ODT SAM and etched GaAs (freshly etched GaAs was preserved in Ar filled container until the beam measurement) acquired at a photon energy (PE) of 580 eV are shown in Figure 4.1. Here, the normalized spectra are compared without fitting process due to the resolution limit at this PE level. As clearly seen in Figure 4.1, the oxide-related features in the spectra of etched GaAs, viz. the spectra portion above 43 eV and the shoulder like feature at ~20.4 eV in As 3d (Fig 4.1a) and Ga 3d (Fig 4.1b) spectra, respectively, are not perceptible in those of ODT SAM. Note the Ga3d spectra of ODT SAM (Figure 4.1b) looks symmetric, without showing the shoulder typical for Ga_xO_y components. In reality, it is an easy, fast, and reasonable way to monitor the oxidation feature in the Ga 3d spectra by the spectral symmetry, in particular for the spectra taken at higher PE. This evaluation method is summarized after the analysis of

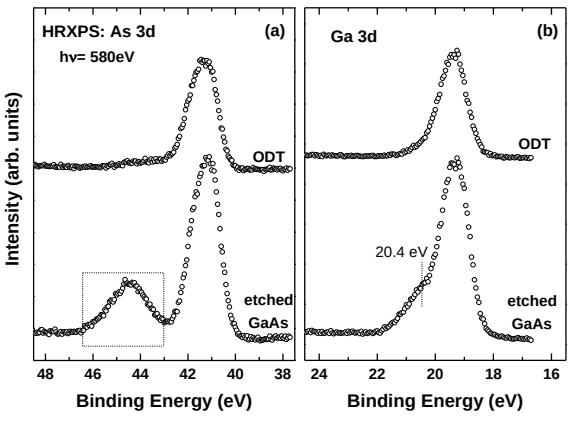

Figure 4.1: As 3d (a) and Ga 3d (b) HRXPS spectra of ODT SAM on GaAs (001) and the etched GaAs. The spectra were acquired at a photon energy of 580 eV. The oxide related features in the As 3d (>43 eV) and Ga 3d (shoulder like feature at ~20.4 eV) HRXPS spectra of the etched GaAs are marked (see text for detail).

the synchrotron-based HRXPS and lab XPS spectra for varieties of samples on GaAs, as well as after the evaluation of the analogous spectra data in previous literatures.[44,55,58]

To get the detailed component information at the ODT SAM-GaAs interface, the corresponding As 3d and Ga 3d HRXPS spectra taken at lower PEs are required. Figure 4.2 illustrates these spectra, which were acquired at PEs of 300 eV and 130 eV, while the latter PE is chosen to achieve the maximum surface sensitivity, corresponding to the smallest sample depth. (the electron mean free path reaches its minimum value at kinetic energies of 50-100 eV)[98,99] The derived parameters and the assignments of individual peaks are presented in Table 4.1. As seen in Figure 4.2, both the As 3d and Ga 3d spectra are dominated by the peaks related to the stoichiometric GaAs (light gray), accompanying some contributions from other components, like surface Ga 3d states (possibly also some Ga_2O_3 coexisting) and elemental As. The spectra weight for the peaks related to the elemental As or surface Ga 3d states increases with decreasing the PE from 300 eV to 130 eV, this suggests these components are located at the near surface region, i.e. at the SAM-GaAs interface. In addition, a black doublet assigned to As-S species is observed at 42.3 ± 0.05 eV. As expected, the intensity of this doublet increases with decreasing sampling depth, as follows from the comparison of the spectra taken at PEs of 300 and 130 eV. In contrast to the As3d spectra, the decomposition of the Ga 3d spectra does not require an introduction of an additional (with respect to the bare substrate) doublet related to the Ga-S species. Nevertheless, the existence of such doublet, even though very weak, cannot be completely excluded, due to an ambiguity of the spectra fitting in the relevant BE region.

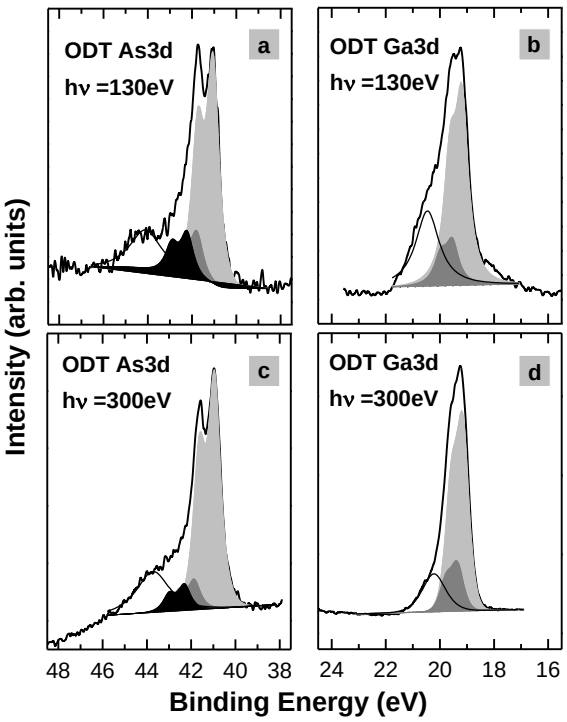

Figure 4.2: As 3d and Ga 3d HRXPS spectra of ODT SAM on GaAs (001). The spectra were acquired at photon energies of 130 eV (a and b) and 300 eV (c and d). The spectra are tentatively decomposed in several doublets related to individual chemical species. As 3d spectra: Light gray: stoichiometric GaAs; dark gray: elementary As; black: S-As. Ga 3d spectra: Light gray: stoichiometric GaAs; dark gray: Ga oxide or surface Ga 3d component. The shoulders at the higher binding energy side of the shadowed doublets correspond to As and Ga oxides. The assignments were performed in accordance with refs 44, 55, 58, 59.

Table 4.1: Parameters of Individual Emissions in the Ga 3d and As 3d Spectra in Figures 4.2[a]

core level	binding energy (eV)	assignment	spin-orbit splitting (eV)	branching ratio
Ga $3d_{5/2}$	19.2 ± 0.05	GaAs	0.43	3/2
	19.5 ± 0.1	Ga_2O_3 or surface Ga3d component		
	>19.8	Ga oxides		
As $3d_{5/2}$	41	GaAs	0.69	3/2
	41.85 ± 0.05	elementary As (As^0)		
	42.3 ± 0.05	As-S		
	>43	As oxides		

a The parameters were derived from a self-consistent fitting procedure. The errors reflect the scattering of the fitting parameters between the spectra for different PEs. The assignments were performed in accordance with refs[44,55,58].

Weak contributions from oxidation were observed in the As3d (As_xO_y) and Ga3d (Ga_xO_y) spectra, in particular those taken at the PE of 130eV; this agrees with the analogous HRXPS results in previous paper, in which ODT film on GaAs performs the best quality.[44] The observed weak oxide-related features in these spectra are considered as one reflection of high quality ODT SAM on GaAs (001) surface, since highly ordered and densely packed SAM can passivate the GaAs substrate and simultaneously protect it from oxidation.[44,55,58] Note it is a reliable method to evaluate the film quality for SAMs on GaAs surface by monitoring the proportion of oxidation features in the respective As 3d and Ga 3d HRXPS spectra; this method will also be applied throughout this thesis.

Herein, it is necessary for us to trace the oxidation of GaAs surface: the pristine GaAs substrate is commonly covered with an oxidation layer (even though the wafer is preserved in Ar filled plastic package), which can be mostly removed during the etching step. The residual oxides can also be further exchanged through a "self-cleaning" process, which can be understood that the "O" atoms are replaced by the "S" atoms.[34] Keeping these in mind, the still existing oxidation constituents after SAM formation mainly come from three sources: (1) native oxides which can not be removed both in the etching and exchange (self-cleaning) steps; (2) residual oxides (after etching) which are not replaced in the exchange step; (3) post oxidation after the monolayer formation. Thus, the observed weak oxidation feature of ODT

SAM in Figure 4.2 is attributed to two effects: on one hand, the ODT molecules clean the residual oxides after etching effectively; on the other hand, the well ordered and densely packed ODT film passivates the GaAs surface and protects it from oxidation. Here, the final extent of oxidation is predominantly determined by the latter effect, since the protection can only work to a certain extent, and a partial penetration of airborne oxidative species (O_2, H_2O) was in principle possible, in particular taking into account that the samples were preserved for several days before the HRXPS measurements.

The binding information of the ODT molecules to GaAs substrate is provided in the S 2p HRXPS spectra, as presented in Figure 4.3 (a), along with the O 1s (b) and C 1s (c) comparison spectra of ODT SAM and etched GaAs substrate. In the S 2p spectra, only a single doublet at a characteristic BE position of ~162.5 eV (S $2p_{3/2}$) is observed, with no traces of unbound, disulfide or oxidized species. This BE value coincides with the analogous ones observed previously for both aliphatic and aromatic SAMs on GaAs (001),[44,55,56,58,59] which indicates ODT molecules bond to GaAs substrate through the conventional thiolate bond. Note the value of 162.5 eV is noticeably higher than that for the thiol-derived SAMs on noble metal substrates (162.0 eV),[7,100-102] presumably related to the screening of the photoemission hole by the substrate electrons in the case of metal. The fwhm of the doublet is 0.97 eV, this value is close to the reported one (∼1.1 eV) in the previous study,[44] but is much larger than the analogous values for the alkanethiolate SAMs on noble metal substrates (0.55-0.6 eV),[100] suggesting the higher inhomogeneity of the adsorption site geometry and exact bonding conditions at the SAM-GaAs interface.

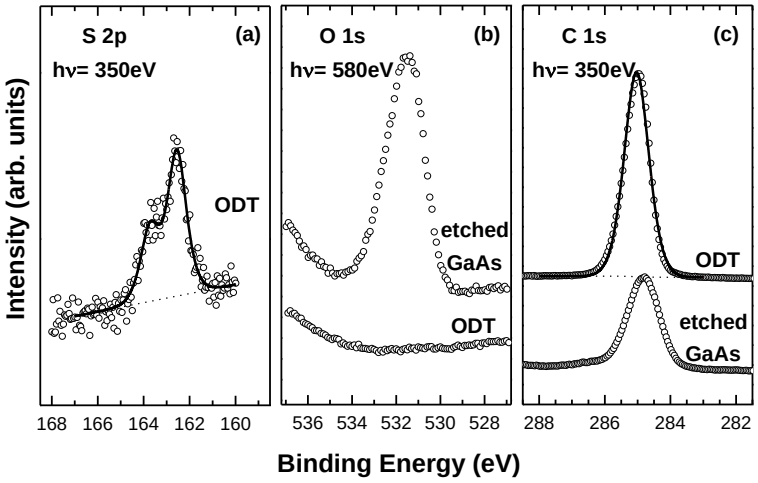

Figure 4.3: S 2p (a), O 1s (b) and C 1s (c) HRXPS spectra of ODT SAM on GaAs(001). In (b) and (c), the respective spectra of etched bare GaAs are also shown for comparison.

The O1s HRXPS spectra of ODT/GaAs exhibits no signal as compared to the etched GaAs, which coincides with the nearly oxidation free feature in the respective As 3d and Ga 3d spectra (Figure 4.1) acquired at the same photon energy (580 eV). In addition, formation of contamination-free ODT SAM is further supported by its C 1s spectra, which exhibits a single pronounced peak at a BE position of 285 eV, with no trace of oxidized carbon species, usually correlated to the contamination, being detected. Note this BE value is nearly the same with the analogous one for ODT/Au SAM (284.95 eV).[103]

4.1.2 NEXAFS spectroscopy

Carbon K-edge NEXAFS spectra of ODT/GaAs SAM acquired at X-ray incident angles of 90°, 55°, and 20° are presented in Figure 4.4, along with the difference between the 90° and 20° spectra. The spectra exhibit a C1s absorption edge related to C1s → continuum excitations and all characteristic absorption resonances of extended alkyl chains in an *all trans* conformation, namely a sharp resonance at ~287.8 eV and two broader resonances at ~293.4 eV and ~301.6 eV. The former resonance, denoted as R^*, is attributed to mixed valence Rydberg states[72,104] with a dominance of Rydberg states,[105,106] while the two latter resonances are commonly related to valence, antibonding C-C σ^* and C-C´ σ^* orbitals.[72,107] The molecular orbitals related to the R^* resonance are oriented perpendicular to the alkyl chains,[11,107,108] whereas the transition dipole moments (TDMs) of the orbitals corresponding to the C-C σ^* and C-C´ σ^* resonances are directed along the chain axis.[108] Thus, the orientations of these orbitals unequivocally determine the orientation of the alkyl chain in the ODT SAM.

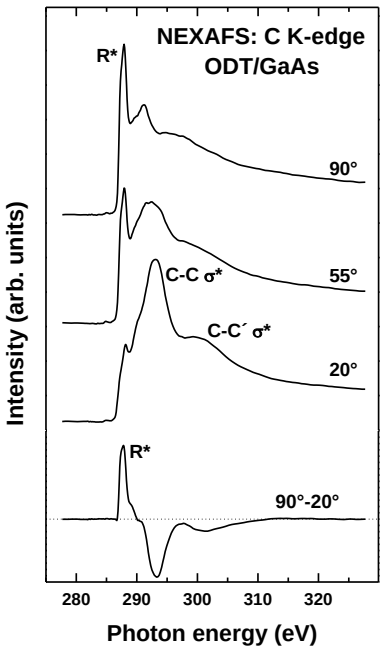

Figure 4.4: C K-edge NEXAFS spectra of ODT/GaAs SAM acquired at X-ray incidence angles of 90°, 55°, and 20°, along with the difference spectra. The spectra are normalized to the height of the absorption edge. The characteristic absorption resonances are marked.

The spectra exhibit pronounced dependence of the absorption resonance intensity on the incidence angle of X-ray, suggesting high orientation order of the ODT molecules on GaAs (001) substrate. Taking into account of the directions of the TDM of the R^*, C-C σ^* and C-C´ σ^* orbitals, the positive peak at the position of R^* resonance and the negative peaks at the positions of C-C σ^* and C-C´ σ^* resonances in the difference spectra indicate an upright orientation of the alkyl chains.

To determine the specific value of the average chain orientation in ODT SAM, a quantitative analysis was performed by measuring the intensity of the R* resonance as a function of the X-ray incidence angle, θ. The resulting dependence was then evaluated according to theoretical expressions (for a plane-type orbital):[72]

$$I(\gamma,\theta) = A\left\{P \times \tfrac{2}{3}\left[1 - \tfrac{1}{4}\cdot(3\cdot\cos^2\theta - 1)\cdot(3\cdot\cos^2\gamma - 1)\right] + (1-P)\times\tfrac{1}{2}\cdot(1+\cos^2\gamma)\right\} \qquad (4\text{–}1)$$

where A is a constant, P is a polarization factor of the X-rays, and γ is the angle between the sample normal and the normal of the molecular orbital plane, namely the tilt angle of the alkyl chain axis. Instead of absolute intensity values, the intensity ratios were analyzed, for example, in the ratio of $I(\theta)/I(20°)$, $I(\theta)$ and $I(20°)$ are the intensities of the R* resonance at X-ray incidence angles of θ and 20°. Figure 4.5 shows the angular dependencies of intensity ratios for the R* resonance for ODT SAM, along with the theoretical fits marked by the red solid line. The results yield average tilt angles of 14.6°, 16.8° and 16.8° when using the intensity ratio of $I(\theta)/I(20°)$, $I(\theta)/I(55°)$ and $I(\theta)/I(90°)$, respectively. Considering the standard error (± 3 − 5°) from the NEXAFS measurement and data evaluation procedure, these values agree with each other and coincide with the value (14.9°) reported by D. L. Allara et al..[34]

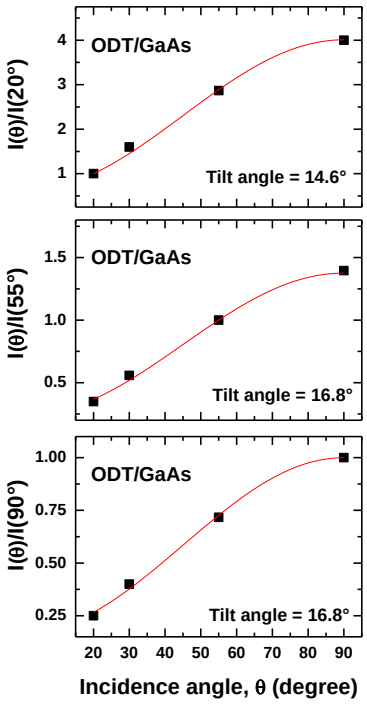

Figure 4.5: The angular dependence of the intensity ratios I(θ)/I(20°), I(θ)/I(55°), and I(θ)/I(90°) for the R* resonance for ODT/GaAs SAM (black filled squares), along with the best theoretical fits (red solid lines). The derived values of the average tilt angles are given.

In addition to the above standard evaluation procedure for R* resonance, the NEXAFS data was also processed using difference spectra upon subtracting two NEXAFS spectra recorded at X-ray incidence angles θ and 55°. For the vector type C-C σ* orbital, one obtains:[72]

$$I_V(\theta) - I_V(55°) = C_V\left(1 - {}^3/_2\, sin^2\,\alpha\right)(\cos^2\theta - \cos^2 55°) \qquad (4\text{–}2)$$

$I_\nu(\theta)$ and $I_\nu(55°)$ are the resonance intensities at X-ray angles of θ and 55°, α is the angle between the sample normal and the TDM of the vector orbital, and hence the tilt of the molecular chain. C_ν in the formula (4−2) is the normalization constant, depending on the cross section of the excitation from the C 1s core level into specific molecular orbital. Plots of the intensity difference of the C-C σ^* resonance, i.e. "$I_\nu(\theta) - I_\nu(55°)$", versus the parameter of ($\cos^2\theta - \cos^2 55°$) show highly linear dependencies for ODT/GaAs and HDT/Au SAMs, as illustrated in Figure 4.6. The respective slope value "$C_\nu(1\text{-}3/2\sin^2\alpha)$", which is function of the molecular orbital tilt angles "α", can be obtained after the linear fitting. Assuming 30° as the average tilt angle of the alkyl chain in the HDT/Au SAM, namely the tilt of C-C σ^* molecular orbital,[11,34,107,108] we calculate the constant C_ν for ODT/GaAs SAM, and obtain a value of 19° for the average tilt angle. Note here the slightly different value as compared to the previously reported one (~15°)[34] is presumably related to the non-absolute chain tilt (~27 − 35°) for the reference (HDT/Au) SAM.[7,10,109]

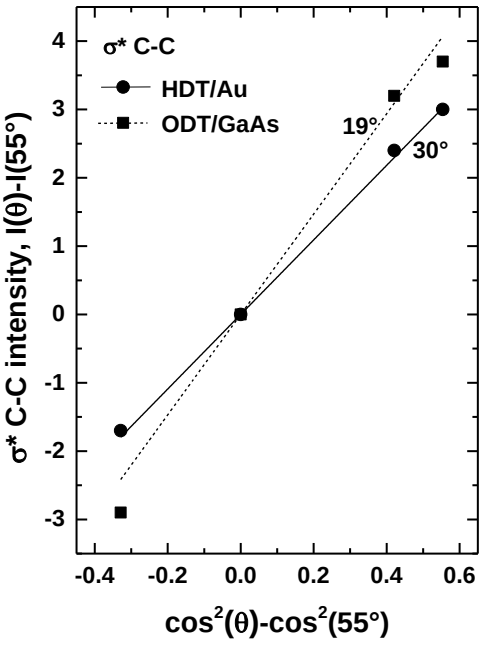

Figure 4.6: Plots of the intensities of the C-C σ^* difference peaks for HDT/Au (filled circles) and ODT/GaAs (filled squares) SAMs versus $\cos^2\theta$-$\cos^2$(55°) along with the respective linear fits (solid and dashed lines, respectively) using least-squares analysis. The derived average alkyl chain tilt angles are given at the respective fits. The data for HDT/Au are given for comparison. See text for details.

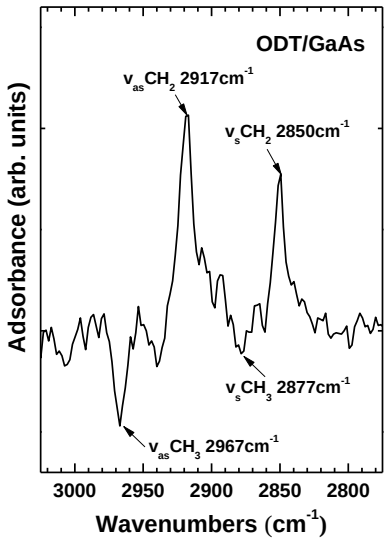

Figure 4.7: IR reflection spectra (80° angle of incidence) of the C-H stretching region for an ODT monolayer on GaAs (001). The characteristic bands are marked. Note no baseline correction and smooth operation are done on this spectra.

4.1.3 IRRAS

Figure 4.7 illustrates the IRRAS spectra of ODT SAM on GaAs (001), in which the characteristic bands, assigning to different C-H stretching modes, are marked: 2850 cm^{-1} for symmetric methylene (−CH_2−) stretching; 2917 cm^{-1} for asymmetric methylene (−CH_2−) stretching; 2877 cm^{-1} for symmetric methyl (−CH_3) stretching; and 2967 cm^{-1} for asymmetric methyl (−CH_3) stretching. The presence of both positive and negative absorbance features in the reflection spectra results from well-known effects involving strong perturbations of the

electric fields by the real part of the optical functions of the film in the case of dielectric substrates.[34,110] The first two distinct bands for $-CH_2-$ stretching modes locate at the same frequencies with those for ODT/Au SAM (2850 cm^{-1} and 2917 cm^{-1}),[7] and in particular, these two frequency values indicate the planar *all trans* conformation of the alkyl chain with a high degree of order.[10,109] Apart from this conformation, the twist angle, defined by the rotation of the plane containing the *all trans* carbon backbone with respect to the plane spanned by the chain axis and the surface normal, can be calculated from the intensity ratio of the asymmetric and symmetric modes following the RATIO method by Debe.[111] The resulting value of the twist angle is ~42°, which agrees quite well with the reported one (~43°).[34]

4.1.4 Ellipsometry: monolayer thickness

The NSAT SAMs ($C_nH_{2n+1}SH$) on GaAs (001) have been studied systematically by Single Wavelength Ellipsometry in the previous study by D. L. Allara et al.,[45] both 3-layer-model (air/SAM/GaAs) and 4-layer-model (air/hydrocarbon/S-GaAs interface/GaAs) have been used during measurements. In this thesis, to determine the thickness of ODT SAM, ellipsometry measurement was carried out using a isotropic 3-layer-model with the refractive index of 1.50 for the alkanethiolate moiety; a value of 21.5 Å was obtained, which agrees with the reported value (21 ± 2 Å).[34,45]

4.1.5 Contact angle: monolayer wetting property

The advancing (θ_a) and static (θ_s) contact angles were measured using a sessile drop mode, the results are 108° and 105° for θ_a and θ_s, respectively. As a reference, the respective contact angles of ODT/Au SAM were also measured, and the same results (108° and 105°) were obtained.

In addition, the advancing and static contact angles of the NSAT SAMs with different chain length on GaAs (001) were measured, and the results are summarized in Table 4.2. Firstly, this set of data indicates the hydrophobic character of these NSAT monolayers on GaAs, similar behavior was also observed for NSAT SAMs on metal substrate.[7] In addition to the general hydrophobic property, the decreasing contact angles (both θ_a and θ_s) with decreasing chain length also suggest the decaying film quality at going from ODT to DDT SAM.

Table 4.2: Advancing and Static Contact Angles of NSAT SAMs on GaAs (001)

	θa	θs
ODT	108°	105°
HDT	106°	102°
DDT	100°	97°

4.2 HDT SAM: comparable film quality with ODT SAM

The As 3d and Ga 3d HRXPS spectra of HDT SAM on GaAs (001) acquired at PEs of 580 eV and 300 eV are shown in Figure 4.8. As expected, low intensities of oxide-related signatures are observed in both As 3d and Ga 3d spectra, in particular those acquired at lower PE of 300 eV, corresponding to the smaller sample depth; this suggests the formation of high quality HDT SAM on GaAs (001) substrate. The spectra proportion for the oxides components in both As3d and Ga3d spectra (shoulders at higher BE side) is comparable to that in the case of ODT SAM (Figure 4.2), suggesting similar film quality of these two SAMs. In addition, similar like ODT SAM, a black doublet at ~42.4 eV, which is assigned to As-S species, is observed in the As 3d spectra of HDT monolayer, suggesting the As-S bond still as the predominant bonding fashion at the HDT-GaAs interface.

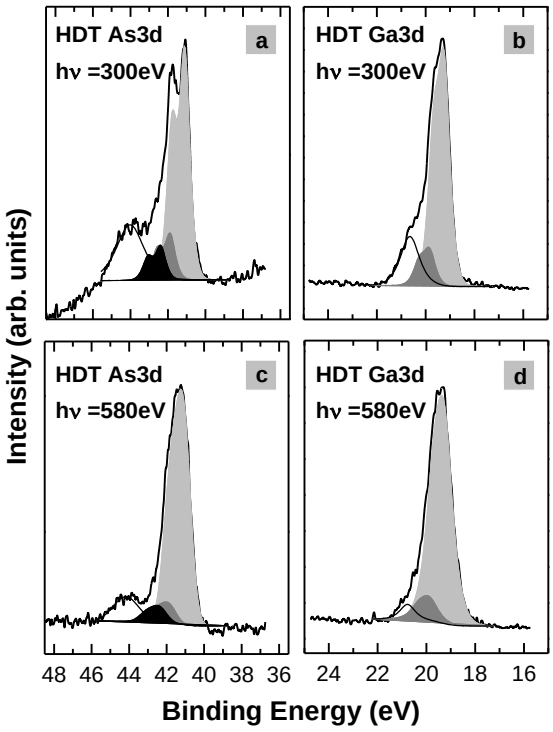

Figure 4.8: As 3d and Ga 3d HRXPS spectra of HDT SAM on GaAs(001). The spectra were acquired at photon energies of 300 eV (a and b) and 580 eV (c and d). The spectra are tentatively decomposed in several doublets related to individual chemical species. As 3d spectra: Light gray: stoichiometric GaAs; dark gray: elementary As; black: S-As. Ga 3d spectra: Light gray: stoichiometric GaAs; dark gray: Ga oxide or surface Ga 3d component. The shoulders at the higher binding energy side of the shadowed doublets correspond to As and Ga oxides. The assignments were performed in accordance with refs 44, 55, 58, 59.

The S 2p, O 1s, and C1s HRXPS spectra of HDT SAM are presented in Figure 4.9. The characters of these spectra have already been demonstrated in the study of ODT SAM (Figure 4.3). After comparing the respective spectra of HDT (Figure 4.9) and ODT (Figure 4.3) SAMs, it is found the spectral shape as well as the corresponding peak position are similar in both cases; this indicates: like ODT molecules, HDT molecules also form contamination free and densely packed SAM on GaAs (001) substrate. Note however, in the S 2p spectra (Figure 4.9a), a narrower $S2p_{3/2}$ (or $S2p_{1/2}$) peak is observed for HDT SAM (fwhm of 0.88eV versus 1eV), suggesting its more homogeneous bonding sites at the corresponding (HDT)SAM-GaAs interface.

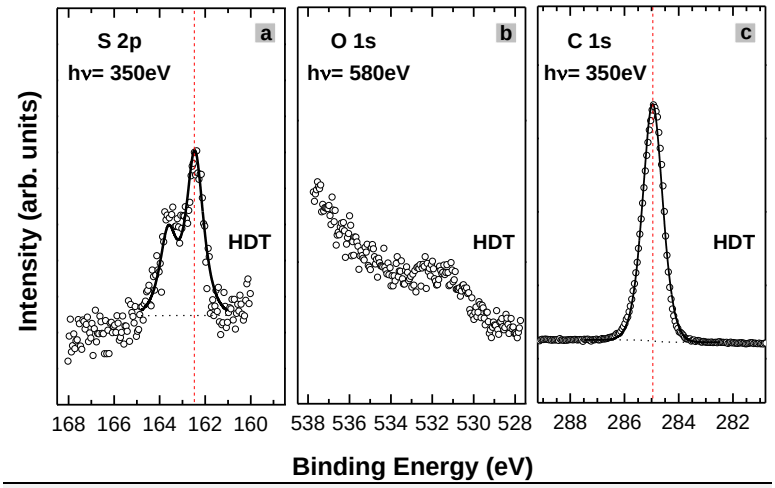

Figure 4.9: S 2p (a), O 1s (b) and C 1s (c) HRXPS spectra of HDT SAM on GaAs(001). The S 2p and C 1s spectra were fitted by a single doublet with branching ratio of 2:1 and a single peak, respectively.

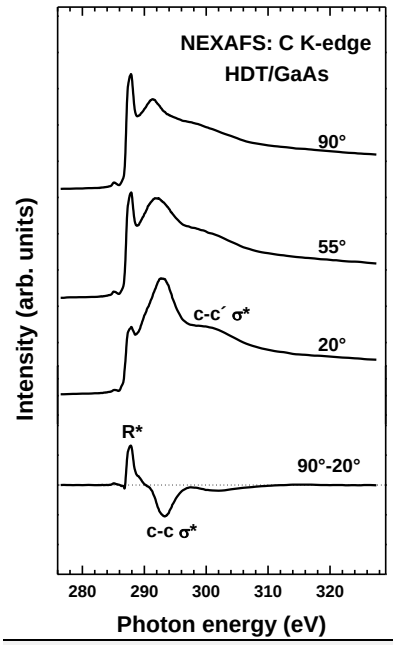

Figure 4.10: C K-edge NEXAFS spectra of HDT/GaAs SAM acquired at X-ray incidence angles of 90°, 55°, and 20°, along with the respective difference spectra. The characteristic absorption resonances are marked.

The Carbon *K*-edge NEXAFS spectra of HDT/GaAs SAM acquired different X-ray incidence angles are shown in Figure 4.10, along with the difference spectra between 90° and 20° incidences. Those spectra behave similarly like those of ODT/GaAs SAM, such as the characteristic adsorption resonances of R^*, C-C σ^*, and C-C´ σ^*, as well as their respective linear dichroism. Using the same, standard evaluation method mentioned above for ODT SAM, the orientation of the chain axis for HDT SAM was also obtained; the resulted value of the average tilt angle (18°) is quite close to that (17°) for ODT SAM.

4.3 DDT SAM

4.3.1 Film quality of DDT SAM

The good quality of DDT SAM is mainly revealed in its As3d and Ga3d XPS spectra, as shown in Figure 4.11. (Here, the factor of etching time during DDT sample preparation is considered in these spectra, and will be discussed later) These spectra exhibit weak oxide related signatures, viz. there is little spectra portion above the BE region of 43eV in the As3d spectra while the Ga3d spectra look symmetric showing quite weak shoulder-like feature at ~20.4 eV. However, compared with HDT and ODT monolayers, the coverage of DDT monolayer is much lower, which is supported by the C1s XPS spectra of these NSAT SAMs in Figure 4.12: the intensity of the C1s emission is much too low in the case of DDT SAM even after the consideration of its shorter chain length. In addition, the lower quality of DDT SAM is also supported by the corresponding lower contact angle values, as presented in Table 4.2.

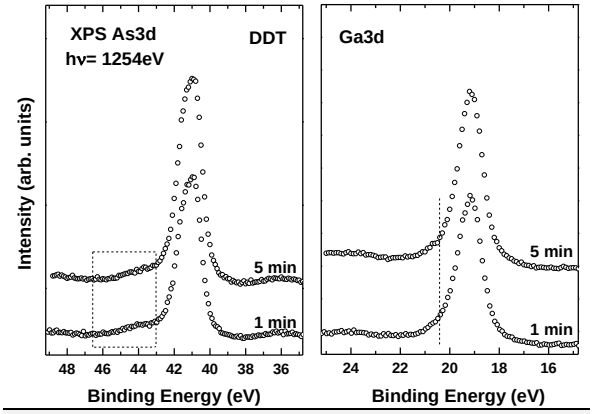

Figure 4.11: As 3d and Ga 3d XPS spectra of DDT SAMs on GaAs(001) prepared with etching time of 1 (bottom) and 5 minutes (top). All spectra were taken with a 0° (normal) photoelectron take-off angle. The oxide-related features are marked in the respective spectra.

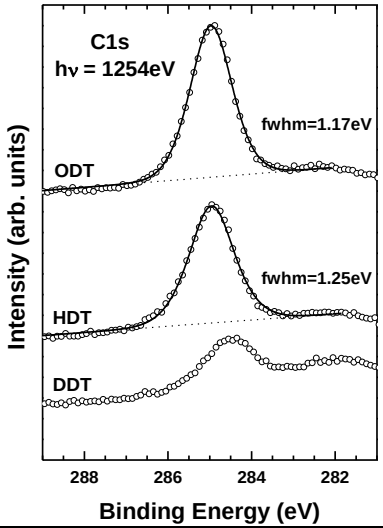

Figure 4.12: C 1s XPS spectra of ODT, HDT and DDT SAMs on GaAs(001). The respective spectra for ODT and HDT SAMs were fitted by a single peak, and the corresponding fwhm values are given.

The observed lower quality of DDT monolayer is due to the associated shorter chain length as compared to HDT and ODT monolayers, and this has been discussed in the previous study.[45] However, it is necessary for us to confirm this important finding and to rule out other effect such as the improper preparation procedure. For this purpose, varieties of procedures for preparing DDT samples were tried to check if the quality can be enhanced to a higher level. The optimized parameters during sample preparation include the etching time, incubation time, and ammonia amount, and they would be demonstrated as follows:

4.3.2 Optimizing preparation procedure for DDT SAM

The As 3d and Ga 3d XPS spectra of DDT SAM prepared with the etching time of 1 and 5 minutes are presented in Figure 4.11. There is nearly no difference between the respective As3d (or Ga3d) spectra for different etching time; they both exhibit weak oxidation related features, which implies that 1 minute etching is enough for the oxides layer removal, and the formation of DDT monolayer afterwards. In addition, the coverage is similar for DDT monolayers prepared with different etching time, which is supported by the similar intensities of the C 1s emission (not shown) as well as the emissions (As3d and Ga3d) from GaAs substrate. In reality, the wet etching, which induces microroughness to the GaAs surface,[112,113] is assumed to be aggressive to the GaAs substrate, hence the etching time of 1 minute is used for preparing NSAT SAMs in this thesis work.

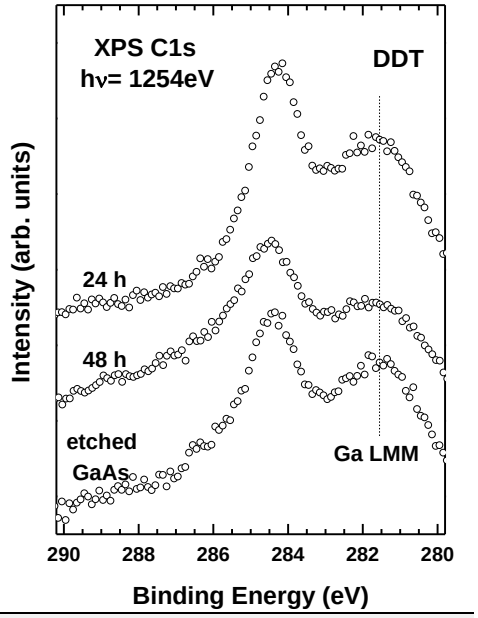

Figure 4.13: C 1s XPS spectra of DDT SAMs on GaAs(001) prepared under incubation time of 24 hours (top) and 48 hours (middle), along with the respective spectra for freshly etched bare GaAs (bottom) for comparison. All spectra were taken with a 0° (normal) photoelectron take-off angle. The interference emission from Ga LMM auger line is marked by the short dash line.

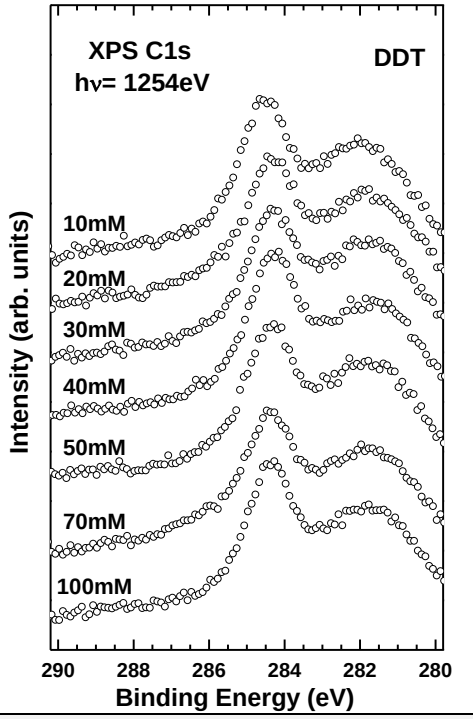

Figure 4.14: C 1s XPS spectra of DDT SAMs on GaAs(001) prepared with different ammonia concentration in the target solutions. All spectra were taken with a 0° (normal) photoelectron take-off angle.

The C 1s spectra of DDT SAMs prepared with the incubation time of 24 and 48 hours are shown in Figure 4.13, along with the spectra of etched GaAs substrate. The C 1s spectra of DDT SAMs exhibit a peak at ~284.3 − 284.4 eV, which is assigned to the hydrocarbon backbone. This peak is interfered to some extent by one emission at ~281.5 eV from the Ga LMM Auger line, while this interference emission is not detected in the case of HDT or ODT monolayer because it is covered by the intense C 1s peak. As seen, the C1s peak intensity is

the highest for the DDT monolayer incubated for 24 hours. When taking into account of the similar intensities of the As3d (or Ga3d) emissions (not shown), the DDT monolayer with better quality is obtained with the incubation time of 24 hours.

In addition to the factors of etching and incubation time, the amount of ammonium hydroxide is also an important factor affecting the quality of NSAT SAMs on GaAs.[114] To monitor the effect of this factor, the DDT samples were prepared in the target solution with different concentration of the ammonia hydroxide, ranging from 10 mM to 100 mM. The C 1s spectra of these DDT samples are compared in Figure 4.14, while they exhibit nearly no intensity difference. Since the intensities of the substrate (As3d or Ga3d) emissions are also similar for these samples, it can be concluded that the coverage (also film quality) of the DDT SAM can not be enhanced significantly by optimizing this factor. Considering the aggression character of ammonium hydroxide to the GaAs substrate, its concentration is set at 10 mM for preparing NSAT SAMs in this thesis.

Consequently, in section 4.3, DDT SAM with good quality can be obtained, and thus be able to protect the GaAs surface from oxidation. Nevertheless, this quality is lower as compared to that for HDT and ODT SAMs, which is related to the intrinsic property of DDT precursor, namely its shorter chain length. In addition, the quality of DDT monolayer can not be enhanced to a comparable level for ODT and HDT SAMs through optimizing the parameters based on the "standard" procedure[34]. The optimum procedure for preparing DDT SAM is: (1) etching time of 1 minute; (2) incubation time of 24 hours; (3) ammonia concentration of 10 mM.

4.4 Discussion

4.4.1 As-S bonding

As follows from the S 2p HRXPS spectra in Figure 4.3a and 4.9a, ODT and HDT molecules bond strongly to the bare GaAs (001) substrate through thiolate bond, the type of bonding commonly observed in alkanethiolate SAMs on metals.[7,100] The As3d HRXPS spectra reveals As-S bond as the predominant bonding mode, which agrees with previous studies for both aliphatic and aromatic SAMs on GaAs.[44,55,58] However, here we do not exclude the Ga-S bond, since existence of such bond is detected in the ToF-SIMS measurement of ODT SAM on GaAs (001);[44,48,49] and in particular highly ordered and densely packed ODT SAMs can be formed on GaAs (111A) surfaces, which are terminated

exclusively by Ga atoms.[33] In reality, the Ga-S bond is expected to be more energetically favorable than As-S bond from the thermochemical viewpoint.[115-119] This would be consistent with earlier work on other III-V (001) surfaces, where the thiolate species bond predominantly to the group III atoms:[35-38] for example, only In-S bond has been observed for alkanethiolate SAMs on InP;[35,36] and also the dominant In-S bond is found for the ODT SAMs on InAs surface.[37,38] In the present case, however, the dominant As-S bonding mode for these NSAT SAMs suggests the monolayer assembly process may be driven in a significant part by a kinetic factor, this can be understood more by discussing the "chain length effect" below.

4.4.2 Chain length dependence of the film quality

HRXPS and NEXAFS results demonstrate that ODT and HDT SAMs exhibit similar packing density and chain orientation, probably with a lower film order for the latter one, as deduced from the contact angle results in Table 4.2. By contrast, DDT SAM exhibits much lower quality compared with the former two films. To explain this, it is essential to understand one special factor in the molecular self-assembly on GaAs substrate but less important on Au and Ag substrates, viz. the ability of the GaAs substrate atoms to compliantly strain over distances of the molecular correlation lengths.[33] This allows the molecular packing to achieve the types of structures which are only possible on a structureless substrate, but with much shorter range order.[33] For example, ODT/GaAs(001) SAM can only form an incommensurate structure in a domain size of ~74 Å, which is only comparable to that for alkaneselenolate SAMs on Au (~60 – 75 Å)[120] and much smaller than that for alkanethiolate SAMs on Au (~250 Å).[45] The strain of the substrate surface atoms is primarily driven by the kinetic factor of "intermolecular interaction". For these NSAT SAMs, the chain packing energies would be reduced by the lower number of van der Waals interactions in the shorter chains, so similarly, as the packing force decreases due to the decreasing chain length, the ability of the intermolecular interactions to force restructuring of the GaAs substrate surface atoms, i.e. distortion of the surface lattice, would gradually decrease, thus leading to a film with decaying order and lower coverage, namely lower quality.

Summary of chapter 4

Highly ordered and densely packed ODT SAM has been formed on GaAs (001). ODT molecules bind to the substrate through thiolate bond, with predominantly bonding to As atoms. A full set of surface characterization techniques were applied to investigate its structure, and to confirm that its quality is comparable to the best reported one.[34] Thus, ODT SAM can serve as reliable reference system for other monolayers of this study.

In addition, two other NSAT SAMs with shorter chain length were also studied. One chain length effect for all SAM systems on GaAs was elucidated by discussing these NSAT SAMs: continuous deterioration of the film quality occurs with decreasing the chain length at going from ODT to DDT, which is especially pronounced in the case of DDT SAM.

Chapter 5: TPn and BPn SAMs on GaAs (001)

The presence of a substrate-dependent binding geometry at the anchoring group and its energetics (bending potential) are known to be important in determining the lateral density and structure of self-assembled monolayers (SAMs) of thiolates and selenolates on coinage metal substrates. In this chapter, we show that on the technologically important GaAs (001) surface a bending potential exists for thiolate adlayers as well. For this, two series of terphenyl- (TPn, n=0 – 6) and biphenyl- (BPn, n=1 – 6) substituted ATs (Scheme 1.1) were used as test model systems. As introduced in chapter 1, the odd-even effects in these TPn and BPn SAMs were well suitable for detecting the bending potential as well as its impact to the structure of these films.

5.1 TPn SAMs

5.1.1 Optimization of the preparation procedure for TPn/GaAs SAMs

In previous studies, the optimum procedure for preparing high quality aliphatic[34] and aromatic[55,58] SAMs on GaAs are different, so the procedure for preparing NSAT SAMs[34] can not be directly transferred to the TPn/GaAs system. To determine the best procedure for these TPn (also TP1-CN) precursors, varieties of procedures were tried; the samples prepared under these procedures were evaluated mainly by the synchrotron-based results, i.e. HRXPS and NEXAFS spectra, as a result of their higher surface sensitivity. Compared with the "standard" procedure (also for NSAT SAMs) given by D. L. Allara et al.,[34] our developed procedure for these TPn precursors has three major modifications: Firstly, the schlenk line setup was used instead of the glovebox; Secondly, the GaAs substrate was etched by concentrated HCl (37%) instead of concentrated $NH_3 \cdot H_2O$ (32%); Lastly, the samples were rinsed with a series of organic solvents after the monolayer formation. It is found the film quality can be improved significantly by these three modifications, which is supported by the HRXPS spectra, in particular.

(a) Schlenk line setup instead of glovebox:

The rigorous control of O_2 concentration for the molecular self-assembly on GaAs surface is essential, in particular considering the proneness of this substrate towards oxidation.[34] The O_2 concentration can be controlled below 5 ppm in the glovebox, however, the degassed solution together with the freshly etched GaAs transferred inside have to be exposed to normal atmosphere during their transportation into the glovebox; this transportation process would induce the oxidation of the GaAs substrate as well as the penetration of O_2 molecules into the degassed solution. The above issue can be solved by preparing the sample in a schlenk line setup, which can ensure that both the etching and immersion steps were carried out under inert atmosphere (Ar) protection.

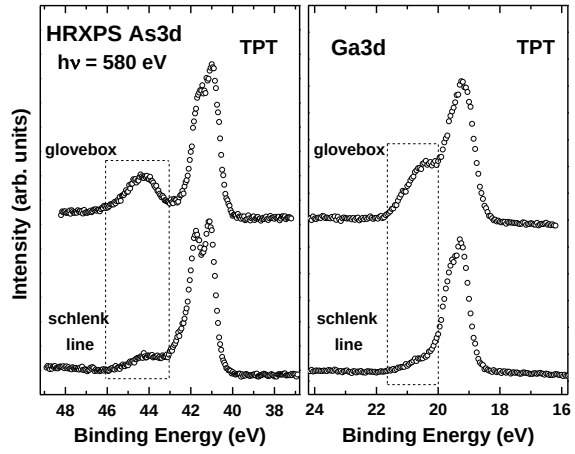

Figure 5.1: As 3d (left) and Ga 3d (right) HRXPS spectra of TPT SAMs on GaAs (001) prepared with the glovebox (top) and schlenk line (bottom) setup. The spectra were acquired at a photon energy of 580 eV. The oxide related features in As 3d (>43eV) and Ga 3d (>20eV) HRXPS spectra are marked.

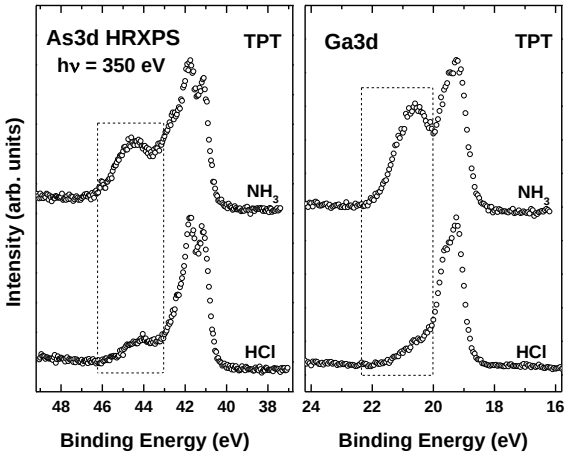

Figure 5.2: As 3d (left) and Ga 3d (right) HRXPS spectra of TPT SAMs on GaAs (001) prepared with concentrated $NH_3.H_2O$ (top) and HCl (bottom) etching methods. The spectra were acquired at a photon energy of 350 eV. The oxide related features in As 3d (>43eV) and Ga 3d (>20eV) HRXPS spectra are marked.

To compare the advantage of glovebox and schlenk line setup, TPT/GaAs SAM was chosen as a test example because of its relatively lower quality as compared to other TPn (n=1–6) films; this can be understood that the quality of the grown TPT monolayer would depend more on the modifying procedure. Note it has also been reported that introduction of an alkane spacer chain between the thiol headgroup and aromatic moiety results in higher structural quality for biphenyl-substituted alkanethiol SAMs on Au as compared to the non-substituted aromatic one.[121] Since the weak oxide related features in the As 3d and Ga 3d HRXPS spectra can be considered as reflection of the high quality SAMs on GaAs substrate,[44,55,58] the quality of the TPT film can be evaluated by the spectra proportion for these features in the respective spectra. As clearly seen in Figure 5.1, the TPT SAM prepared

with the schlenk line setup exhibits much weaker oxide related features in both As 3d (>43 eV) and Ga 3d (>20 eV) HRXPS spectra, suggesting the advantage of this setup for the sample preparation of TPn precursors.

(b) Etching with HCl (37%) instead of NH_4OH (32%)

The pristine GaAs is normally covered with an oxidation layer (even though preserved in Ar), which should be removed before incubating the GaAs into the target solution. The wet etching methods, including base and acid etching, were commonly used for removing this oxidation layer; the etching process happens so fast (~10 seconds), along with some additional surface microroughness. It has been shown the acid (HCl) etched surfaces are initially cleaner than the base ($NH_3 \cdot H_2O$) treated ones since they are free of chemisorbed –OH.[112] Moreover, the acid etching also generate more excess, reactive As sites.[122] In the previous studies for monolayer preparation on GaAs substrate, acid etching is commonly used for the precursors of aromatic thiols,[55,58] while base etching is usually used for the precursors of aliphatic thiols.[34] In the experiment, both these two etching methods were tested for the TPn/GaAs system. Here also, TPT/GaAs was selected as the test example, the As 3d and Ga 3d HRXPS spectra of the TPT SAM with the two etching methods are shown in Figure 5.2. (the TPT samples are both prepared using the schlenk line setup) As clearly seen, much less oxide-related signatures are observed in both As 3d (>43 eV) and Ga 3d (>20 eV) spectra for the TPT monolayer grown on the HCl (37%) treated GaAs substrate, indicating the corresponding higher film quality. Thus, acid etching is chosen for the preparation of the TPn SAMs in this thesis.

(c) Removal of physisorbed molecules with organic solvents

As a result of the bulky size (terphenyl moiety) of TPn molecules, they can easily attach on the formed TPn SAMs; these physisorbed species can not be removed by the normal rinsing with ethanol solvent, and would be detected in the S 2p HRXPS afterwards, as shown in Figure 5.3, the doublet at the BE position of ~163.5 eV is assigned to these species. (here TP3/GaAs sample was selected as an typical example) To remove these physisorbed species, the sample should be rinsed softly

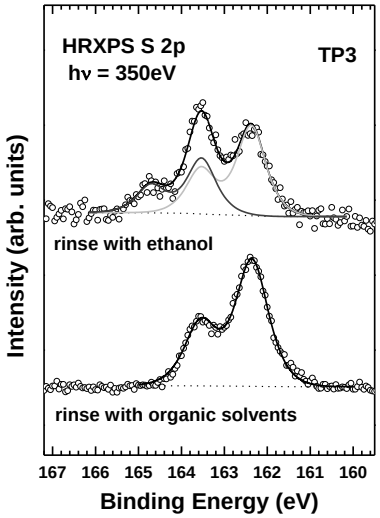

Figure 5.3: S 2p HRXPS spectra of TP3 SAMs on GaAs (001) using different rinsing methods after sample incubation: ethanol (top) and organic solvents (bottom).

with series of organic solvents after incubation, in a sequence of ethanol, acetone, chloroform and then ethanol. Note that, the polar organic solvents of acetone and chloroform are both aggressive to GaAs surface or the grown monolayer, or probably both; so the rinsing should be performed softly. The S 2p HRXPS spectra of the TP3/GaAs sample, which is rinsed with different organic solvents after incubation, is also presented in Figure 5.3, with no trace of physisorbed molecules (~163.5 eV) being observed.

5.1.2 Spectroscopy characterization of TPn SAMs: HRXPS

The formation of high quality TPn (n=0 – 6) and TP1–CN SAMs was, in particular, manifested by the As 3d and Ga 3d HRXPS spectra, as presented in Figure 5.4. These spectra can be decomposed into individual spectral components, with the parameters and assignments given in Table 5.1. The spectra are dominated by the signals from stoichiometric GaAs (light gray doublets), which are accompanied by much weaker contributions from elementary As (dark gray doublets in As 3d spectra) and surface states (dark gray doublets in Ga 3d spectra). In addition, a black doublet assigned to As–S could be traced at ~42.3 eV (As $3d_{5/2}$) in the As 3d spectra, which means that the TPn molecules are preferably bonded to the As atoms. Note that even though the conclusion regarding the dominance of As–S bond agrees well with previous studies,[44,55,58] bonding to the Ga atoms cannot be completely excluded.[44,48,49]

Along with the above characteristic features, there are weak signals related to oxides (As_xO_y and Ga_xO_y) at ~44.3 eV and ~20.7 eV, respectively. In spite of all efforts, we have not succeeded in eliminating the oxides completely. They could be residuals from the etching procedure and self-cleaning process[44] during the SAM formation but most likely appeared as a result of post-oxidation, during the transport and handling of the samples. Even though the GaAs surface was protected by the SAMs, this protection worked presumably to a certain extent only, so that a partial penetration of airborne oxidative species (O_2, H_2O) was in principle possible. The small extent of oxidation suggests, however, dense molecular packing in the SAMs.[55,58]

In addition to the general weak oxidation signatures of these TPn SAMs, the spectral portion related to the oxide-related species exhibits an odd-even variation: this proportion is higher for the TPn (n=0 – 6) SAMs with an even (n) number of methylene units in the aliphatic linker, with only an exception of TP6. The larger extent of oxidation in the respective As3d and Ga3d spectra suggests the corresponding, less dense TPn films (even n) on the GaAs surface.

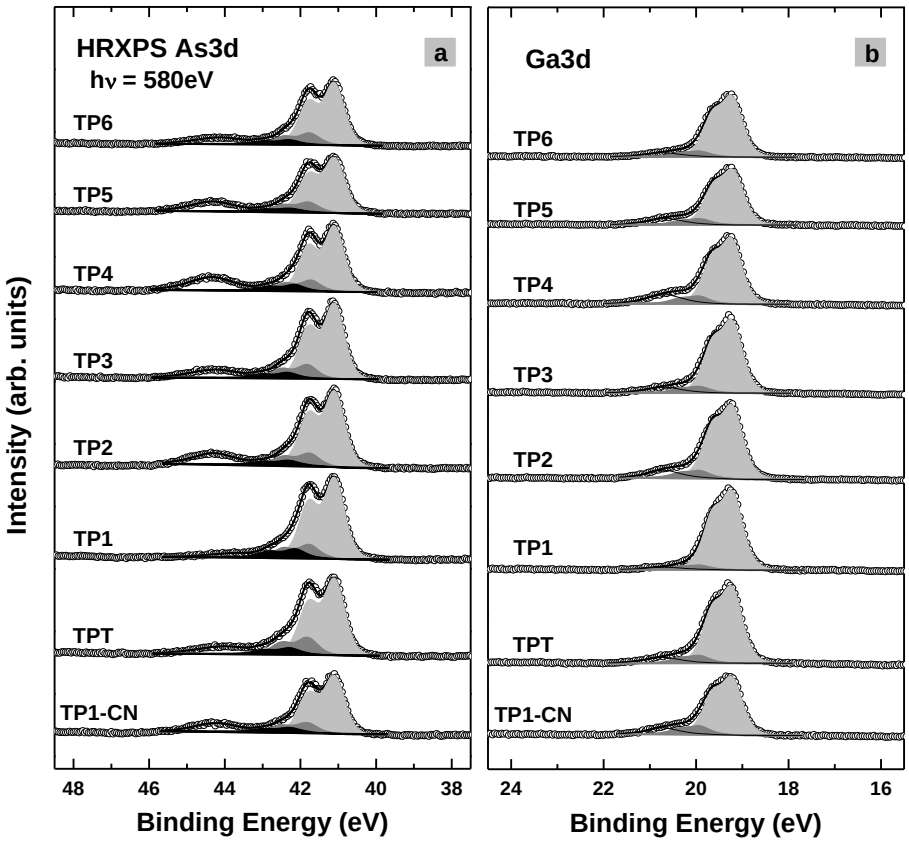

Figure 5.4: As 3d (a) and Ga 3d (b) HRXPS spectra of TPn (n = 0 - 6) and TP1-CN SAMs on GaAs(001). The spectra were acquired at a photon energy of 580 eV. The spectra are decomposed in several doublets related to individual chemical species: (a) As 3d spectra: Light gray: stoichiometric GaAs; dark gray: elementary As; black: S-As. (b) Ga 3d spectra: Light gray: stoichiometric GaAs; dark gray: Ga oxide or surface Ga 3d component. The shoulders at the higher binding energy side of the shadowed doublets correspond to As (a) and Ga (b) oxides. The assignments were performed in accordance with refs 44, 55, 58.

Table 5.1: Parameters of Individual Emissions in the Ga 3d and As 3d Spectra in Figures 5.4[a]

core level	binding energy (eV)	assinment	fwhm (eV)	spin-orbit splitting (eV)	branching ratio
Ga $3d_{5/2}$	19.21 ± 0.02	GaAs	0.50 ± 0.02	0.43	3/2
	19.8 ± 0.1	Ga_2O_3 or surface Ga3d component			
	>19.8	Ga oxides			
As $3d_{5/2}$	41.1	GaAs	0.61 ± 0.02	0.69	3/2
	41.77 ± 0.05	elementary As			
	42.29 ± 0.05	As-S			
	>43	As oxides			

a The parameters were derived from a self-consistent fitting procedure. The errors reflect the scattering of the fitting parameters between the spectra for different samples and different PEs. The assignments were performed in accordance with refs[44, 55, 58]

Formation of contamination-free and densely packed TPn (n=0 – 6) and TP1-CN SAMs were further supported by the S 2p and C 1s HRXPS spectra, as shown in Figure 5.5a and b, respectively. All the S 2p spectra exhibit a single S $2p_{3/2,1/2}$ doublet at the position of ~162.4 ± 0.1 eV, which is commonly assigned to the thiolate-type sulfur bonded to the GaAs surfaces; and no traces of unbound, disulfide, or oxidized species are observed in the spectra. The BE values coincide with the analogous ones for both aliphatic[44] and aromatic[55,56,58] SAMs on GaAs. In addition, the fwhm values of the S $2p_{3/2}$ and S $2p_{1/2}$ peaks for these TPn SAMs (~0.77 ± 0.03 eV) is lower than that (~1 eV) for ODT/GaAs SAM, suggesting the more homogenous binding site geometry for these TPn films, since the fwhm value is a fingerprint of the homogeneity of the adsorption sites for the sulfur head groups.

The C 1s spectra for TPn/GaAs (n=1–6) SAMs show a main emission peak at BE positions of 284.3 – 284.4 eV (284.6 eV for TPT/GaAs) assigned to the terphenyl backbone, and a shoulder at ~0.6 eV higher BE, while no trace of contamination could be detected, so that its content is considered as very low. Note that the shoulder has been observed previously for different aromatic SAMs[76] and TPn SAMs in particular[21,22]. It is alternatively assigned to the carbon atom bonded to the sulfur headgroup or to shake-up process. As the probing depth of HRXPS is rather small at the given photon energy, the former assignment seems to be rather questionable and an assignment to shake-up process is more likely.

The C 1s spectra for TP1-CN/GaAs SAM differs from those for TPn SAMs mainly in two aspects: on one hand, the main peak assigned for the aromatic backbone locates at somewhat higher BE position (~284.9 eV), which is attributed to the introduction of nitrile group to the end of terphenyl backbone. On the other hand, the shoulder at the BE position of ~286.4 eV is assigned to the nitrile carbon atom instead of shake-up process.[123] Note, the above BE values of both the main peak (284.9 eV) and the shoulder (286.4 eV) for TP1–CN/GaAs SAM agree with those reported for biphenylnitrile-based SAMs ($NC(C_6H_4)_2(CH_2)_nSH$ n=0 – 2) on Au.[123]

The O1s spectra of TPn/GaAs SAMs (n=0 – 6) are presented in Figure 5.6, these spectra exhibit weak signal or nearly no signal (TPT, TP1, TP6), which correlates with the low intensities of the oxide-related signatures in the respective As 3d and Ga 3d spectra (Figure 5.4) taken at the same photon energy (580 eV). The weak signal appearing in these O 1s spectra further proves the formation of densely packed TPn SAMs on GaAs, which can passivate the surface and protect it from oxidation.

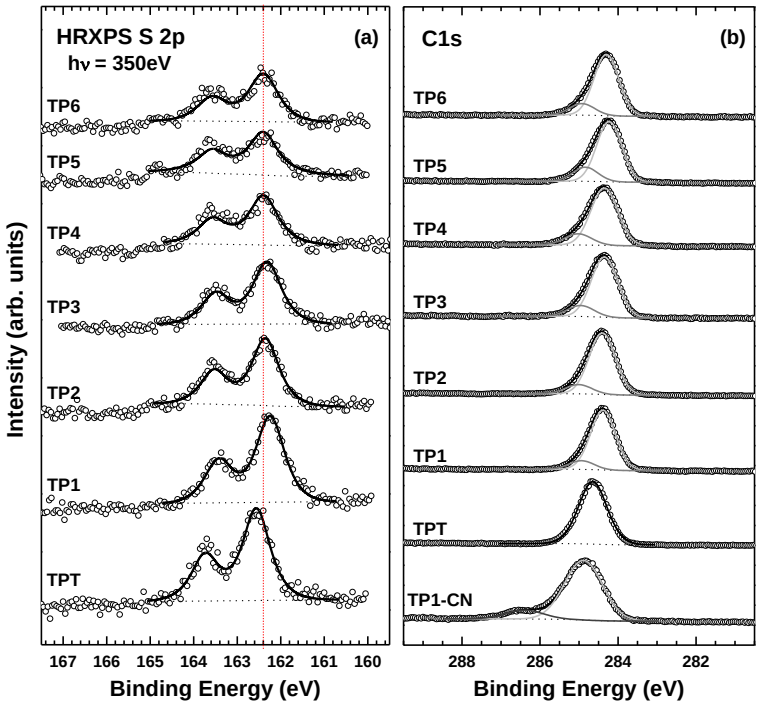

Figure 5.5: S 2p (a) and C 1s (b) HRXPS spectra of TPn (n = 0 - 6) and TP1-CN (only in b) SAMs on GaAs(001). The spectra were acquired at a photon energy of 350 eV.

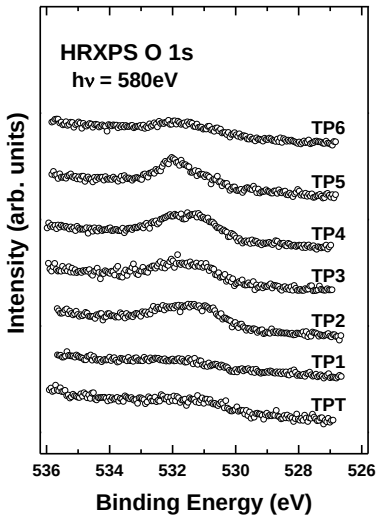

Figure 5.6: O 1s HRXPS spectra of TPn (n = 0 - 6) SAMs on GaAs(001). The spectra were acquired at a photon energy of 580 eV.

5.1.3 Spectroscopy characterization of TPn SAMs: NEXAFS spectroscopy

A typical C *K*-edge NEXAFS spectra of a TPn SAM (taking TP5/GaAs as an example) is presented in Figure 5.7, in which individual absorption resonances are marked. The spectra was acquired at a "magic" angle of 55°, in this angle, the spectra is exclusively representative of the electronic structure of the investigated film.[72] The assignments and positions of these resonances are given in Table 5.2 (next page).

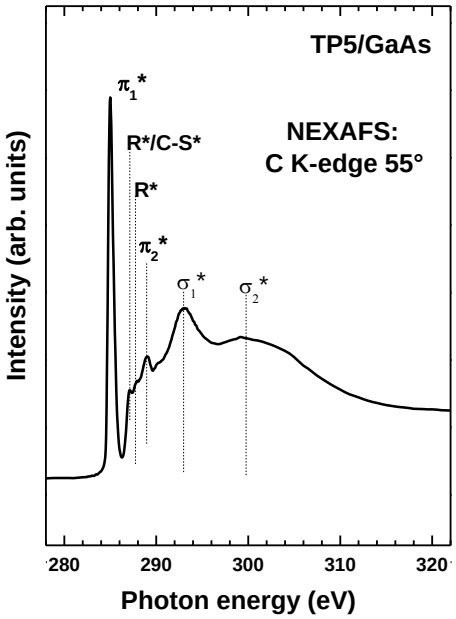

Figure 5.7: C K-edge NEXAFS spectra of TP5 SAM on GaAs (001) acquired at an X-ray incident angle of 55°. Individual absorption resonances are shown.

Table 5.2: Assignments and Positions of the Characteristic NEXAFS Resonances in TPn/GaAs (001)

resonance assignment[a]	π_1^*	R^*/C-S^*	R^*	π_2^*	σ_1^*	σ_2^*
resonance positions[b] (eV)	285	287	287.6	288.9	292.8	300

[a]The resonance assignment is performed in accordance with refs 21. [b]There is no noticeable variation in the resonance position among the TPn films.

The C *K*-edge NEXAFS spectra of the TPn (n=0 – 6) SAMs taken at this magic angle are shown in Figure 5.8a. As clearly seen, these spectra are dominated by the intense π_1^* resonance of the phenyl rings, whereas the R^* resonance characteristic for the aliphatic chains can not be clearly distinguished since it overlaps with the absorption edge. No features related to contamination could be traced, including a sharp resonance of COOH (typical component of adventitious carbon) at ~288.5 eV.[55]

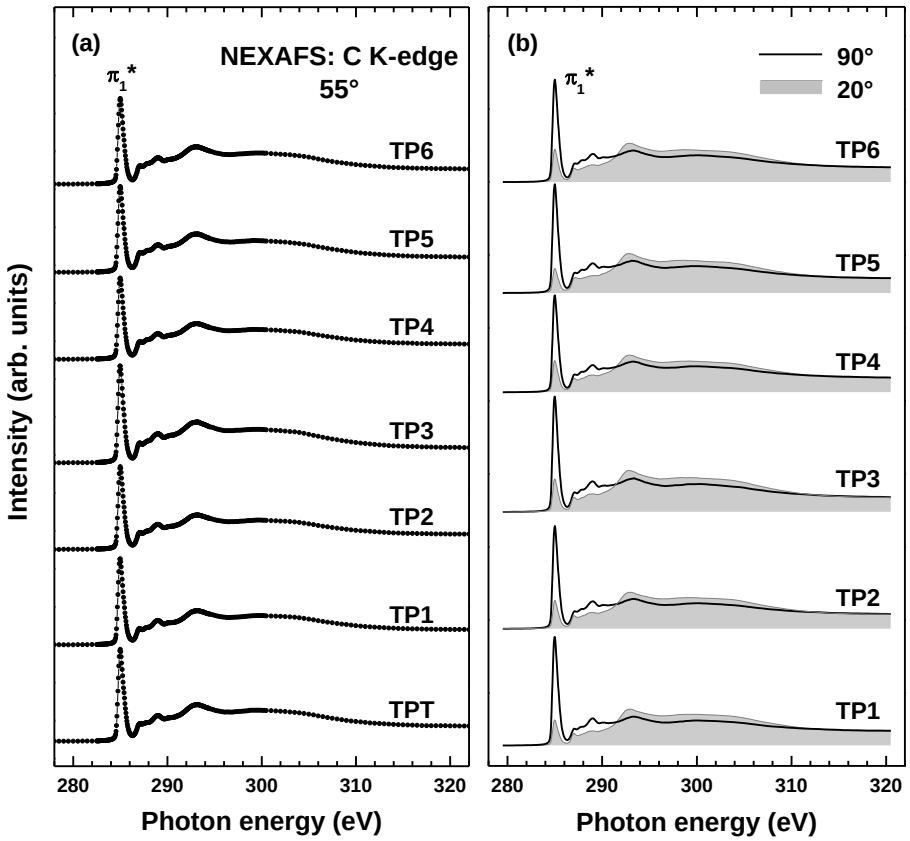

Figure 5.8: C K-edge NEXAFS spectra of TPn (*n* = 0 – 6 for (a) and n = 1 – 6 for (b)) SAMs on GaAs (001) acquired at an X-ray incident angle of 55° (a) as well as at normal (90°) and grazing (20°) incidence of X-rays (b). The characteristic π_1^* resonance is indicated.

Apart from the electronic structure, molecular orientation in TPn SAMs was monitored, relying on the linear dichroism in X-ray absorption, i.e., dependence of the absorption cross-section on the relative orientation of the molecular orbital and electric field vector of linearly

polarized X-rays.[72] In Figure 5.8b, the C *K*-edge NEXAFS spectra of these films acquired at normal (90°) and grazing (20°) X-ray incidence are depicted; they exhibit pronounced linear dichroism of the π_1^* resonance. Considering that the transition dipole moment (TDM) of this resonance is perpendicular to the plane of the phenyl rings, its larger intensity at normal incidence suggests the upright orientation of the terphenyl moieties in these TPn films. More importantly, the larger intensity difference between the spectra acquired at 90° and 20° incidence angles observed for odd n implies the odd-even variation in the orientation of the terphenyl moieties − a fingerprint of the bending potential.

The orientation of the terphenyl moieties can be numerically evaluated using the entire set of the NEXAFS spectra and a standard evaluation procedure.[72] For this purpose, the intensity of absorption resonances *I* was monitored as a function of the X-ray incidence angle θ. The π_1^* resonance was selected due to its strong intensity. In order to extract its intensity from the experimental spectra, the entire spectra series were self-consistently fitted by several Gauss peaks representing the observed resonances listed in Table 5.2 and by one absorption edge (the standard shape)[72] related to the C1s → continuum excitation.[72] The positions and widths of the fitting peaks were determined from the difference spectra (90°–20°) following the procedure described by Outka et al.[107] and Hähner et al.[11] As an example, the decomposition of the C *K*-edge NEXAFS spectra of TP5/GaAs SAM acquired at the magic (55°) angle is presented in Figure 5.9.

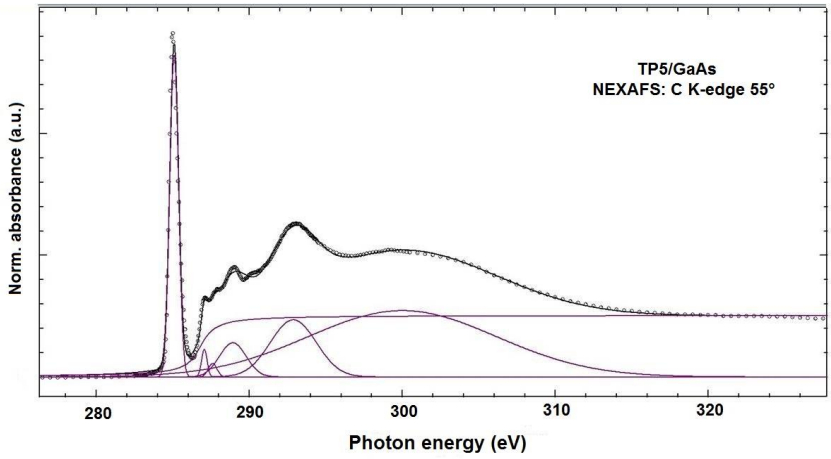

Figure 5.9: C K-edge NEXAFS spectra of TP5 SAM on GaAs (001) acquired at an X-ray incident angle of 55° along with the respective fit (purple line). The positions of the individual absorption resonances are in accordance with Table 5.2 (see text for detail).

After extracting the intensities of π_1^* resonance in the entire set of NEXAFS spectra, the resulting dependence of I and θ were evaluated according to the theoretical expression (for a vector-type orbital):[72]

$$I(\alpha,\theta)=A\left\{P\times\frac{1}{3}\left[1+\frac{1}{2}\cdot(3\cdot\cos^2\theta-1)\cdot(3\cdot\cos^2\alpha-1)\right]+(1-P)\times\frac{1}{2}\cdot(\sin^2\alpha)\right\} \quad (5-1)$$

where A is a constant, P is a polarization factor of the X-rays, and α is the average tilt angle of the molecular orbital. To avoid normalization problems, not the absolute intensities but the intensity ratios $I(\theta)/I(90°)$ were analyzed,[72] where $I(\theta)$ and $I(90°)$ are the intensities of π_1^* resonance at X-ray incidence angles of θ and 90°, respectively. The intensity ratios of $I(\theta)/I(20°)$ and $I(\theta)/I(55°)$ were also analyzed. As an example, the resulting dependences of TP5/GaAs SAM are presented in Figure 5.10 together with the best theoretical fits.

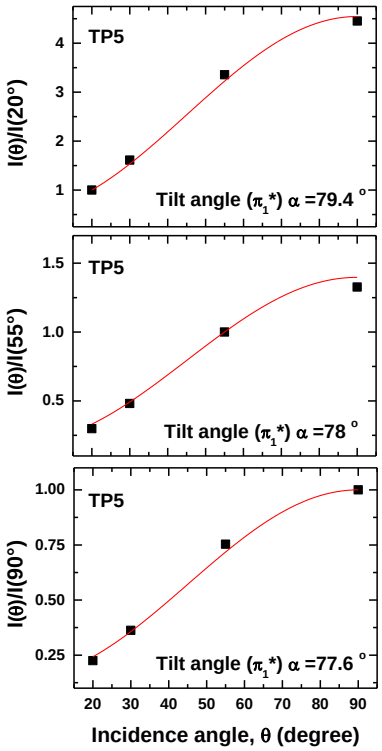

Figure 5.10: The angular dependence of the π_1^* resonance intensity ratios I(θ)/I(20°), I(θ)/I(55°), and I(θ)/I(90°) for TP5 SAM on GaAs (001) (black filled squares), along with the best theoretical fits (red solid lines). The derived values of the average tilt angles are given at the respective fits.

After knowing the tilt angle of the molecular orbital (α) through evaluating the NEXAFS data, the average tilt angle of the terphenyl moiety (β) can be calculated through the equation:

$$\cos(\alpha)=\sin(\beta)\cos(\gamma)^{79} \quad (5-2)$$

which is suitable for a variety of aromatic SAMs. In this equation, "γ" is the twist angle of the aromatic backbone, which defines the rotation of the plane containing the terphenyl backbone with respect to the plane spanned by the surface normal and molecule axis. The twist is estimated at 45% using a nitrile-terminated terphenyl (TP1-CN) SAM.[79] Note like the TPn molecules, the backbone of the TP1-CN molecule is consisted of three phenyl rings, hence it is reasonable to assume the same twist for all these terphenyl-based (TPn and TP1-CN) SAMs. The detailed procedure about how to get the twist will be introduced in next section (5.1.4).

5.1.4 Probing the twist angle for TPn SAMs using TP1-CN SAM

The twist angle of the aromatic backbone for TPn SAMs can be derived through evaluating the NEXAFS data of TP1-CN/GaAs sample, assuming TPn and TP1-CN monolayers have the same twist in the aromatic moiety. The presence of the nitrile tailgroup in the target molecules is a crucial point since this group possesses two mutually perpendicular π^* orbitals, which, due to the hybridization with the π^* orbitals of the phenyl rings, are oriented either perpendicular (π_1^*) or parallel (π_3^*) to the ring plane.[79] Further, the energies of these two orbitals are different,[79] so that the orientation of their TDMs can be independently derived.

The C *K*-edge and N *K*-edge NEXAFS spectra acquired with varying the X-ray incidence angles are shown in Figure 5.11. The former spectra are dominated by the π_1^* resonance typical for the aromatic backbone, while the latter ones are dominated by the π_1^* and π_3^* resonances related to the −CN group[124] at 398.5 and 399.5 eV, respectively. Both the C and N *K*-edge spectra exhibit noticeable linear dichroism, which is a clear signature of the orientational order in the TP1-CN SAM.

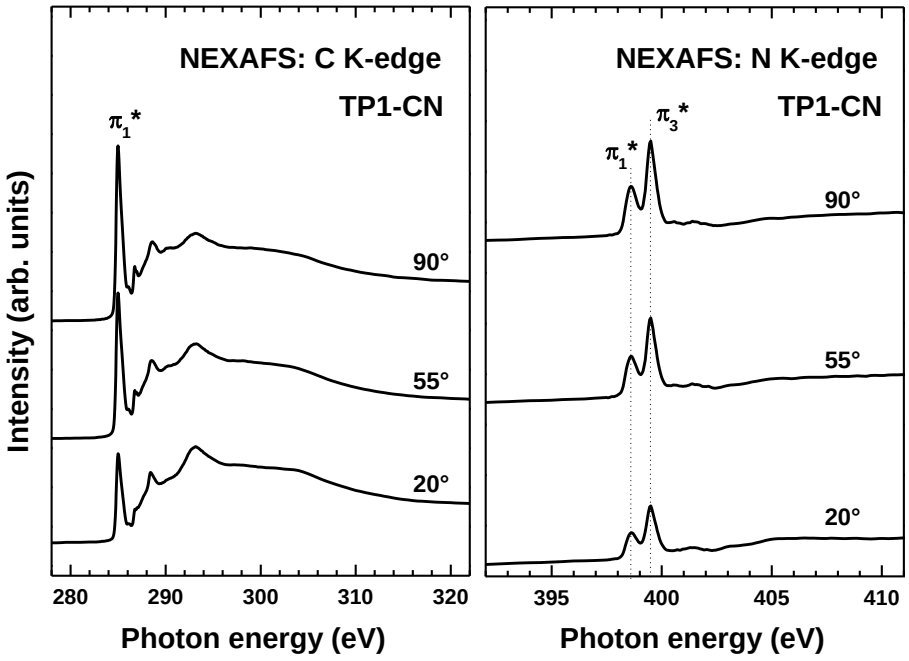

Figure 5.11: Carbon *K*-edge (left) and Nitrogen *K*-edge (right) NEXAFS spectra of TP1-CN SAM on GaAs (001) acquired at X-ray incidence angles of 90°, 55° and 20°. The most prominent absorption resonances are marked.

The average tilt angles of all relevant π^* orbitals, α, could be directly obtained from a quantitative analyze of the entire set of the NEXAFS spectra acquired at different X-ray incidence angle, θ, according to the theoretical equation (5−1) for a vector type orbital. The derived tilt angles for π_{ph}^* in the phenyl part (α_{ph}) as well as π_1^* (α_1) and π_3^* (α_3) in nitrile end group were all listed in Table 5.3.

Table 5.3 Tilt and Twist Angles (°) of TP1-CN SAMs on GaAs (001) and Au derived from the NEXAFS data (accuracy ± 3~5°)

	GaAs	Au
tilt angle of the π_1^* orbital (phenyl) α_{ph}	65.8	67.3
tilt angle of the π_1^* orbital (CN) α_1	64.4	68.1
tilt angle of the π_3^* orbital (CN) α_3	64	66.3
twist angle (γ) from α_1 and α_3	45.4	47.1
molecular tilt (β) from α_1 and α_3	38	33.3
molecular tilt (β) from α_{ph} and $\gamma(\alpha_1, \alpha_3)$	35.7	34.5

Since the TDMs of the π_1^* orbitals of the phenyl rings and the −CN group are collinear and perpendicular to the ring plane, the average tilt angle of the aromatic moiety can be calculated according to equation (5−2): $\cos(\alpha)=\sin(\beta)\cos(\gamma)$ with the twist angle γ also unknown. For the π_3^* orbital of the CN group, with the TDM within the ring plane, equation (5−2) should be modified to:

$$\cos(\alpha_3)=\sin(\beta)\cos(\pi/2-\gamma) \qquad (5-3)$$

Thus, combining two equations (5−2) and (5−3), we can get the molecular tilt angle β and twist angle γ, the two values were given in Table 5.3. Further, the derived twist angle (γ) can be used to calculate the molecular tilt β on the basis of α_{ph}, according to equation (5−2). The calculated value agrees well with the molecular tilt value derived from equations (5−2) and (5−3) on the basis of α_1 and α_3. In Table 5.3, the respective values of the tilt or twist angles

for TP1-CN/Au (values taken from Ref [79]) are also listed and compared with the values for TP1-CN/GaAs, it is found they are close to each other, suggesting the similar structure of the aromatic backbone for the TP1-CN SAMs on these two substrates.

Note here, during the twist angle probing process, a planar conformation of the aromatic backbone is assumed, however, if the phenyl rings are twisted differently as in the molecular state (torsion), the derived twist (45°) then represents the average twist of the phenyl rings in the aromatic backbone.

5.1.5 Odd-even effect for TPn SAMs

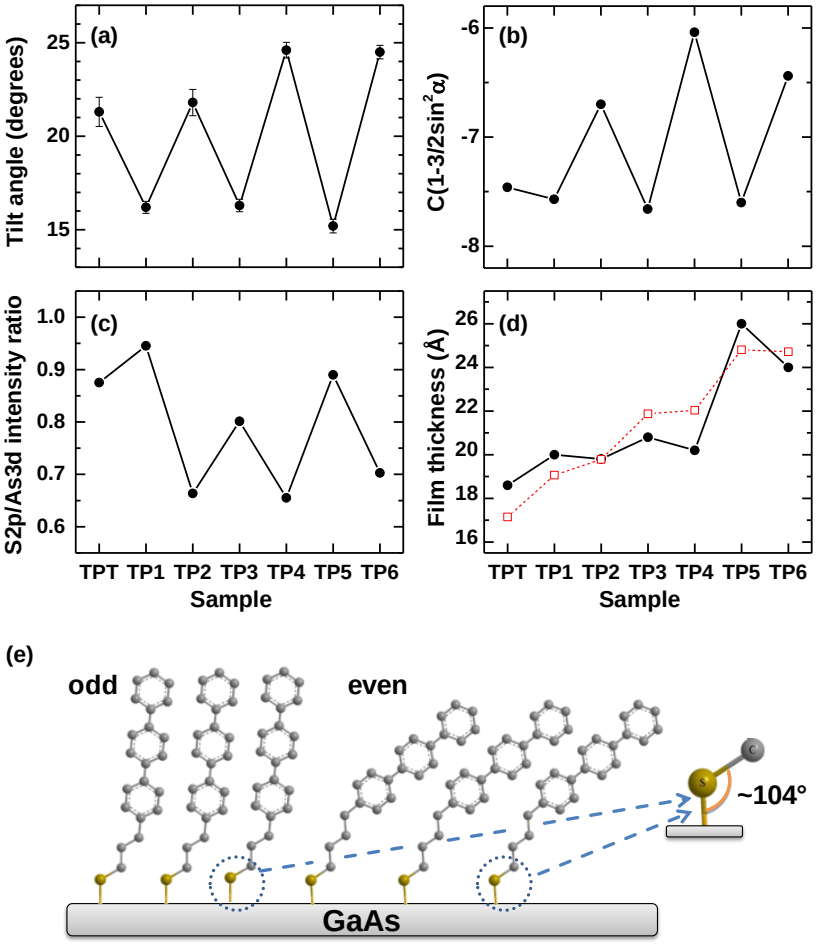

Figure 5.12: Derived parameters of TPn SAMs on GaAs(001): (a) The average tilt angles of the terphenyl backbones; (b) a proportionality factor $C(1-3/2\sin^2\alpha)$ determined from the difference NEXAFS spectra – a fingerprint of the average tilt angle α of the π_1^* orbital; (c) S2p/As3d intensity ratio; (d) effective thickness, as measured by XPS (filled black circles) and as calculated based on the tilt and molecular structure (red open circles; scaled up by a factor of 1.15); and (e) a schematic structural picture. The data for the SAMs of TPT ($C_6H_5(C_6H_4)_2SH$) are shown as well – for comparison. The intensity ratio in (c) is normalized to the analogous value for the ODT SAM. The higher absolute values for the XPS-derived thickness are presumably related to the possible difference in the attenuation lengths of the photoelectrons for alkanethiolate and TPn SAMs and to a possible uncertainty in the thickness of the reference ODT/GaAs sample.[34]

The C *K* edge NEXAFS spectra acquired at incidence angles of 90° and 20° in Figure 5.8b has provided evidence for the odd-even variation in the orientation of the terphenyl moieties; The qualitative considerations were complemented by the numerical analysis of the NEXAFS data, further to obtain the average tilt angles of the aromatic backbones. Following the established theoretical procedure talked above, the derived values of the average tilt angles of the terphenyl backbones in TPn SAMs are shown in Figure 5.12a. (a twist of 45° is assumed for the terphenyl backbone) These values exhibit a systematic zigzag variation (6°–10°) with varying length of the aliphatic linker: smaller molecular inclination is observed for odd n, while larger inclination occurs at even n.

An independent demonstration of this behavior was provided by an alternative evaluation procedure of the NEXAFS data, relying on the difference spectra.[72,125] As described in literature,[72] the difference in the intensity of a particular resonance at angles θ_1 and θ_2, $I_v(\theta_1) - I_v(\theta_2)$, is proportional to the parameter ($\cos^2\theta_1 - \cos^2\theta_2$), with a proportionality factor C(1-3/2$\sin^2\alpha$), where α is the average tilt angle of a given molecular orbital and C is a constant which depends on the excitation probability from the core level into this orbital. Since this probability is the same for all TPn molecules as far as the π_1^* orbital related to the common terphenyl building block is considered, the proportionality factor is a measure of molecular tilt, even though the exact value of C is not known. Based on these considerations, we calculated the proportionality factors for the π_1^* resonance for all TPn SAMs and presented them in Figure 5.12b (θ_1 was varied; θ_2 was 55°; the average values over different θ_1 were calculated). The odd-even variation of the molecular inclination is obvious, in agreement with the data in Figure 5.12a.

The changes in the molecular inclination should be accompanied by the corresponding variation of the packing density. Using a high quality sample of ODT SAM on GaAs(001) as reference,[33] we calculated the intensity ratios of the S 2p to the total As 3d photoemission signals and the effective thicknesses of the TPn SAMs. The derived values in Figures 5.12c and 5.12d, respectively, show a pronounced odd-even behavior corresponding to a higher packing density at an odd n and a lower packing density at an even n. This agrees with the observed changes in the molecular inclination: a smaller inclination corresponds to a higher packing density and vice versa, which is also supported by the comparison to the thickness values calculated on the basis of the tilt and the known molecular structure (Figure 5.12d). Note that the S 2p/As 3d intensity ratio is a direct measure of the packing density since the respective photoemission signals are similarly attenuated by the hydrocarbon overlayer.

In Figure 5.12d, the effective film thicknesses of TPn SAMs were calculated by evaluating the intensity ratios of the C 1s and As 3d emission, using a standard expression:

$$\frac{\frac{I_{C1s}}{I_{As3d}}(sample)}{\frac{I_{C1s}}{I_{As3d}}(refer)} = \frac{1-exp\frac{-d_{sample}}{\lambda_{C1s}(E_C)}}{exp\frac{-d_{sample}}{\lambda_{As3d}(E_{As})}} \times \frac{exp\frac{-d_{refer}}{\lambda_{As3d}(E_{As})}}{1-exp\frac{-d_{refer}}{\lambda_{C1s}(E_C)}} \qquad (5-4)$$

and ODT SAM as a reference system.[126] The photoelectron escape depth λ of Arsenic and Carbon depend on the X-ray source as well as the density of the layer material; for Mg Kα (1254 eV) they amount to λ_{As3d} = 28.15 Å at a photoelectron kinetic energy of E_{As} = 1208 eV and λ_{C1s} = 24.37 Å at a photoelectron kinetic energy of E_C = 964 eV.[70] The film thickness of

ODT SAM is set as 23.8 Å.[34] Note similar odd-even variation like Figure 5.12d is observed when using the C1s/Ga3d intensity ratios during the thickness calculation. (data not shown)

5.1.6 Odd-even effect for TPn SAMs on Au (111)

The phase of the observed odd-even behavior in section 5.1.5 is the same as that for TPn SAMs on Au(111):[21-23] higher molecular packing and smaller molecular orientation are observed in the TPn SAM with an odd n. In this section, I will confirm the odd-even behavior for TPn/Au SAMs by XPS and Ellipsometry results, and also make a comparison of this behavior for the TPn monolayer systems on Au (111) and GaAs (001) substrates.

The effective film thicknesses of TPn/Au SAMs were calculated in a similar way like TPn/GaAs system. The intensity ratios of C 1s and Au 4f emission signals were evaluated instead of the C1s/As3d intensity ratios, and DDT/Au SAM with total thickness of 15 Å was used as a reference.[127] Equation (5−4) should be modified to:

$$\frac{\frac{I_{C1s}}{I_{Au4f}}(sample)}{\frac{I_{C1s}}{I_{Au4f}}(refer)} = \frac{1-exp\frac{-d_{sample}}{\lambda_{C1s}(E_C)}}{exp\frac{-d_{sample}}{\lambda_{Au4f}(E_{Au})}} \times \frac{exp\frac{-d_{refer}}{\lambda_{Au4f}(E_{Au})}}{1-exp\frac{-d_{refer}}{\lambda_{C1s}(E_C)}} \qquad (5-5)$$

In equation (5−5), for Mg Kα (1254 eV), other parameters amount to λ_{Au4f} = 27.5 Å at a photoelectron kinetic energy of E_{Au} = 1165 eV and λ_{C1s} = 24.4 Å at a photoelectron kinetic energy of E_C = 964 eV. The derived film thicknesses of TPn/Au SAMs are shown in Figure 5.13a, from which the expected odd-even behavior can be clearly identified; this behavior is further confirmed by the Ellipsometry results in Figure 5.13b.

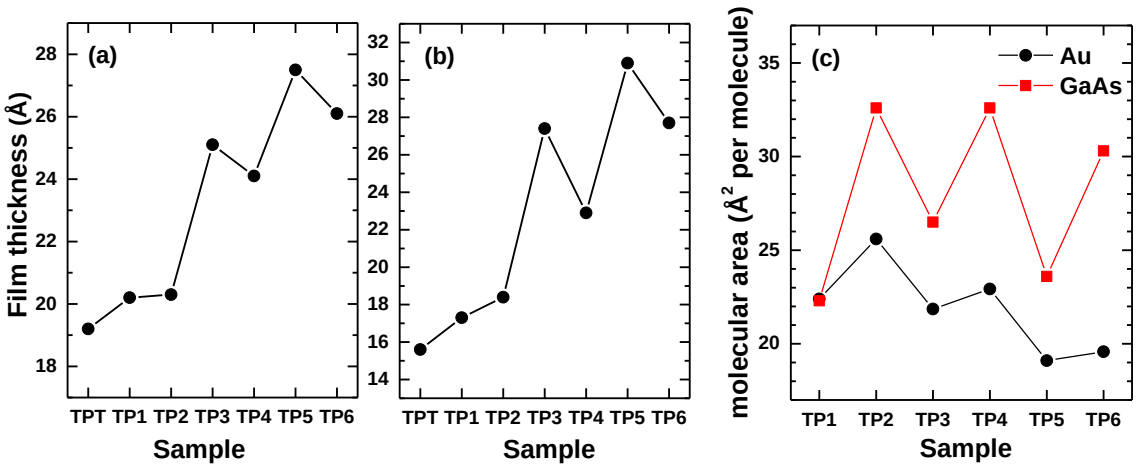

Figure 5.13a, b: Effective film thickness of TPn (n=0-6) SAMs on Au derived from the XPS (a) and ellipsometry (b) data; **Figure 5.13c:** packing densities of TPn (n=1-6) SAMs on GaAs (001) (red full squares) and Au (black full circles) derived from the XPS data.

In Figure 5.13a and b, the odd-even behavior seems not to be obvious from TP1 to TP2, revealed in particular from the Ellipsometry results (Figure 5.13b). This is understandable taking into account of previous studies of these monolayers on Au by STM and NEXAFS:[23,21] At room temperature, it is found TPn SAMs with odd n as well as TP2 SAM exhibit the same $2\sqrt{3}\times\sqrt{3}R30°$ structure, while TPn SAMs with even n (TP4 and TP6) have a different $c(5\sqrt{3}\times3)$ phase, corresponding to a lower packing density.[23] In accordance with the above results from STM, the NEXAFS-derived average tilt angle of the terphenyl moity in TP2/Au is noticeably smaller than the value expected for the odd-even behavior.[21]

In addition to the film thickness, the packing densities of TPn/Au SAMs were calculated from the intensity ratios of the S 2p and Au 4f emissions, following the approach of Refs [128] and [129]. The HDT SAM with well-known packing density of 21.62 $Å^2$/molecule[7,61] was used as a reference system. Similarly, the packing densities of TPn/GaAs SAMs were calculated using a high quality ODT/GaAs SAM as a reference, with its packing density set to 21.2 $Å^2$/molecule.[45] The derived values of the packing densities for TPn SAMs on Au and GaAs substrates are compared in Figure 5.13c. As clearly seen, obvious odd-even behavior with the same phase was observed for the TPn SAMs on these two substrates. In addition to this general behavior, the odd-even variation of the packing density, e.g. from n= 3 to 4, is more obvious for TPn SAMs on GaAs as compared Au, this may be probably related to the associated smaller domain size for SAMs on GaAs.[33,45] Note that it is not realistic to compare the absolute packing densities of the respective TPn monolayers on the two substrates due to the uncertainty in the packing density of the reference film on GaAs (ODT/GaAs).[45]

5.1.7 Discussion of TPn SAMs

High quality TPn (n=0 – 6) and TP1-CN SAMs have been prepared on GaAs (001) substrate after the procedure optimization (section 5.1.1). These TPn (and also TP1-CN) SAMs were found to be highly ordered and densely packed, and thus able to protect the surface from oxidation. More importantly, an obvious odd-even effect has been observed in these TPn SAMs: higher packing density and less SAM constituent inclination are observed in the TPn SAM with an odd (n) number of the methylene units in the alkyl linker.

5.1.7.1 Origin of the odd-even effect − bending potential

Taking into account the negligible difference in the molecular composition between the odd and even counterparts in the alkyl chain linker, the observed odd-even effect in the molecular inclination and packing density can only be caused by the favored binding

geometry of the GaAs−S−C bond, mediated by the bending potential, as shown in Figure 5.12e. This potential gives a predefined orientation to the alkyl linkage, which, as far as this linkage has *all trans* conformation or, at least, a sufficient rigidity, "transfers" this orientation to the terphenyl moiety. The bending potential enters the balance of the structure-building interactions either cooperatively or competitively.[130] If the geometry of GaAs−S−C bond and the number of the CH_2 groups fit to the energetically preferred, small inclination of the terphenyl moieties, high-density SAMs are formed in a cooperative way, as it happens for TPn SAMs with an odd *n*. By contrast, if the combination of this geometry and the number of the CH_2 groups corresponds to a large inclination of the terphenyl moieties, the bending potential works against the intermolecular forces in a competitive way, and as the result, a compromise structure with a lower-density packing will be achieved, as it happens for TPn SAMs with an even *n*. Without the bending potential, the molecular orientation and packing density will be mostly mediated by the interaction between the terphenyl moieties – a common building block of all TPn molecules – and no odd-even effect will be observed.

5.1.7.2 Non-universal Au-like bending potential

The phase of the odd-even effect on GaAs is the same as reported for Au (111) but is opposite to that for Ag (111) where smaller molecular inclination and, consequently, higher packing density are observed at an even number of CH_2 units in the alkyl linker of the TPn molecules.[21,23] The system is nevertheless somewhat more complicated. On Au(111) and Ag(111), the different bending potentials result in different tilt and twist angles of the alkyl chains (~30° and ~53° for Au(111)[16,17,20,21,23-25,131] and ~12° and 45° on Ag(111),[2,7,9] respectively). These values are adopted not only in NSAT-based SAMs but in the TPn series as well. For NSAT SAMs on GaAs(001) tilt and twist angles of 15-17° and ~43°, respectively, have been reported,[33,45] suggesting a behavior similar to the one on Ag(111).[132] The current findings nevertheless suggest that in the TPn series on GaAs(001), the alkyl chains rather adopt a conformation similar to the one on Au(111). So obviously, the effect of the Au-like bending potential, which plays a dominant role in the TPn SAMs on GaAs(001), is compensated to some extent by other factors in the case of NSAT SAMs. A special factor, which is relevant for GaAs but less important for Au and Ag substrates, is the ability of the GaAs substrate to compliantly strain over distances of the molecular correlation lengths.[33] This allows the molecular packing to achieve the types of structures which are only possible on a structurless substrate, but with much shorter range order.[33] Presumably, this factor is of major importance in the case of NSAT SAMs, whereas a different balance of the structure-

building interactions, with the stronger effect of the bending potential, occurs in other cases, such as TPn monolayers of the given study.

5.2 BPn SAMs

5.2.1 Spectroscopy characterization of BPn SAMs: HRXPS

The As 3d and Ga 3d HRXPS spectra of BPn (n=3, 5, 6) SAMs on GaAs (001) are shown in Figure 5.14. These spectra were acquired at a PE of 350 eV (compared with 580 eV) in order to achieve higher surface sensitivity. These spectra are dominated by the peaks related to the stoichiometric GaAs, accompanied by much weaker contributions from elementary As (gray doublets in As 3d spectra), surface states (gray doublets in Ga 3d spectra), and oxide-related components (shoulders at higher BE). Similar like the TPn/GaAs monolayer systems, a black doublet assigned to As−S species could be traced at ~42.4 eV ($As3d_{5/2}$) in the As 3d spectra, while the features for Ga-S species were obscured in the Ga 3d spectra; this suggests that the BPn molecules are also preferably bonded to the As atoms.

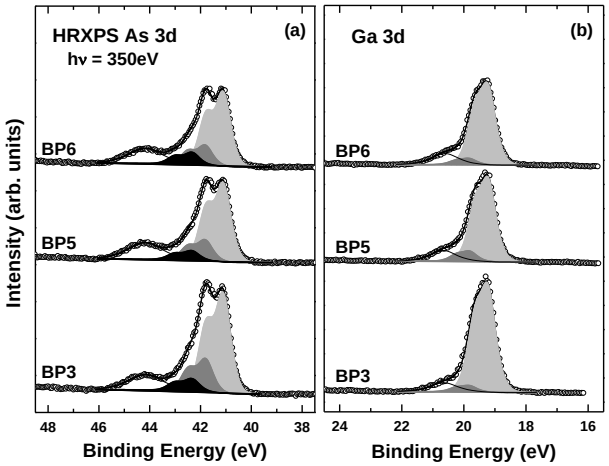

Figure 5.14: As 3d (a) and Ga 3d (b) HRXPS spectra of BPn (n = 3, 5, 6) SAMs on GaAs(001). The spectra were acquired at a photon energy of 350 eV. The spectra are decomposed in several doublets related to individual chemical species: (a) As 3d spectra: Light gray: stoichiometric GaAs; dark gray: elementary As; black: S-As. (b) Ga 3d spectra: Light gray: stoichiometric GaAs; dark gray: Ga oxide or surface Ga 3d component. The shoulders at the higher binding energy side of the shadowed doublets correspond to As (a) and Ga (b) oxides. The assignments were performed in accordance with refs 44, 55, 58, 59.

The spectra in Figure 5.14 can be basically representative of the entire data set for BPn SAMs (n=1 – 6), however, the oxide-related signatures, which are assumed mainly from post-oxidation,[59] appear more for the BPn SAMs with shorter alkyl linker such as BP1 and BP2 monolayers. The general weak oxidation feature for all BPn (n=1 − 6) SAMs suggests the dense molecular packing of these films,[44,55,58] simultaneously accompanied by the relatively lower film quality for BP1 and BP2 SAMs.

Formation of contamination-free and densely packed BPn SAMs were further supported by the S 2p and C 1s HRXPS spectra, as presented in Figure 5.15a and b, respectively. The S 2p spectra exhibit a single doublet at 162.4 ± 0.1 eV (S $2p_{3/2}$) assigned to the typical thiolate bonding, and no traces of unbound, disulfide, or oxidized species are observed in the spectra; the BE values agree well with the analogous ones observed previously for both aliphatic and aromatic SAMs on GaAs (001),[44,55,58] as well as those for TPn/GaAs SAM systems. The C1s spectra show one main emission peak at ~284.5 – 284.6 eV assigned to the biphenyl backbone, and another shoulder at higher binding energy (285.3 – 285.4eV) due to the shake up process,[18,76] while no trace of contamination could be detected. Note the BE values for the aromatic backbone are close to the reported values for non-substituted and biphenyl-substituted SAMs on GaAs,[55,58] and the shoulder at higher BE side has also been observed previously for different aromatic SAMs,[76] and biphenyl based SAMs in particular.[18]

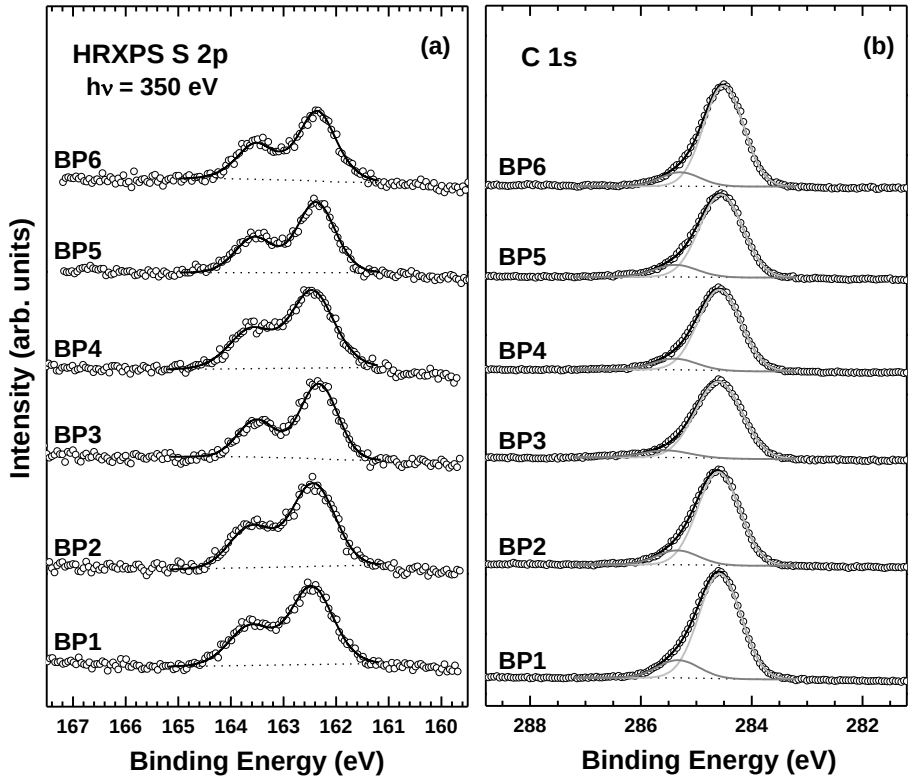

Figure 5.15: S 2p (a) and C 1s (b) HRXPS spectra of BPn (*n* = 1 - 6) SAMs on GaAs(001). The spectra were acquired at a photon energy of 350 eV.

The intensities of the S 2p emission of these BPn (n=1 – 6) SAMs are shown in Figure 5.16. When taking into account of the intensity of the S 2p emission, it mainly results from the interplay of two effects: On one hand, the packing density of the sulfur headgroups varies with n due to the either favorable or unfavorable packing conditions; on the other hand, the attenuation of the S 2p emission signal, governed by the effective film thickness, varies in the

opposite way, i.e., there is a larger attenuation for a densely packed film. In the present case, the odd-even variation in the headgroups' density is overcompensated by the change of the effective film thickness. This effect is especially obvious for the intensities of the S 2p emission excited with low PE (e.g. 350eV), and is also observed for the TPn,[22] and BPn[18] in particular, SAMs on metal substrates. Note that the zigzag variation of the intensities of the S 2p emissions, caused by the attenuation effect, can also be considered as one indirect proof of the odd-even behavior of the packing densities in these BPn SAMs.

The O 1s HRXPS spectra of BPn (n= 1, 2, 5, and 6) SAMs are shown in Figure 5.17. The spectra BP5, and BP6 SAMs exhibit nearly no signal, while those of BP1 and BP2 films exhibit some signal related to the oxidized GaAs components, which further confirms the relatively lower quality in the BPn SAMs with shorter alkyl linker, such as BP1 and BP2 monolayers.

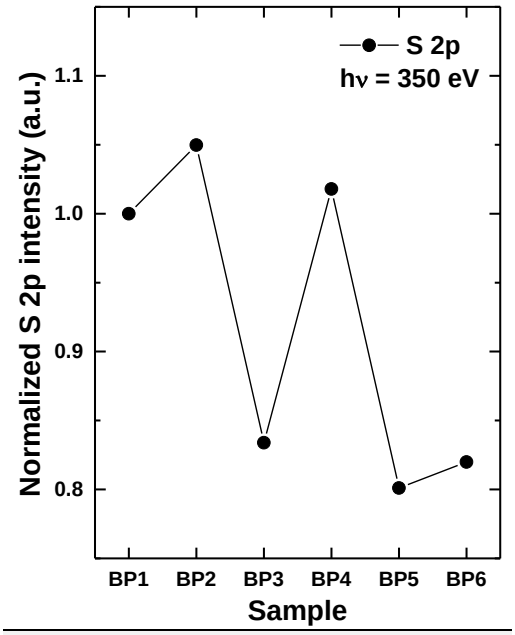

Figure 5.16: the intensities of the S 2p emission of BPn (n=1 - 6) SAMs on GaAs (001). The intensities for BPn SAMs were normalized to that for BP1 SAM.

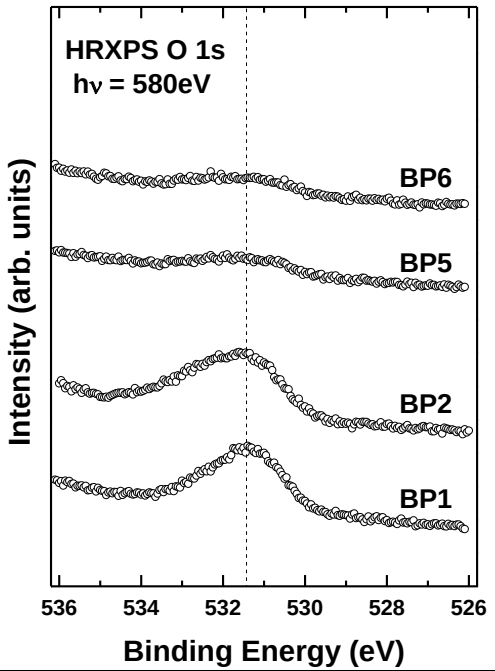

Figure 5.17: O 1s HRXPS spectra of BPn (*n* = 1, 2, 5, and 6) SAMs on GaAs(001). The spectra were acquired at a photon energy of 580 eV.

5.2.2 Spectroscopy characterization of BPn SAMs: NEXAFS spectroscopy

The HRXPS results were complemented by the NEXAFS spectroscopy data. The C *K*-edge NEXAFS spectra of BPn SAMs for the so-called magic angle geometry are presented in Figure 5.18a. These spectra are only characteristic of the electronic structure of the probed films, sampling the unoccupied molecular orbitals.[72] The spectra are typical of high quality aromatic SAMs;[16] they are dominated by the intense π_1^* resonance of the phenyl rings (at

~285.1 eV) and exhibit several characteristic σ^* resonances at higher photon energies. No features related to contamination could be traced. The R^* resonance associated with the alkyl linker of the BPn molecules cannot be clearly distinguished since it overlaps with the absorption edge (~287.6 eV).

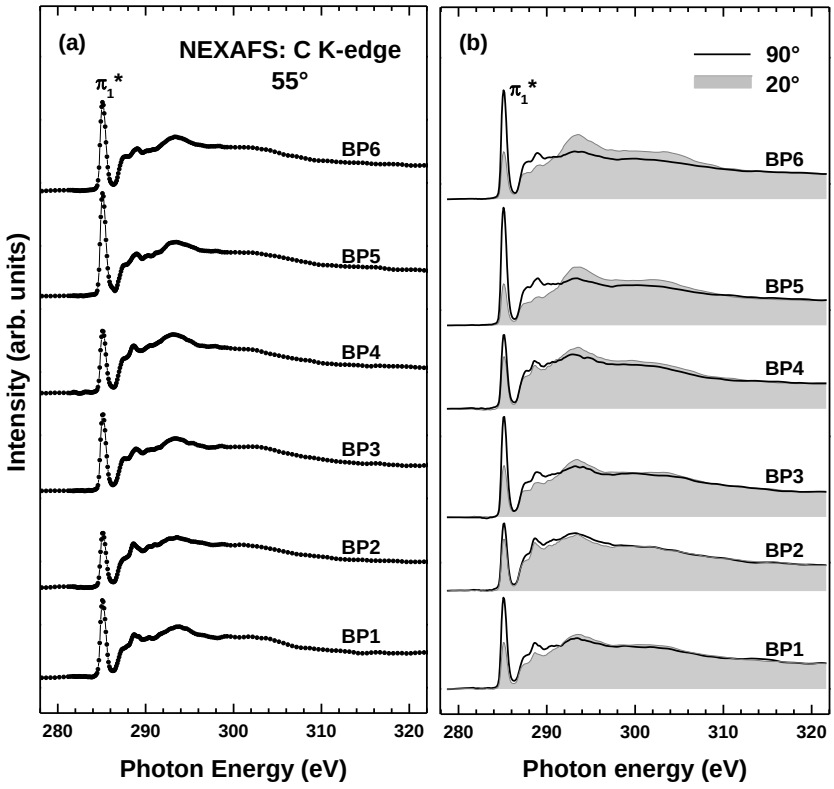

Figure 5.18: (a) C K-edge NEXAFS spectra of BPn (n = 1 – 6) SAMs on GaAs (001) acquired at an X-ray incident angle of 55° (a) as well as at normal (90°) and grazing (20°) incidence of X-rays (b). The characteristic π_1^* resonance is indicated.

Apart from the electronic structure, the molecular orientation in BPn SAMs can be monitored, relying on the linear dichroism of the NEXAFS spectra.[72] In Figure 5.18b, the C *K*-edge NEXAFS spectra of these films acquired at normal (90°) and grazing (20°) X-ray incidence are depicted; they exhibit pronounced linear dichroism of the π_1^* resonance. Considering the TDM of this resonance is perpendicular to the plane of the phenyl rings, its larger intensity at normal incidence suggests the upright orientation of the biphenyl moieties in these BPn SAMs. In addition, the larger intensity difference between the spectra acquired at 90° and 20° incidence angles observed for BPn with odd n implies the odd-even variation in the orientation of the biphenyl moieties. Similar odd-even behavior, generated by the bending potential, is also observed in TPn/GaAs monolayer systems.

5.2.3 Odd-even effect for BPn SAMs

The above qualitative considerations were complemented by the numerical analysis of the NEXAFS data using the same procedure described for TPn/GaAs monolayer systems in section 5.1.3. The twist angle of the biphenyl backbones was assumed to be 32°, note this twist (32°) is found for thioaromatic bulk materials. Besides, it is also based on theoretical estimates for the molecular arrangements in biphenyl and naphthalene mercaptan films on Au and on the experimental data for a series of oligo (phenylethynyl) benzenethiols.[21] The derived values of the average tilt angles of the biphenyl moieties in BPn SAMs are shown in Figure 5.19. These values exhibit a clear odd-even variation with varying length of the aliphatic linker: smaller molecular inclination is observed for odd *n*, while larger inclination occurs at even *n*.

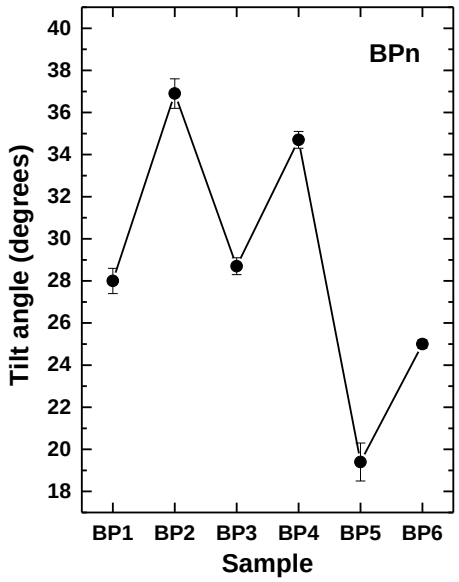

Figure 5.19: Average tilt angles of biphenyl moieties in BPn/GaAs (001) SAMs derived from the NEXAFS data, the aromatic backbone is assumed to twist at 32°. The error bars represent the accuracy of the theoretical fit and are not representative for the accuracy of the NEXAFS experiment which is usually believed to be ± 3-5°.

The observed odd-even change of the molecular orientation should be accompanied by the corresponding variation in the packing density. The effective film thicknesses of BPn/GaAs SAMs were calculated according to equation (5−4), using a high quality sample of ODT SAM with a thickness of 23.8 Å[34] as a reference system.[126] The spectra taken at a PE of 580 eV were used for the evaluation, the photoelectron escape depth λ of Arsenic and Carbon at this PE amount to λ_{As3d} = 16.7 Å at a photoelectron kinetic energy of E_{As} = 534 eV and λ_{C1s} = 11.3 Å at a photoelectron kinetic energy of E_C = 290 eV.[70] The derived thickness values are presented in Figure 5.20, they show an obvious odd-even variation, while thicker film, associated with the higher packing density, is obtained for the BPn SAM with an odd n. This agrees with the observed odd-even behavior of the molecular inclination, i.e. smaller inclination corresponds to the higher packing density, and vice versa.

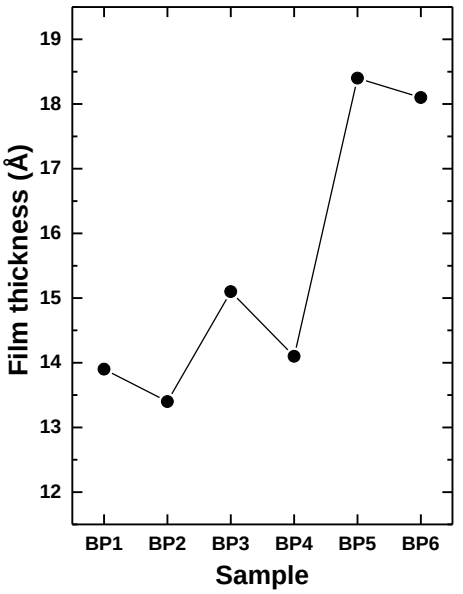

Figure 5.20: The HRXPS-derived effective thickness of BPn (n=1 - 6) SAMs on GaAs (001).

5.2.4 Discussion of BPn SAMs

5.2.4.1 Average tilt angles of the aromatic backbone in TPn and BPn SAMs

After comparing the values of the average tilt angles of the aromatic backbone in TPn and BPn SAMs (the same twist of 32° was used in both TPn and BPn SAMs), it is found the respective value is larger in the latter monolayer series (BPn), e.g. the value for BP3/GaAs SAM is larger than that for TP3/GaAs SAM, ~28.5° versus ~13.5°; this phenomena agrees with the general tendency observed previously for aromatic SAMs on metal substrates, viz. a decrease of molecular inclination with increasing the aromatic backbone.[133] Note, the average tilt angles calculated with a twist of 32° in TPn SAMs are not given in this thesis, however, they can be easily calculated from the values in Figure 5.12a

5.2.4.2 Bending potential for thiolate monolayers on GaAs

Like the TPn precursors, series of BPn (n=1 − 6) precursors also form contamination-free and densely packed SAMs on GaAs (001) substrate. The formed BPn SAMs protect the GaAs surface effectively from oxidation, while this protection weakens to some extent for the BPn SAMs with less number of CH_2 units such as BP1 and BP2 monolayers, which is attributed to their relatively poor film quality. An obvious, systematic odd-even effect has been observed for these BPn SAMs, i.e. smaller molecular inclination, and consequently higher packing density is obtained for BPn SAMs with an odd n; the phase of the odd-even variation is the same with that for TPn/GaAs monolayer systems. Thus, the existence of bending potential for the thiolate monolayers on GaAs, correlated with the favored binding geometry (~104° of the GaAs-S-C angle), is further proven by using series of BPn SAMs. In addition, this potential plays the predominant role in the balance of structural building forces in these films.

5.2.4.3 Relatively poor film quality of BP1 and BP2 SAMs

Unlike TPn SAMs, which all show high quality, the situation is more complex for the BPn monolayer systems: the BPn (n=1, 2) SAMs with shorter alkyl linker length exhibit relatively lower film quality. The reason for this is: except for the dominant effect of bending potential, another chain length factor also affects the structure of these BPn SAMs. The “chain length effect” for all SAM systems on GaAs has already been demonstrated in chapter 4 by studying the NSAT SAMs with different length. The molecular chain length is directly associated to the intermolecular packing force, which force the GaAs substrate atoms to reconstruct in the molecular correlation lengths.[33] This allows the molecular packing to achieve the types of structures which are only possible on a structureless substrate, but with much shorter range

order.[33] Compared with the terphenyl-based (TPn) SAMs, the loss of one phenyl group in the aromatic backbone leads to a significant decrease of the intermolecular packing force in biphenyl-based (BPn) SAMs. In this context, the chain length effect, which is reflected in the length of the alkyl linker, should be taken into account in the given BPn monolayer systems, in particular those with shorter alkyl linker such as BP1 and BP2 SAMs. The GaAs surface atom reconstruction can not be well resolved for these two monolayers, thus resulting in their relatively poor quality. By contrast, the reconstruction issue can be well resolved in the case of BP5 and BP6 SAMs as a result of the correlated longer alkyl chain, thus leading to the films with better quality, which can protect the GaAs surface more effectively from oxidation.

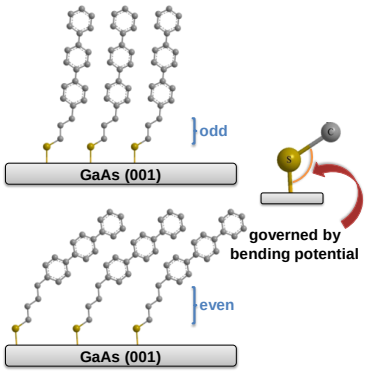

Summary of chapter 5

In summary, using series of TPn and BPn SAMs, we demonstrated the existence of a bending potential at the headgroup-substrate interface in the thiolate/GaAs(001) system with a preferable GaAs–S–C angle of ~104°, which is similar to the analogous value for the AT SAMs on Au. For both TPn and BPn SAM systems, this potential plays the dominant role in the balance of the structure-building interactions, mediating the odd-even variation in the molecular orientation and packing density. Therefore, bending potential should always be taken into account for the design of future, functional SAMs on technologically important type of semiconductor substrates such as GaAs (001).

As for BPn SAMs, in addition to the predominant effect of bending potential, another chain length factor, reflected in the alkyl linker length, also contributed to the structure-building factors, leading to the relatively poor quality of BPn SAMs with shorter alkyl chain, such as BP1 and BP2 monolayers.

Chapter 6: Structure of SAMs of Partially Fluorinated Alkanethiols with a Fluorocarbon Part of variable Length on Au (111)

As introduced in chapter 1, the most extensively studied und used SAMs are those of ATs on coinage metal substrates, Au (111) in particular.[1-6] One of the major advantages of these molecules is a relative ease of their substitution, which, as mentioned above, is important to redefine the properties of the SAM-modified surface in a desired way. A special kind of substitution is partial fluorination of the molecular backbone, resulting in PFAT, described by the general expression $CF_3(CF_2)_{n-1}(CH_2)_mSH$ and abbreviated as FnHmSH. Because of their hydrophobicity, rigidity, inertness, thermal stability, and potential use as nanoscale corrosion inhibitors, these films have gained substantial attention during the past years.[63,66,134-145] The respective studies were devoted to basic properties of these systems such as wettability,[138,140,143] thermal stability,[138,145] and radiation sensitivity,[146] as well as to understanding of their structure and organization.[63,65,135,137-139,145] The latter characteristics were found to be strongly affected by a larger van der Waals diameter of the fluorocarbon parts (~5.67 Å),[62,63] as compared to the hydrocarbon one (4.4 Å).[14] This diameter is associated with the typical helical conformation of the fluorocarbon chains (in contrast to *all trans* planar conformation of the hydrocarbon chains),[64] persisting usually in SAMs as well.[65,66] In accordance with this conformation, atomic force microscopy (AFM) and X-ray diffraction data reveal an enlarged (relative to non-substituted AT SAMs) intermolecular spacing of ~5.8 Å,[63,65,66,135,147] suggesting also that the packing density of the PFAT SAMs is determined by the bulky fluorocarbon part. Typical structures on Au(111) are commensurate p(2×2) and c(7×7) arrangements, but non-commensurate structures, with the parameters close to these arrangements, were reported as well.[63,65,135,147] The hydrocarbon chains, separated beyond their equilibrium spacing are, as far as they are not too short, however still capable to keep the *all trans* conformation typical of non-substituted AT SAMs.[16,139] Also, in spite of the large separation, their orientation was reported to mimick that of non-substituted AT SAMs, due to the effect of the bending potential.[16,139]

Until now, different combinations of fluorocarbon and hydrocarbon chains within the general FnHmSH architecture were studied with the goals to get systematic data for the PFAT monolayers and to monitor the effect of a particular combination on the structure and properties of these systems, assuming a close relationship between these basic characteristics.

As one of the available options, the length of the hydrocarbon chain was varied while keeping the length of the fluorocarbon chain constant (F10HmSH series).[16,63,138,139,141,145] The orientational and conformational order of both parts was found to change to some extent upon variation of *m*.[16,139] In particular, hydrocarbon segments become more ordered with increasing chain length.[138,141,145] Both the wettability and the thermal stability of the monolayers could be tailored by selection of *m*.[138] Alternatively, the length of the hydrocarbon part was kept constant but the length of the fluorocarbon part was varied (FnH11SH series).[141,145] It was found that the hydrocarbon parts remain ordered upon increasing the length of the fluorocarbon segment. Finally, the lengths of both fluorocarbon and hydrocarbon chains were varied simultaneously while keeping the total length ($n + m$) constant to look for the effect of the extent of fluorination (FnHmSH series).[137,140,141,145] This extent was observed to influence the wettability, structure, capacity, charge-transfer resistance, and resistance against exchange by a competing adsorbate.[140] In addition, the fluorocarbon parts of the SAM constituents were found to be oriented more upright on the substrate for higher *n* than for smaller ones.

Here in this chapter, we look more closely on the situation when the length of the hydrocarbon segment is kept constant while the length of the fluorocarbon segment is varied, putting special emphasis on the orientation and conformation of these moieties. Accordingly, we studied a series of the FnH11SH SAMs with n = 6, 8, and 10 (see Scheme 1.2) on Au (111) by a combination of several complementary spectroscopic techniques, which give a deep insight in the organization of these films. Consequently, we tried to understand this organization in terms of the structure-building interactions which are common for a variety of SAM-like systems; the obtained valuable findings could also be useful to better understand the analogous SAM systems on GaAs substrate in chapter 7. Note that the structure of the F10H11SH SAM has been studied in detail by a similar approach before,[139] so that the results for this monolayer can also be considered as a reference for the two other films in the study.

6.1 Results

6.1.1 HRXPS

S 2p HRXPS spectra of the FnH11SH SAMs are presented in Figure 6.1, along with the corresponding fits. Only a single S 2p doublet at a BE position of ~162.0 eV (S $2p_{3/2}$) is observed for all three monolayers with no traces of unbound, disulfide, or oxidized species. The above BE value corresponds to the thiolate species bonded to noble metal surfaces,[7,76,101,102] which suggest that all molecules in the FnH11SH films are bound to the substrate via thiolate-gold bond, as can be found in similar systems. The fwhm of the S $2p_{3/2}$

and S $2p_{1/2}$ peaks (~0.54 eV) is essentially the same as that for non-substituted AT SAMs on gold (0.55-0.6 eV).[76] Since the fwhm value is a fingerprint of the homogeneity of the adsorption sites for the sulfur head groups, the above results imply a rather high degree of homogeneity at the SAM-substrate interface. The intensity of the S 2p doublet decreases with increasing *n*, which agrees well with the expected attenuation of the respective photoelectron signal for the intact PFAT molecules bonded to the substrate via conventional thiolate bond – the longer molecule is then associated with stronger signal attenuation.

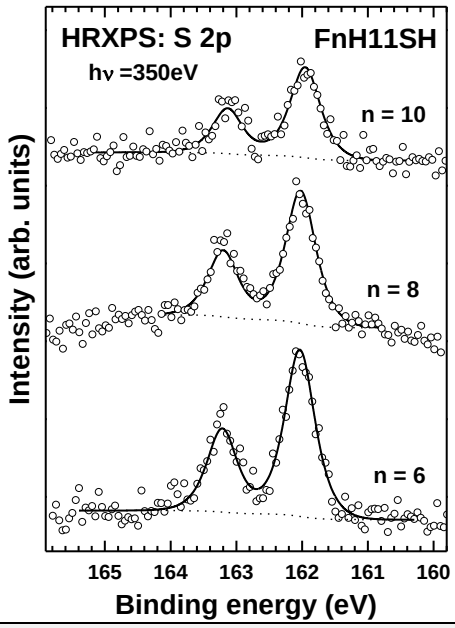

Figure 6.1: S 2p HRXPS spectra of the FnH11SH SAMs on Au acquired at a photon energy of 350 eV (open circles). The spectra are fitted by a single doublet with a branching ratio of 2:1 (solid line). The background is shown by a dotted line.

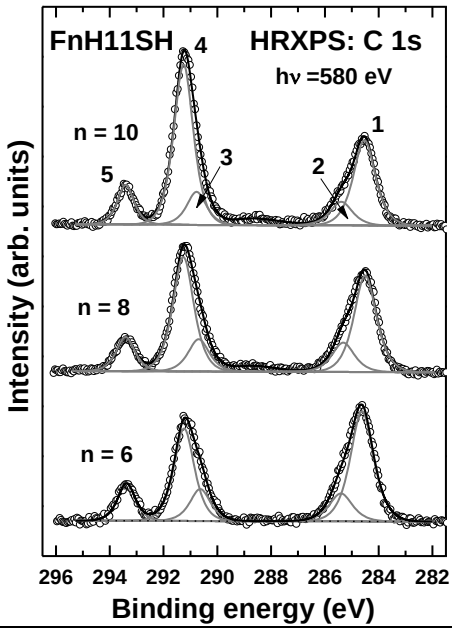

Figure 6.2: C 1s HRXPS spectra of the FnH11SH SAMs on Au acquired at a photon energy of 580 eV (open circles). The spectra are decomposed into individual emissions (gray solid lines) within a fitting procedure; these emissions are marked by numbers. The resulting fitting curve is shown by a thick solid line.

Adsorption of the intact FnH11SH molecules onto the substrate surface and formation of well-defined SAMs are also confirmed by the C 1s HRXPS spectra in Figure 6.2. These spectra exhibit three distinguished peaks of different intensities, which, going from the low to high BE, can be clearly assigned to the hydrocarbon chain part, the $–CF_2–$ chain part, and the CF_3 terminal moiety (peak 5), respectively.[139] The first two peaks are somewhat asymmetric and can therefore be decomposed into individual signals, viz. emissions 1 and 2 for the hydrocarbon part and emissions 3 and 4 for the $–CF_2–$ chain part.[82] Emission 2 corresponds to the terminal moiety connected to the fluorocarbon chain, resulting in an increase of the respective BE position as compared to all other $–CH_2–$ units (peak 1). Similarly, the emission 3 corresponds to the terminal $–CF_2–$ moiety connected to the hydrocarbon chain, resulting in decrease of the respective BE position as compared to all other $–CF_2–$ units (peak 4).

The intensities of the individual emissions show the expected behavior with varying *n*. The intensities of the peak 5 (CF_3 terminal moiety) do not differ noticeably for all three films. Considering that the constituents of all these SAMs have only one CF_3 tail group which, according to the standard architecture, is located at the SAM-ambience interface, the respective photoemission signal should only depend on the molecular density. The latter parameter seems then to be similar for all FnH11SH monolayers, with, probably, a slightly higher value in the n = 10 case. The intensity of the peaks 3 and 4 (fluorocarbon part) increases with the increasing length of the fluorocarbon chain as can be expected. By contrast, the intensity of the peaks 1 and 2 (hydrocarbon part) have an opposite behavior even though the length of the hydrocarbon chain is the same for all SAMs of this study. The reason for this intensity decrease is the stronger attenuation of the respective photoemission signal by the longer fluorocarbon chain. Based on these considerations, one can consider the intensity decrease as an additional evidence for the expected, upright orientation of the SAM constituents, anchored to the substrate by the thiolate group (see Figure 6.1).

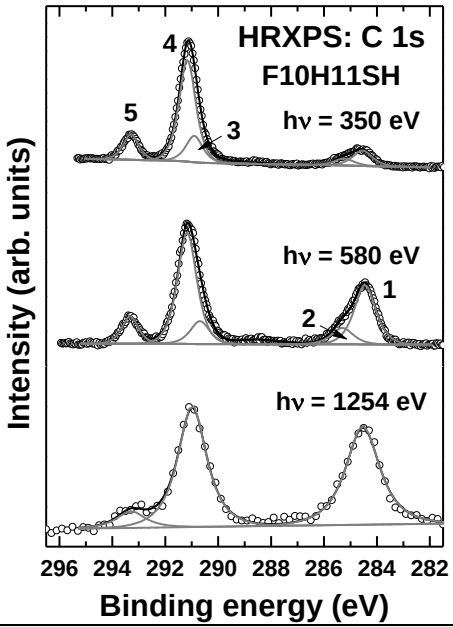

Figure 6.3: C 1s HRXPS and XPS spectra of the F10H11SH SAM on Au acquired at photon energies of 350 eV, 580 eV, and 1254.6 eV (XPS) (open circles). The spectra are decomposed into individual emissions (gray solid lines) within a fitting procedure; these emissions are marked by numbers. The resulting fitting curve is shown by a thick solid line.

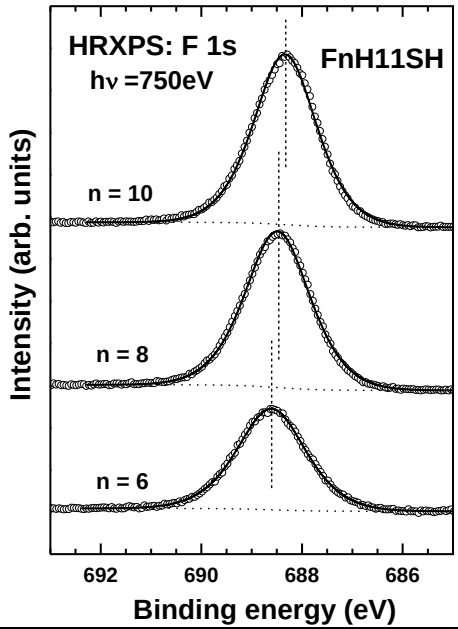

Figure 6.4: F 1s HRXPS spectra of the FnH11SH SAMs on Au acquired at a photon energy of 750 eV (open circles). The spectra are fitted by a single emission (solid line). The background is shown by a dotted line. The vertical dashed lines highlight the BE positions of the emission.

To further support this statement, C 1s HRXPS spectra of F10H11SH taken at different photon energies and normalized to the same height of peak 4 ($-CF_2-$ part) are compared in Figure 6.3. It is clearly seen that the intensity of the $-CH_2-$ component increases with increasing kinetic energy of the photoelectrons, following the increasing mean free path

governing the attenuation efficiency. Note that because of the lower resolution, peaks 2 and 3 are not perceptible in the spectra taken at 1254 eV.

In contrast to the C 1s spectra, F 1s HRXPS spectra of the FnH11SH monolayers in Figure 6.4 exhibit only one emission peak related to the entire fluorocarbon chain, since it is well known that CF_2 and CF_3 species can not be distinguished in this spectral region.[63,82,139] As expected, the intensity of the emission increases with increasing fluorocarbon chain length. At the same time, the BE position of this emission moves downwards with increasing length of the fluorocarbon segment, while the opposite behavior, related to the decreasing extent of screening of the photoemission hole by the substrate electrons could be expected based on the analogous data for SAMs on metal substrates.[76,103] This effect can be explained by the vacuum-level-like pinning of the energetic levels in SAMs.[148-151] According to this pinning model, BE positions of the C 1s and F 1s emissions become dependent on the work function of the system. In this context, the persistent downward shift of the F 1s emission at going from F6H11SH to F10H11SH, can be associated with progressive increase of the work function.[150,151] In its turn, this increase can be associated with either increasing packing density of the FnH10SH species or less inclination of the fluorinated chain, since both, the density and the orientation of the CF_3 terminal moieties, determine the work function of the PFAT/Au systems (the adsorption of the PFAT molecules results generally in an increased work function, with the prevailing contribution coming from the CF_3 moieties).[152] A combined effect of these two factors is also possible.

6.1.2 XPS: Film thickness and packing density

In addition to the spectra analysis, the film thickness values were calculated by evaluating the intensity ratios of the C 1s and Au 4f emissions according to equation (5–5) in chapter 5,[126,153] and using a DDT SAM – a film of well-defined thickness – as a reference system. For the thickness of the DDT SAM, a value of 15 Å was used;[127] this value agrees well with the theoretical estimate of the SAM thickness, on the basis of the alkyl chain length (1.26 Å per CH_2 moiety),[154] molecular inclination (30-33.5°),[2,4] and Au−S distance (1.8 A).[8,155] The derived values of the effective thickness were 20.1, 22.9, and 24.2 Å for the F6H11SH, F8H11SH, and F10H11SH monolayers, respectively. Further, the packing densities were coarsely calculated from the intensity ratios of the S 2p and Au 4f emissions, following the approach of Refs [128] and [129]. As a reference system with well known packing density (21.62 $Å^2$/molecule),[7,61] a HDT SAM on Au(111) was used. The derived areas per molecule were 28.4, 28.1, and 27.7 $Å^2$ for the F6H11SH, F8H11SH, and F10H11SH SAMs,

respectively. All these values are quite close to the expected value for the helical conformation of the fluorocarbon chain and can be associated with an intermolecular spacing of 5.7-5.8 Å, close to the van der Waals diameter of this chain (5.67 Å) and to the lattice constant observed in previous AFM studies on analogous systems (5.7-5.9 Å).[63,65,135,147] This suggests that the packing density of the FnH11SH monolayers is primarily governed by the bulky helical conformation of the fluorocarbon part and does not change significantly with the varying length of the fluorocarbon part. There is just a general tendency that the efficient packing density decreases slightly with decreasing *n*. Note that the attenuation length for photoelectrons in fluorocarbon films are almost indistinguishable from those in hydrocarbon films,[142] which justifies the use of the DDT and HDT SAMs as references for the evaluation of the XPS data in terms of the effective film thickness and packing density.

6.1.3 IRRAS

Part I: General description

The IRRAS spectra of the FnH11SH monolayers are depicted in Figures 6.5 and 6.6 for the spectral regions predominantly characteristic of the CF_2 and CH_2 related vibrations, respectively. Figure 6.5 presents additionally the spectrum of neat F10H11SH and the DFT calculated spectrum of the isolated F10H11SH molecule. The analogous spectra for the F6H11SH and F8H11SH cases are presented in the Appendix (Figure S1 and S2). The assignments of the main vibrational modes are provided in Table 6.1; these assignments and the estimation of the orientation of the respective TDMs were conducted with the help of DFT calculations of the isolated PFAT molecules (see more in section 3.5.4.2). Comparison of the experimental spectra with the calculations reveals a fair accordance. Also, the calculation results are in accordance with literature,[65,134,139,147] regarding both the assignment of the relevant absorption bands modes and the orientation of their TDMs (*vide infra*).

Part II: Fluorocarbon region

The spectral region between 1100 and 1400 cm^{-1} (Figure 6.5) contains characteristic stretching and bending modes of the CF_2 groups. In particular, the intense absorption bands in the 1150-1250 cm^{-1} region (among them bands 1 and 2) are characteristic of fluorocarbon entities (see Table 6.1 for details). They have a noticeable contribution from the asymmetric

CF_2 stretching vibration with a TDM perpendicular to the helical axis.[134] These modes are observed both for poly(tetrafluoroethylene) (PTFE) and for thin organic films containing fluorocarbon segments.[2,66,134,139] The positions of these modes do not change significantly with the varying length of these segments and only intensity redistribution occurs.[2,147,156]

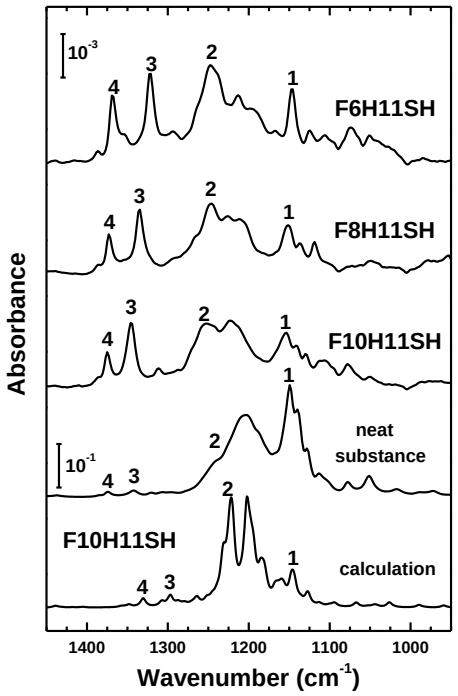

Figure 6.5: IR spectra of the FnH11SH SAMs on Au in the range characteristic of the CF_2 vibrations (three upper curves), along with the spectrum of the neat F10H11SH substance (second curve from bottom), recorded with an ATR unit, and the theoretical spectrum of an isolated molecule, calculated using DFT. Two scale bars indicate the absorbance intensities of the experimental spectra for the SAMs and neat substance, respectively. The most prominent bands are marked with numbers. See text and Table 6.1 for details.

In contrast to these modes, the absorption bands 3 and 4 at 1322-1344 and 1368-1375cm^{-1}, respectively, are identified as axial CF_2 stretching vibrations with a strong component of the dynamic dipole moment along the helical axis.[134] These modes are also characteristic of the helical conformation of the fluorocarbon chain and are commonly observed in thin organic films containing these entities.[65,66,134,139,147] The appearance of these modes as well as bands 1 and 2 for all investigated FnH11SH films implies that the fluorocarbon parts of the FnH11SH molecules in the densely packed layers on the Au substrate adopt a helical conformation. Significantly and in contrast to the absorption bands in the 1150-1250 cm^{-1} region, bands 3 and 4 are only observed for short fluorocarbon chain oligomers.[156] The reason for their appearance is the finiteness of the fluorocarbon helix which causes certain modes to become active.[157] The solution of the eigenvalue equation for such systems depends on the length of the oligomer.[158] Accordingly, the positions of these bands shift continuously to higher wavelengths with increasing length of the fluorocarbon chain,[66,141] which, as suggested by Colorado et al.,[141] can even be used to determine the length of the fluorocarbon segment in PFAT SAMs regardless to the orientation of the segments within the film.

In full agreement with the above literature data, the positions of bands 3 and 4 in the spectra of FnH11SH SAMs in Figure 6.5 move progressively to higher wavenumbers with increasing length of the fluorocarbon segment; the respective chain length dependence[66,141] is also apparent in the calculated spectra (see Table S1-S3 in the Appendix).

Along with the positions of the absorption bands, their relative intensity is of importance as well. As can be deduced from comparison of the spectra of the FnH11SH SAMs with the ones of the respective neat substances (Figure 6.5 and Figure S1 and S2 in the Appendix), the perpendicular CF_2 bands are strongly attenuated in the SAM spectra which can only be explained by a rather upright orientation of the fluorocarbon segments. For such an orientation, the bands with TDMs perpendicular to the fluorocarbon segments will be strongly suppressed on account of the surface selection rule on metals,[159] and this is exactly what is observed in Figure 6.5. Exploiting further the selection rule, one can consider the relative intensity of the bands with TDMs along the segment axis and the bands with TDMs perpendicular to this axis as a fingerprint parameter for the degree of the molecular inclination. This relative intensity seems to increase slightly with increasing length of the fluorocarbon segment, suggesting that the inclination is somewhat smaller in the F10H11SH films as compared to the F8H11SH and F6H11SH SAMs.

Table 6.1: Infrared Vibrational Modes of FnH11SH SAMs, along with the respective assignments[a]

	mode assignment	F6H11SH	F8H11SH	F10H11SH	TDM[b]
1	ν as CF_2, ω CH_2	1146 s	1151 m	1154 m	almost perpendicular to helical axis
2	ν as CF_3, ν as CF_2, τ CH_2	1247 s	1246 s	1252 s	almost perpendicular to helical axis
3	ν sym CF_2, ν sym CF_3	1322 s	1335 s	1345 s	almost parallel to helical axis
4	ν sym CF_2, ν CC helix	1368 s	1373 m	1375 m	almost parallel to helical axis
5	ν sym CH_2	2850 m	2851 m	2851 m	parallel to CCC backbone plane
6	ν as CH_2	2919 m	2920 m	2920 m	perpendicular to CCC backbone plane

[a]Wavenumbers are given in cm^{-1}. Mode 1-6 positions in the neat substance spectra and the calculated spectra of F6H11SH, F8H11SH and F10H11SH are listed in Tables S1-S3 in the Appendix. Abbreviations used: ν-stretch, τ-torsion, ω-wagging; as-asymmetric, sym-symmetric, vs-very strong, s-strong, m-medium, w-weak.

[b]Information on the direction of the vibrational mode's transition dipole moment.

Part III: Hydrocarbon region

The hydrocarbon part of the FnH11SH SAMs was probed by IRRAS as well, relying on the C–H stretching modes of the CH_2 units (Figure 6.6). The spectra of all these monolayers exhibit distinct symmetric and asymmetric C–H stretching modes (5 and 6; see Table 6.1) at about 2850 and 2919 cm^{-1}, respectively, in accordance with the literature data for the analogous systems.[141] These band positions are characteristic of the planar zigzag conformation of hydrocarbon chains with a low percentage of *gauche* defects,[10,109] which is observed for both ordered polyethylene and well-ordered aliphatic SAMs.[7,81] Note the blue shift of the band positions of modes 5 and 6 in the neat substance spectra (see Table S1-S3 in the Appendix) indicates a higher amount of gauche defects in the bulk as compared to the SAMs. Interestingly, according to the IR spectra (Appendix), the degree of order in the F10H11SH bulk seems to be slightly higher than in the other two substances, probably a consequence of the longer fluorocarbon segment.

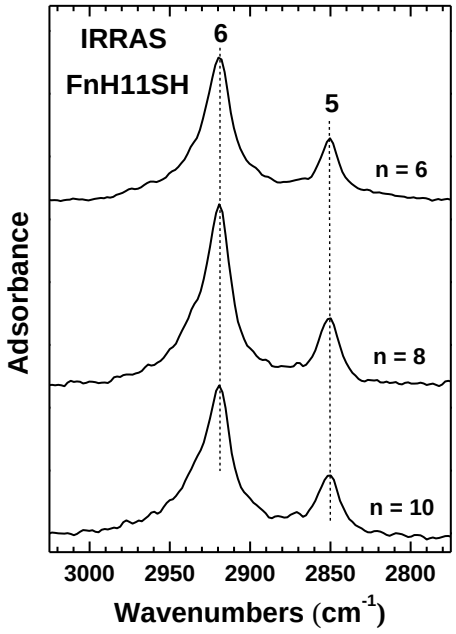

Figure 6.6: IR spectra of the FnH11SH SAMs on Au acquired in the C-H stretching region. The characteristic absorption bands are marked with numbers, see text and Table 6.1 for details. The vertical dashed lines highlight the positions of these bands.

Along with the above conclusions regarding the conformation of the hydrocarbon segments, information about their orientation can be derived from the IR spectra in Figure 6.6 by taking into account that the TDMs of the C–H stretching modes are perpendicular to the molecular axis and to each other, and the electric field vector of the IR light in the grazing incidence geometry is oriented normal to the substrate. Under these conditions, the observed similar integral intensities of these modes for the FnH11SH monolayers of this study lead to the tentative conclusion that the hydrocarbon segments in all these SAMs have similar orientation. In addition, the twist angle of these segments can be estimated. This parameter determines the rotation of the plane containing the *all trans* carbon backbone with respect to the plane defined by the chain axis and the surface normal. The twist angle was calculated from the intensity ratio of the asymmetric and symmetric modes following the RATIO method by Debe.[111] The resulting values of the twist angles are close to ~53° for all the three FnH11SH SAMs. Note that this value practically coincides with the corresponding value of 53° found for the non-substituted AT SAMs on gold.[7]

6.1.4 NEXAFS spectroscopy

Carbon *K*-edge NEXAFS spectra of the FnH11SH monolayers acquired at an X-ray incidence angle of 55° are presented in Figure 6.7; spectra acquired at this "magic" angle are free of orientational effects[72] and, in this sense, are only representative of the electronic structure of the target systems. The spectra in Figure 6.7 contain two absorption edges at ~287.8 and ~294.0 eV related to the C 1s → continuum excitations for the carbon atoms bonded to hydrogen and fluorine, respectively; the first edge is perceptible, the second is hidden due to the overlap with other features. The spectra are dominated by the pronounced resonances of the fluorocarbon part, viz. those related to the transitions from the C 1s state to the C–F σ^*, C–C σ^*, and C–F´ σ^* orbitals at ~292.5, ~295.5, and ~298.8 eV, respectively.[82,160-162,134,139] The corresponding TDMs are oriented almost perpendicular (C 1s → C–F σ^*) or along (C 1s → C–C σ^*) the axis of the fluorocarbon chain, respectively.[108,160,161,134] As to the hydrocarbon part, only a weak feature at ~288.0 eV, alternatively assigned to the C 1s excitations into predominantly Rydberg states,[105,106] valence C–H orbitals,[72] or mixed valence/Rydberg states,[104] is discernible in the spectra, with the corresponding TDMs oriented perpendicular to the alkyl chain axis.[81,107,108] The further characteristic C–C σ^* and C–C´ σ^* resonances of the hydrocarbon parts at ~293.0 and ~302.0 eV, respectively,[81,107,108] overlap with the strong features related to the fluorocarbon segments and are, therefore, indistinguishable in the spectra.

Both the positions of the resonances related to the fluorocarbon segments and the entire spectral shape are very similar to the calculated NEXAFS spectra of PTFE in the standard[163,164] 13/6 (or 15/7) helical conformation of the fluorocarbon chains.[165] This behavior suggests that the fluorocarbon segments in all FnH11SH SAMs adopt the expected helical conformation, in full agreement with the conclusions made on the basis of the HRXPS and IR data. Distortions of the helical conformations in terms of the extent of coiling, stretching or elongation, relative orientation of the fluorine atoms, and location of the carbon atoms with respect to the chain axis are assumed to result in the modification of the NEXAFS spectra, with the extent and character depending on the kind and degree of distortion.[165] At a large distortion, complete change of the spectral envelope can occur, while, at moderate distortion, shift and/or broadening of the absorption resonances can be expected.[165] In our case, the general spectral envelopes are similar for all studied FnH11SH SAMs, suggesting that the decrease in the length of the fluorocarbon segment does not result in noticeable disturbance of the helix structure. At the same time, the positions of the characteristic absorption resonances of the fluorocarbon segment change slightly and the peaks become slightly broader with

decreasing *n* (in a systematic fashion), hinting on some minor distortions of the helical conformation in the F8H11SH and F6H11SH SAMs.

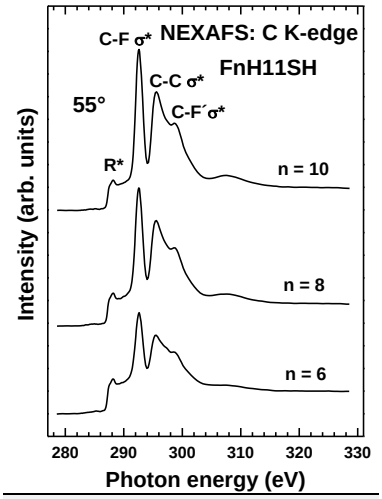

Figure 6.7: C K-edge NEXAFS spectra of the FnH11SH SAMs on Au acquired at an X-ray incident angle of 55°. The characteristic absorption resonances are marked.

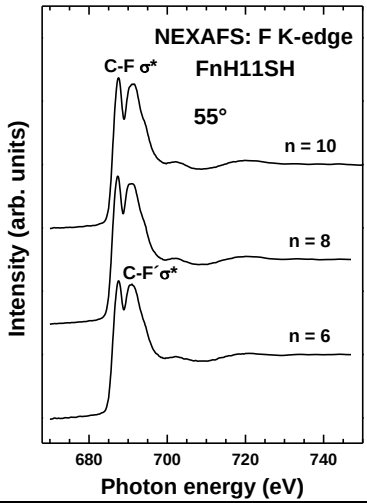

Figure 6.8: F K-edge NEXAFS spectra of the FnH11SH SAMs on Au acquired at an X-ray incident angle of 55°. The characteristic absorption resonances are marked.

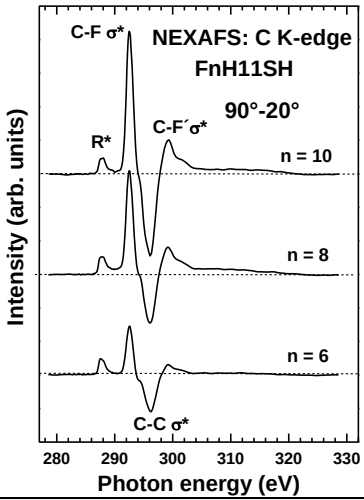

Figure 6.9: Difference between the C K-edge NEXAFS spectra of the FnH11SH SAMs on Au acquired at the normal (90°) and grazing (20°) incidence of X-rays. The difference peaks corresponding to the characteristic absorption resonances are marked. The horizontal dashed lines correspond to zero.

Fluorine *K*-edge NEXAFS spectra of the FnH11SH monolayers acquired at an X-ray incidence angle of 55° are presented in Figure 6.8. All these spectra are very similar to those of PTFE[166] and are dominated by the pronounced resonances at ~687.4 and ~691.0 eV assigned to the transitions from the F1s core level to the C–F σ^* and C–F´ σ^* orbitals. The similarity to PTFE which has the "standard" helical conformation is an additional evidence for the same conformation of the fluorocarbon segments in the FnH11SH SAMs.

As introduced of the NEXAFS spectroscopy in chapter 2, the information about the orientational order and molecular orientation in the PFAT SAMs can be obtained from the linear dichroism of the NEXAFS spectra, i.e., their dependence on the incidence angle of the X-rays.[72] A convenient way to monitor the linear dichroism is to calculate the difference between the spectra acquired at normal (90°) and grazing (20°) incidence of X-rays. Such C *K*-edge difference spectra are presented in Figure 6.9. They exhibit pronounced peaks at the position of the absorption resonances, which highlights the strong dependence of the resonance intensity on the angle of X-ray incidence, characteristic of well-ordered, densely packed monomolecular films. The resonances with TDMs oriented along and perpendicular to the axis of the fluorocarbon and hydrocarbon segments show, as expected, opposite behaviors with the varying incidence angle of X-rays. The positive peak at the position of the R^* and C–

F σ^* resonances and negative peaks at the position of C–C σ^* resonances in the difference spectra suggest a predominantly perpendicular orientation of both fluorocarbon and hydrocarbon segments in the FnH11SH SAMs. Besides, the intensities of the R^* resonance for all three of these SAMs are nearly the same. Consequently, considering that they have the same length of the hydrocarbon segments, we can conclude that the latter moieties have similar orientation in all FnH11SH SAMs, which also agrees with the IRRAS results.

The above qualitative considerations were complemented by the quantitative analysis of the NEXAFS data within the standard theoretical framework.[72] To this end, the average tilt angles of the fluorocarbon and hydrocarbon segments were derived from the angular dependence of the C–F σ^* and R^* resonance intensities using equation (4–1) typical for a plane-type orbital:[72]

$$I(\gamma,\theta) = A\left\{P\times\tfrac{2}{3}\left[1-\tfrac{1}{4}\cdot(3\cdot\cos^2\theta-1)\cdot(3\cdot\cos^2\gamma-1)\right]+(1-P)\times\tfrac{1}{2}\cdot(1+\cos^2\gamma)\right\} \qquad (4\text{–}1)$$

where A is a constant, P is a polarization factor of the X-rays, and γ is the angle between the sample normal and the normal of the molecular orbital plane. Note that both C–F σ^* and R^* orbitals were considered as plane ones, which is justified since the R^* orbital is comprised of two mutually perpendicular orbitals with almost identical intensities,[104] and the C–F σ^* orbital can be related to the CF_2 plane in the same manner as the R^* orbital.

The C–F σ^* resonance was chosen because of its high intensity and its separation from the other resonances, while the R^* resonance was selected as the single distinguishable resonance related to the hydrocarbon segment in the present case. To extract the intensities of the C-F σ^* and R^* resonances from the experimental spectra, the entire spectra series were self-consistently fitted by several Gauss peaks representing the observed resonances and by two absorption edges (the standard shape)[72] related to the C 1s → continuum excitations for the hydrogen- and fluorine-bonded carbon atoms (the standard shapes of the absorption edges were used)[72]. The positions and widths of the fitting peaks were determined from the difference spectra (90°–20°) following the procedure described by Outka et al.[107] and Hähner et al.[11] The positions of the absorption edges were obtained from consideration of the C 1s XPS spectra and literature data.[82,146] As an example, the fitting of the C *K*-edge NEXAFS spectra of F10H11SH/Au acquired at 55° X-ray incidence angle is shown in Figure 6.10. In the evaluation process, to avoid normalization problems, not the absolute intensities but the intensity ratios I(θ)/I(90°) were analyzed,[72] where I(θ) and I(90°) are the intensities of a

particular absorption resonance at X-ray incidence angles of θ and 90°, respectively. The results of this analysis are presented in Figure 6.11.

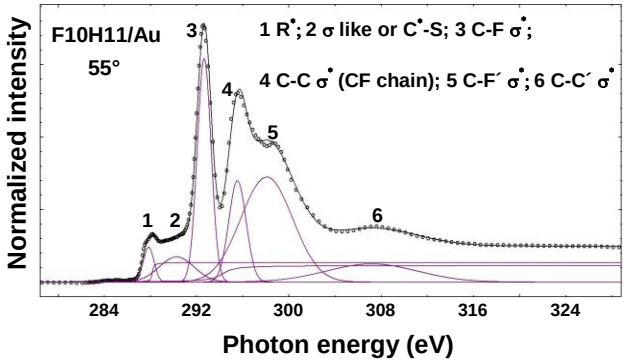

Figure 6.10: A fit of the C K-edge NEXAFS spectra of F10H11SH SAM on Au. The spectra acquired at an X-ray incidence of 55° is taken as an example. The characteristic resonances are marked with numbers, and their assignment is given; the two edges can be observed at ~287.8eV and ~294eV. (see text for detail)

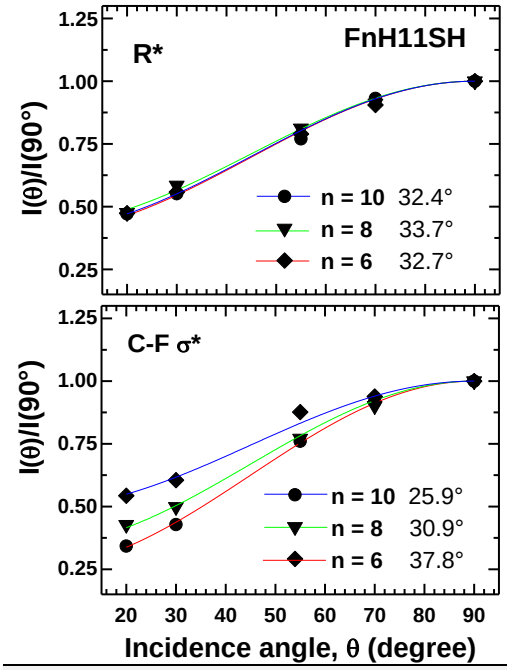

Figure 6.11: The angular dependence of the I(θ)/I(90°) intensity ratios for the R* (top panel) and C–F σ* (bottom panel) resonances for the F10H11SH (circles), F8H11SH (triangles) and F6H11SH (diamonds) SAMs on Au, along with the best theoretical fits (solid lines). In the case of the R* resonance, the fitting curves for the different SAMs almost coincide practically and are therefore hardly distinguishable. The derived values of the average tilt angles for the hydrocarbon and fluorocarbon segments of the FnH11SH chains are given. The values for the fluorocarbon segments were further corrected (see text for details).

The fits of the measured angular dependencies for the R* resonance intensity by the theoretical expression give average tilt angles of ~33°,~34°, and ~32° for the hydrocarbon segments in the F6H11SH, F8H11SH, and F10H11SH SAMs, respectively, suggesting that this parameter does not depend on the length of the fluorocarbon segment. Significantly, the derived values are very close to the analogous value for the non-substituted AT SAMs on Au(111).[6,7,10-13] The accuracy of these values is ±3°. The major source of errors is the relatively (as compared to σ* C–F and σ* C–C) low intensity of the R* resonance and the uncertainty of the exact location of the C1s (C–H) absorption edge, these characters can also be identified in the fitting spectra of F10H11SH SAM (example) shown in Figure 6.10.

The fits of the measured angular dependencies for the C–F σ* resonance intensity by the theoretical expression give average tilt angles of ~38°, ~31°, and ~26° for the fluorocarbon segments in the F6H11SH, F8H11SH, and F10H11SH SAMs, respectively. It should be

noted, however, that these values were obtained assuming that the molecular plane of the CF_2 entities is exactly perpendicular to the fluorocarbon chain axis.[134] In reality, these planes are slightly tilted toward the helix axis with a tilt angle depending on the helix parameters. Assuming a standard 15/7 helix with a twist of about 13-15° per C–C bond for the fluorocarbon segments in the FnH11SH SAMs,[65,167-169] one obtains a tilt angle of 8-9° between the normal of the CF_2 planes and the chain axis. Presumably, exactly this angle will be derived from NEXAFS spectra of vertically standing fluorocarbon chains. The real tilt angle of these moieties (0°) can then be tentatively obtained by a subtraction of the tilt angle of the CF_2 planes from the measured value. Applying the same subtraction procedure in the present case we obtained the "effective" average tilt angles of ~30°, ~23°, and ~18° for the fluorocarbon segments in the F6H11SH, F8H11SH, and F10H11SH monolayers, respectively. The accuracy of these values is estimated to be ±3° or even somewhat lower. It is partly related to the uncertainty of the exact geometry of the fluorocarbon helix and to the simple angle subtraction procedure used to correct for the tilt of the CF_2 planes with respect to the chain axis. But the general tendency is clear: Orientational and conformational order of the fluorocarbon segments decrease with decreasing chain length, accompanied, probably, by an increase in its inclination (on the average).

In Figure 6.12, the schematic drawings of the molecular orientation in the FnH11SH SAMs are depicted. The NEXAFS-derived average tilt angles of fluorocarbon and hydrocarbon chains are indicated. Using the derived tilt angles and assuming a length of 1.3 Å,[62] 1.26 Å,[154] and 1.8 Å[8,155] for the $-CF_2-$, $-CH_2-$, and −C−S− units, respectively, we can calculate the thicknesses of the PFAT films. The respective values are 20.2, 22.9, and 25.9 Å for the F6H11SH, F8H11SH, and F10H11SH monolayers, which, with probably an exception of F10H11SH, agree well with the film thickness values calculated from the XPS data (section 6.1.2).

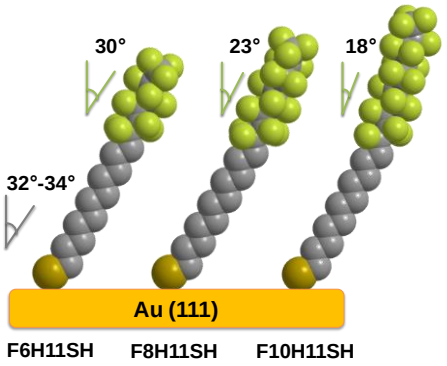

Figure 6.12: Schematic drawing of the molecular orientation in the FnH11SH SAMs on Au. The average tilt angles of the fluoro- and hydrocarbon segments are marked.

6.2 Discussion

The XPS, HRXPS, IRRAS, and NEXAFS data imply that the FnH11SH precursors form contamination-free, densely packed, and well-ordered SAMs on polycrystalline gold substrates with predominant (111) orientation. The molecules are bonded to the substrate by the thiolate-gold anchors, while the molecular backbones, consisting of the hydrocarbon and fluorocarbon segments, are oriented upright, as illustrated in Figure 6.12. The intermolecular packing density in the monolayers is governed by the fluorocarbon segments, which, according to the XPS (packing density), IRRAS (characteristic absorption modes), and NEXAFS (characteristic spectral envelope) data, have the helical conformation typical of these entities.

Generally, the helical conformation of fluorocarbon chain results from a rotation about the C–C bonds, which arises from dipolar repulsion between the 1,3-diaxial C–F bonds.[170] While a hydrocarbon chain can have a planar zigzag structure, the helical structure of the fluorocarbon chain is driven by the steric repulsion between the fluorine atoms of the adjacent $–CF_2–$ moieties since the van der Waals radius of a fluorine (1.35 Å)[64] is larger than that of a hydrogen (1.1-1.2 Å).[64] The respective twist angle is about 12-15° per C–C bond, and the dihedral angle between adjacent planes (each plane contains three neighboring carbon atoms) is 160-165°.[64,167,168] For a sufficiently long fluorocarbon chain, as can be found e.g. in PTFE, so called 15/7 and 13/6 helix structures are typical.[163-165] In particular, the 13/6 helical structure is formed in a way that a planar zigzag chain becomes twisted 180° within 16.8 Å, 6.5 zigzags or 13 chain atoms.[64] (Note that the full 360° twist of the chain occurs in 33.6 Å and involves 13 zigzags or 26 chain atoms, but the actual period is half of this, because a zigzag consists of two lines of atoms, and a half twist brings the fourteenth atom on the second line directly above the first atom on the first line). This type of helix has been reported to be the stable form at lower temperatures (<19°C) while the 15/7 helix is claimed to be the stable PTFE structure at room temperature.[163,164]

The number of the carbon atoms in the fluorocarbon segment of the FnH11SH precursors is much smaller than that associated with the full period of the 13/6 or 15/7 helix. Nevertheless, these parts keep this or a similar conformation, with the perfection which, according to the analysis of the NEXAFS data, reduces only slightly (if at all) with the decreasing length. This finding is supported by the results of the DFT calculations for the individual FnH11SH molecules, which resulted in similar parameters of the helix structures for n = 10, 8, and 6.

A characteristic feature of the FnH11SH SAMs is a slight decrease in the packing density with decreasing *n*, accompanied by the increase in the average tilt angle of the fluorocarbon segments. Generally, an increase in the average tilt angle does not necessary means a larger molecular inclination but a higher degree of conformational and orientational disorder. In the given case, association of the above average tilt angles with the inclination only will require noticeable changes (~9 %) in the packing density at going from F10H11SH to F6H11SH. Changes to such an extent are not observed, which only leave us with the assumption that the observed increase in the average tilt angle of the fluorocarbon segment with decreasing *n* is related to progressive deterioration of the orientational order in the fluorocarbon part of the FnH11SH SAMs. Note that dependence of the orientational order on the length of the precursors is typical for SAM-like systems[4,6] and can therefore occur in the FnH11SH monolayers as well. Note also that the organization of the fluorocarbon and hydrocarbon (see below) segments in these monolayers is governed by the different factors (intersegment interaction and bending potential, respectively), so that the respective parts of the SAMs can be considered as partly decoupled. In this sense, the change in the length of the fluorocarbon segments at going from F10H11SH to F8H11SH and further to F6H11SH is quite essential, resulting, as assumed above, in a partial deterioration of the orientational order. As to the conformational order, presumably, it contributes only slightly to the variation of the average tilt angle, since it is mostly persisting through the FnH11SH series, exhibiting only slight deterioration of the fluorocarbon helix with decreasing *n*.

The derived average tilt angle of the fluorocarbon chains for the F10H11SH monolayer (18°) agrees well with our previous result (20°),[139] which underlines the reliability of the experiments and data evaluation procedure. The observed partial deterioration of the orientational order of the fluorocarbon segments with decreasing *n* agrees with the tentative conclusions by Lee et al. made for the analogous PFAT monolayers on the basis of the thermostability and contact angle data.[145]

In contrast to the average tilt angles of the fluorocarbon segments, the average tilt angles of the hydrocarbon parts are almost the same for all studied FnH11SH monolayers, independent of the length of the fluorocarbon segments, as indicated by the NEXAFS data. In addition, the twist angles of the hydrocarbon segments in the FnH11SH SAMs are found to be quite similar as well, with these segments having the *all trans* planar conformation as implied by the IRRAS data. Significantly, the derived tilt (32-34°) and twist (52-53°) angles correlate well with analogous values of 27-35° and 53° for the non-substituted ATs on gold.[6,7,10-13] The presumable reason for this behavior is the bending potential of the thiolate bond, which enters

into the balance of the structure-building interactions and predefines the Au–S–C angle.[16,139] This angle, which is close to 104° for Au(111),[1] results then in certain inclination of the hydrocarbon segments, both in the non-substituted AT SAMs where the interchain spacing is close to the equilibrium value,[6] and in the PFAT monolayers where the hydrocarbon segments are separated beyond their equilibrium spacing due to the presence of the bulky fluorocarbon segments.[16,139] The equilibrium spacing can then only be achieved by a significantly stronger tilt of the hydrocarbon chains, which, however, works against the bending potential which appears to be stronger in the given case. Note that the effect of the bending potential has been observed in a variety of some other systems as well.[16,17,19,21,131] This potential is frequently associated with a certain hybridization of sulfur,[16,17,139] e.g. sp^3-hybridization for Au(111),[8] but the recent observation of the effect of the bending potentials for selenolate SAMs[24,25] makes this hypothesis questionable. It is well known that the extent of the sp hybridization is very small in the case of selenium, thus it should be rather referred to a bonding configuration of the anchor group without the reference to the hybridization.

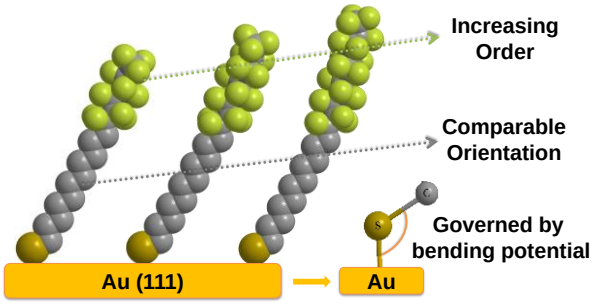

Summary of chapter 6

A series of SAMs formed on Au(111) by PFAT molecules with a variable length of the fluorocarbon segment and a constant length of the hydrocarbon segment, viz. FnH11SH (*n* = 6, 8, and 10) was studied using XPS, IRRAS, as well as synchrotron-based HRXPS, and NEXAFS spectroscopy. Independent of *n*, these segments were found to have helical and *all trans* planar conformations, respectively, typical of such entities. The packing density was governed by the bulkier fluorocarbon segments, with the average molecular spacing of 5.7-5.8 Å, close to the van der Waals diameter of this segment. A slight decrease in the packing density was observed with decreasing length of the fluorocarbon segments, which correlated with the increasing average inclination of these segments at going from the F10H11SH to F6H11SH monolayers. The observed change in the inclination was however much stronger than the variation of the packing density, which led us to the assumption that this change is mostly associated with a partial deterioration of the orientational order in the fluorocarbon part of the FnH11SH SAMs. The conformational order of the fluorocarbon segments was mostly persistent through the FnH11SH series, contributing only slightly to the observed variation of the segment inclination.

Whereas the orientational order in the fluorocarbon part of the FnH11SH SAMs varied with varying *n* and a slight variation of the conformational order could be assumed, the orientation and conformation of the hydrocarbon segments was found to be independent of this parameter. Both tilt and twist angles of the hydrocarbon segments are close to the analogous values for the non-substituted AT SAMs on Au(111), which was explained by the effect of the bending potential, predefining the Au–S–C bond angle. The energy contribution associated with this potential is obviously stronger than the thermodynamical drive to achieve the equilibrium spacing between the hydrocarbon segments through their larger inclination.

The above results underline once more the complexity of seemingly simple monomolecular films and the potential of a suitable combination of complementary spectroscopic (and microscopic) techniques to get insight and better understanding of the structure and organization in these systems.

Chapter 7: Structure of Self-Assembled Monolayers of Partially Fluorinated Alkanethiols on GaAs (001) substrate

In chapter 6, the structure and organization of the FnH11SH (*n*= 6, 8, 10) SAMs on Au has been discussed in detail by a combination of several complementary spectroscopic techniques. Here in this chapter, similar approach was used to study the same series of FnH11SH SAMs on GaAs (001) substrate, and the structure-building factors for molecular assembly on this complex semiconductor substrate were additional studied by unraveling the structure of these PFAT films.

In addition, it has to be noted that, till now only limited substituted ATs have been used for the molecular assembly on GaAs substrate,[50-53] these molecules include the carboxylic-acid[52]and thiol[50,51] terminated ATs, as well as the polyethylene-glycol (PEG) and biotinylated PEG based thiols.[53] Here, we are the first to apply these novel PFAT precursors for the molecular assembly on the GaAs (001) substrate.

7.1 Results

7.1.1 HRXPS and XPS

The formation of high quality FnH11SH and ODT SAMs on GaAs (001) was firstly manifested in the As 3d and Ga 3d HRXPS spectra, which are shown in Figure 7.1. As seen, after decomposing into individual spectral components, these spectra are dominated by the peaks from stoichiometric GaAs (light gray doublets), which are accompanied by much weaker contributions from elementary As (dark gray doublets in As 3d spectra) and surface states (dark gray doublets in Ga 3d spectra). In the As 3d spectra, a black doublet assigned to As–S could be traced at ~42.3 eV (As $3d_{5/2}$), which means that these FnH11SH and ODT

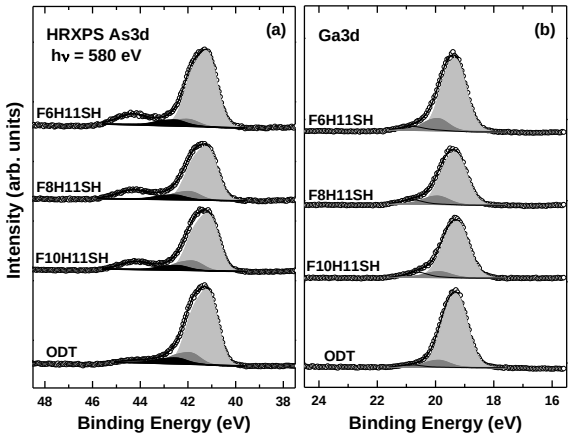

Figure 7.1: As 3d (a) and Ga 3d (b) HRXPS spectra of FnH11SH (n= 6, 8, and 10) and ODT SAMs on GaAs (001). The spectra were acquired at a photon energy of 580 eV. The spectra are tentatively decomposed in several doublets related to individual chemical species: (a) As 3d spectra: Light gray, stoichiometric GaAs; dark gray, elementary As; black, S-As. (b) Ga 3d spectra: Light gray, stoichiometric GaAs; dark gray, Ga oxide or surface Ga 3d component. The shoulders at higher binding energy side correspond to As oxides. The assignments were performed in accordance with refs 44, 55, 58, 59.

molecules are preferably bonded to the As atoms. In contrast to the As3d spectra, the decomposition of the Ga3d spectra does not require an introduction of an additional (with respect to the bulk GaAs component) doublet related to the Ga-S species. Nevertheless, the existence of these species can not be completely excluded,[33,48,49] due to the ambiguous spectra fitting in the relevant binding energy region.

Along with the above characteristic features, there are weak signals related to oxides (As_xO_y and Ga_xO_y) at higher BE side. The small extent of oxidation suggests, however, dense molecular packing in these FnH11SH and ODT SAMs.[55,58] In Figure 7.1, the respective As 3d and Ga 3d spectra of ODT SAM are included for a comparison, the exhibited nearly oxidation free feature agrees with the analogous results in previous literatures, in particular by D. L. Allara et al;[33,44] this suggests the reliability of the experimental process, in particular considering the nontrivial task of molecular assembly on GaAs substrate. In contrast to the nearly oxidation free feature of ODT SAM, the oxide-related signatures appear somewhat more for the FnH11SH monolayers, and the spectra proportion for these signatures increases slightly with decreasing the fluorocarbon chain length at going from F10H11SH to F6H11SH, as can be identified in the As 3d spectra in particular.

The formation of high quality FnH11SH SAMs were further supported by the S 2p HRXPS spectra in Figure 7.2 (a), along with the O 1s and F 1s spectra in Figure 7.2 (b) and (c), respectively. All the S 2p (a) spectra exhibit one single doublet at a characteristic BE position of ~162.4 eV (S $2p_{3/2}$), with no traces of unbound, disulfide, or oxidized species being detected; the above BE value coincides with the analogous values observed previously for both aliphatic and aromatic SAMs on GaAs (001),[44,55,56,58,59] suggesting that all these FnH11SH molecules bond to the substrate via a thiolate-GaAs bonding mode. Note this BE value (162.4 eV) is noticeably higher than that (162.0 eV) for the thiol-derived SAMs on noble metal substrates,[7,76,101,102] presumably related to the screening of the photoemission hole by the substrate electrons in the case of metal.[44] The fwhm values (0.9-1.0 eV) of the S $2p_{3/2}$ and S $2p_{1/2}$ peaks for these FnH11SH monolayers are close to those for non-substituted AT SAMs on GaAs, but are noticeably larger than the analogous values for AT SAMs on noble metal surfaces (0.55-0.6 eV),[76,80] this indicates the higher inhomogeneity of the bonding configuration at the SAM-GaAs interface as compared to the SAM-metal interface.[44] The intensity of the S 2p doublet decreases with increasing the length of the fluorocarbon segments at going from F6H11SH to F10H11SH, which agrees well with the expected

attenuation effect, i.e. the respective photoelectron signal is attenuated more for the intact FnH11SH SAMs with thicker film, such as F10H11SH SAM.

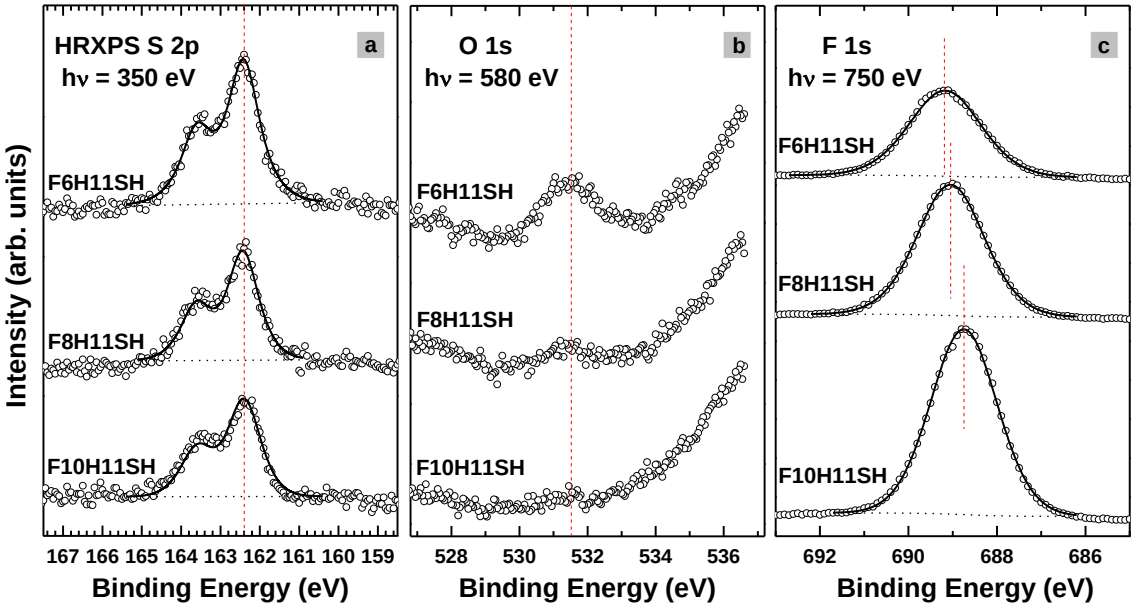

Figure 7.2: S 2p (a), O 1s (b), F 1s (c) HRXPS spectra of the FnH11SH (n= 6, 8, and 10) SAMs on GaAs (001). The spectra were acquired at photon energies of 350 eV (a), 580 eV (b), and 750 eV (c), respectively. The vertical dashed lines highlight the BE positions of the emissions.

In the O 1s spectra (Figure 7.2b), only a small signal, correlated with the oxide-related feature in the respective As 3d and Ga 3d spectra (Figure 7.1) at the same PE (580eV), is observed for F6H11SH SAM, while nearly no emission signal is observed for the other two films. This agrees with the As 3d and Ga 3d spectra feature of these films, viz. less oxidation is observed for FnH11SH SAM with longer fluorocarbon segment.

The F 1s spectra of FnH11SH SAMs in Figure 7.2 (c) exhibit only one emission peak related to the fluorocarbon chain, since it has been well accepted that CF_2 and CF_3 species can not be differentiated in this spectral region.[63,80,82,139] As expected, the peak intensity increases when increasing the fluorocarbon chain length. At the same time, the BE position moves downwards with increasing the length of the fluorocarbon segments; this downward movement is also observed in the same series of FnH11SH monolayers on Au (Figure 6.4), which can be explained by the vacuum-level-like pinning of the energetic levels in SAMs.[148-151] According to this pinning model: BE positions of the C 1s and F 1s emissions depend on the work function of the system; the latter parameter increases with increasing the length of the fluorocarbon segments, and hence leading to the downward shift of the respective emission.[80,150,151]

In addition, the BE positions of FnH11SH SAMs on Au and GaAs substrates were compared in Table 7.1, it is found the BE value is larger for each FnH11SH monolayer on GaAs (001) as compared to that for Au, which is presumably related to the photoscreening effect in the case of metal. Note this effect also occurs in the S 2p spectra, which results the larger BE value (S $2p_{3/2}$ peak) for FnH11SH SAMs on GaAs as compared to Au (162.4 versus 162 eV).

Table 7.1: F 1s Binding Energy Positions for FnH11SH (n = 6, 8, 10) SAMs on GaAs(001) and Au(111)

	F10H11SH	F8H11SH	F6H11SH
GaAs (001)	688.7	689	689.2
Au (111)	688.3	688.45	688.6

Adsorption of intact FnH11SH molecules on GaAs (001) surface and formation of well-defined SAMs are further confirmed by the C 1s HRXPS spectra in Figure 7.3, which were acquired at PEs of 350 and 580 eV, respectively. These spectra exhibit three distinguished peaks of different intensities, while the first two asymmetric ones can be decomposed into individual emissions. After decomposing, emissions 1 and 2, emissions 3 and 4, and emission 5 can be clearly assigned to the hydrocarbon ($-CH_2-$) part, the fluorocarbon ($-CF_2-$) part, and the CF_3 terminal moiety, respectively.[80,82,139] Emission 2 corresponds to the terminal moiety connected to the fluorocarbon chain, resulting in an increase of the respective BE position as compared to all other $–CH_2–$ units (emission 1). Similarly, emission 3 is related to the terminal $–CF_2–$ moiety linked to the hydrocarbon chain, leading to the decrease of the respective BE value as compared to all other $–CF_2–$ units (emission 4).

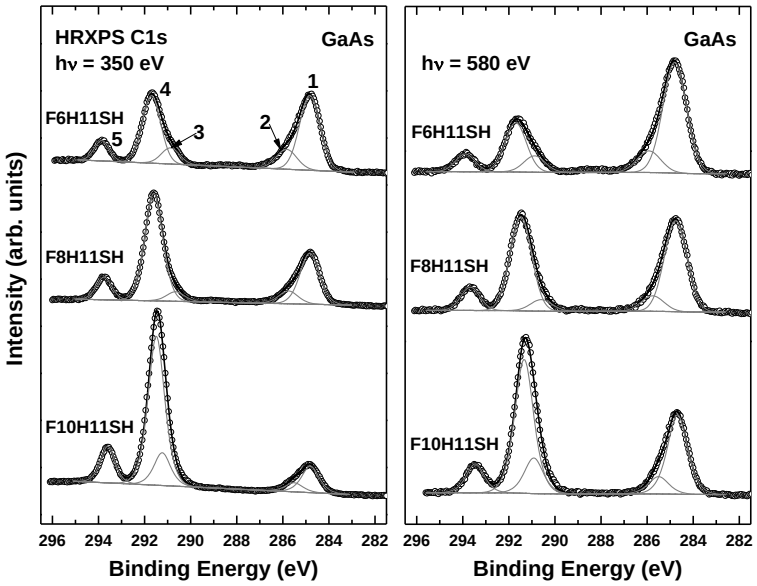

Figure 7.3: C1s HRXPS spectra of the FnH11SH (n= 6, 8, and 10) SAMs on GaAs (001). The spectra were acquired at photon energies of 350 (left) and 580 (right) eV, respectively. The spectra are decomposed into individual emissions (gray solid lines) within a fitting procedure; these emissions are marked by numbers. (see text for detail)

In the C 1s spectra taken at both PEs, the intensities of the individual emissions show the expected behavior with varying *n*. The intensity of the peak 5 (CF_3 terminal moiety) increases slightly with increasing the length of the fluorocarbon segments. Considering that the constituents of all these SAMs have only one CF_3 terminal moiety, which, according to the standard architecture, is located at the SAM-ambience interface, the respective photoemission signal should only depend on the molecular density. The latter parameter seems then to increase slightly with increasing the fluorocarbon chain length. The intensities of fluorocarbon part (peak 3 and 4) increase with increasing the length of the fluorocarbon chain as can be expected. By contrast, the intensities of hydrocarbon part (peak 1 and 2) have an opposite behavior even though they all have the same hydrocarbon chain length; the intensity decrease is attributed to the stronger attenuation of the respective photoemission signal by the longer fluorocarbon chain, such as in F10H11SH SAM. Based on these considerations, one can consider this intensity decrease as an additional proof for the expected, upright orientation of the SAM constituents, anchored to the GaAs surface through the thiolate bond (see Figure 7.2a). This statement is further supported by comparing the C 1s spectra taken at different PEs: for each FnH11SH SAM, the relative intensity of the $–CH_2–$ components increases with increasing the PE from 350 eV to 580eV, following the increasing probing sample depth, which is caused by the increase of the attenuation length.[70]

In addition to the spectral analysis, the film thicknesses of the FnH11SH monolayers were calculated based on the XPS results by evaluating the intensity ratios of the C 1s and As 3d emissions according to equation (5–4) in chapter 5,[126,153] and using ODT/GaAs SAM with a thickness of 23.8 Å[34] as a reference model. The derived thickness values were 17.6 Å, 20.4 Å, and 23.9 Å for F6H11SH, F8H11SH, and F10H11SH monolayers, respectively.

Furthermore, the packing densities were coarsely calculated from the HRXPS results using S2p/As3d intensity ratio following the approach of Refs [128] and [129], and ODT/GaAs SAM with the packing density of 21.2 $Å^2$ per chain was selected as a reference.[45] The obtained values for F6H11SH, F8H11SH, F10H11SH monolayers were 27.5, 27.2, and 27.5 $Å^2$ per chain, respectively. Here, the packing densities were calculated using the S 2p and As 3d HRXPS spectra acquired at a PE of 350eV; however, we have to note the real packing densities should be calculated using the spectra taken at higher PE, like those taken under normal lab XPS setup, since the photoelectrons for the S 2p and As 3d emissions are attenuated similarly taking into account of their higher kinetic energy. However, the S 2p emission in that case can not be distinguished since it is totally covered by the strong Ga 1s

emission at the BE position of ~160 eV. As for the HRXPS spectra taking at PE of 350 eV, despite the packing densities can be calculated, the read trend for this parameter will deviate from the calculated result due to the strong attenuation effect, which has to be taken into account at this PE level. The photoelectrons from S 2p emission are attenuated more compared with those from As 3d emission as a result of their lower kinetic energy (183eV versus 304eV), keeping this in mind, the S2p/As3d intensity ratio can be underestimated, and this underestimation is more obvious for thicker FnH11SH monolayer. Therefore, the packing densities of these FnH11SH SAMs should increase slightly with increasing *n* rather than keep similar values.

In addition to the slight increase of packing density with increasing the fluorocarbon chain length, it should be noted that these calculated packing densities (27.2~27.5 $Å^2$ per molecule) are close to those (27.7-28.4 $Å^2$ per molecule) for the FnH11SH SAMs on Au, and also noticeably larger than the analogous value for non-substituted AT SAM on GaAs (001) (~21.2 $Å^2$ per molecule)[45]; these larger values (compared with 21.2 $Å^2$ per molecule) can be associated with an intermolecular spacing of 5.67-5.7 Å, close to the van der Waals diameter of this chain (5.67 Å) and to the lattice constant observed in previous AFM studies on PFAT monolayer systems on Au (5.7-5.9 Å).[63,65,135,147] Thus, the packing density of these FnH11SH/GaAs SAMs is also primarily governed by the bulky fluorocarbon segment, typical of the helical conformation; it does not change significantly with the varying length of the fluorocarbon part, only decreases slightly with decreasing *n*. Note that the attenuation length for photoelectrons in fluorocarbon films are almost indistinguishable from those in hydrocarbon films,[142] which justifies the use of the ODT/GaAs SAM as a reference for the evaluation of the effective film thickness and packing density.

7.1.2 IRRAS

In section 6.1.3 in chapter 6, the IR dataset of FnH11SH SAMs on Au has been studied systematically. Unlike the IRRAS spectra of FnH11SH/Au SAMs, the C-H stretching region in the IRRAS spectra for FnH11SH/GaAs SAMs does not yield a noticeable signal. Because the intensity in the present case was – as expected – much lower as compared to SAMs on metal substrates where a substrate-mediated amplification of the FTIR signal occurs. Further, since the induced dipole is much weaker in the case of semiconductors as compared to metals, the selection rules are less strict, which makes it even more difficult to get the structural information from the IRRAS data.

The IRRAS spectra of the F10H11SH SAM on GaAs(001) in the range of the C-F stretching modes is depicted in Figure 7.4. This region exhibits pronounced stretching and bending modes of the CF_2 groups, and the characteristic bands are marked with numbers like the FnH11SH SAMs on Au (chapter 6), the assignment of these bands along with their corresponding TDMs are provided in Table 6.1 in chapter 6. Interestingly, both positive and negative absorbance features appear in the reflection spectra in Figure 7.4, which can be explained by the well-known effects involving strong perturbations of the electric fields by the real part of the optical functions of the film in the case of dielectric substrates.[34]

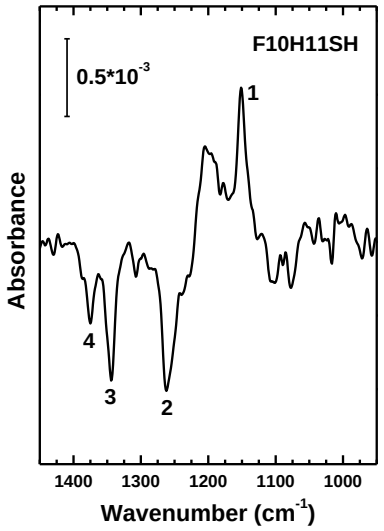

Figure 7.4: IR spectra of the F10H11SH SAM on GaAs (001) in the range characteristic of the CF_2 vibrations. The scale bar indicates the absorbance intensity. The most prominent bands are marked with numbers. See text for details.

Absorption bands 3 and 4 at ~1345 and ~1375 cm^{-1}, respectively, are identified as axial CF_2 stretching vibrations with a strong component of the dynamic dipole moment along the helical axis.[134] These two characteristic modes for the helical conformation of the fluorocarbon chain are commonly observed in thin organic films containing these entities.[65,66,134,139,147] In the present case, these modes are clearly seen, which implies that the fluorocarbon segment in the densely packed F10H11SH/GaAs SAM adopts the expected helical conformation. It has to be noted that, the positions of these two bands depend on the fluorocarbon chain length,[66,141] which as suggested by Colorado et al.,[141] can be used to determine the length of the fluorocarbon segment in PFAT SAMs regardless of the orientation of the segments within the film. The above conclusion also applies without considering the type of substrate, since the positions of these two bands are the same for F10H11SH SAMs on Au and GaAs(001).

The intense absorption bands in the 1150–1250 cm^{-1} region are also characteristic of fluorocarbon entities. The pronounced bands 1 (~1151cm^{-1}) and 2 (~1262cm^{-1}) have, in contrast to the axial CF_2 stretches at ~1345 and ~1375 cm^{-1}, a significant contribution from the asymmetric CF2 stretching vibration with a dynamic dipole moment perpendicular to the helical axis.[134] These modes are commonly observed both for PTFE and for thin organic films containing fluorocarbon segments.[2,66,134,139]

7.1.3 NEXAFS spectroscopy

Carbon *K*-edge NEXAFS spectra of FnH11SH monolayers acquired at an X-ray incidence angle of 55° are shown in Figure 7.5 (a), the spectra taken at this "magic" angle are not affected by the molecular orientaion,[72] and can only reflect the electronic structure of the target systems. The spectra in Figure 7.5 (a) contain two absorption edges at ~287.9 and ~294.0 eV related to the C1s → continuum excitations for the carbon atoms bonded to hydrogen and fluorine, respectively. The spectra are dominated by the pronounced resonances at positions of ~292.5, ~295.5, and ~298.8 eV; these resonances are typical of the fluorocarbon part, and are assigned for the transitions from the C1s state to the C-F σ^*, C-C σ^*, and C-F´ σ^* molecular orbitals, respectively.[80,82,160-162,134,139] The corresponding transition dipole moments (TDMs) are believed to be almost perpendicular (C1s → C-F σ^*) or along (C1s → C-C σ^*) the chain axis.[108,160,161,134] As to the hydrocarbon chain part, only a weak feature at ~287.9 eV, alternatively assigned to the C1s excitations into predominantly Rydberg states,[105,106] valence C-H orbitals,[72] or mixed valence/Rydberg states,[104] is discernible, while its corresponding TDM is oriented perpendicular to the alkyl chain axis.[82,107,108] The further characteristic C-C σ^* and C-C´ σ^* resonances of the hydrocarbon part at positions of ~293 and ~302 eV, respectively,[82,107,108] are hardly distinguishable in the spectra since they overlap with the strong features related to the fluorocarbon segment.

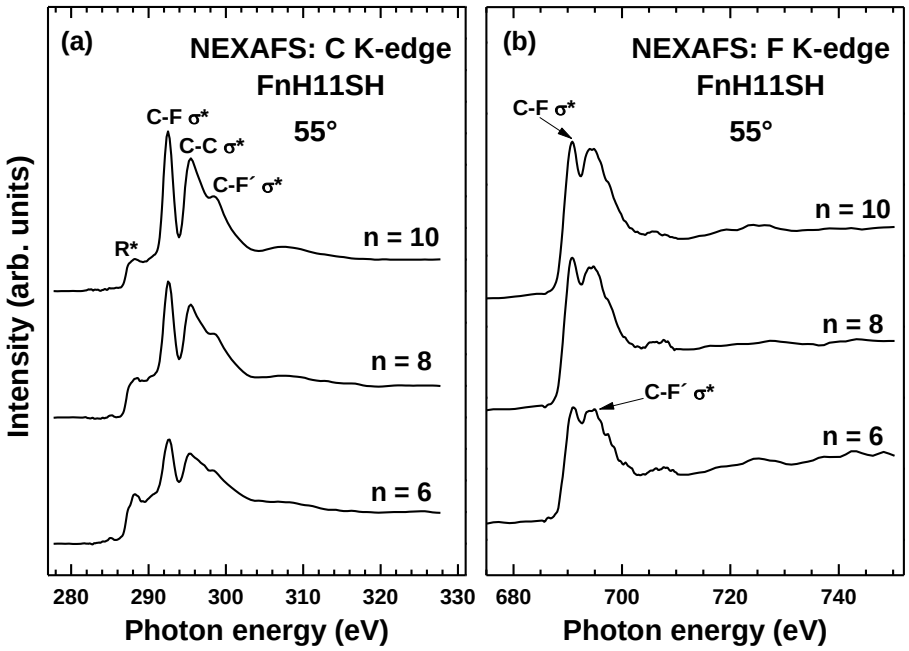

Figure 7.5: Carbon *K*-edge (a) and Fluorine *K*-edge (b) NEXAFS spectra of the FnH11SH (n= 6, 8, and 10) SAMs on GaAs (001) acquired at an X-ray incident angle of 55°. The characteristic NEXAFS resonances are indicated.

Both the positions of the resonances related to the fluorocarbon segments and the entire spectral shape are very similar to the calculated NEXAFS spectra of PTFE in the standard[163,164] 13/6 (or 15/7) helical conformation of the fluorocarbon chains;[165] this behavior suggests that the fluorocarbon segments in these FnH11SH SAMs adopt the expected standard helical conformation, which is also supported by the HRXPS and IRRAS results. The definite structure models about the 13/6 and 15/7 helical conformation have been given,[64,80] and it is difficult to distinguish between these two helix based on the NEXFAS data. As known, distortion of the helical conformation of the fluorocarbon chain is assumed to modify the corresponding NEXAFS spectra, with the extent depending on the degree of distortion:[165] Large distortion would induce a complete change of the spectral envelope, while moderate distortion would lead to some shift and/or broadening of the absorption resonances.[165] In the present case of FnH11SH SAMs, the general spectra envelopes are similar among all studied monolayers, suggesting that no noticeable disturbance of the helix structure occurs with varying the length of the fluorocarbon segment.[165] At the same time, the peaks assigned for the characteristic resonance of the fluorocarbon segments become slightly broader with decreasing the fluorocarbon chain length, e.g. the fwhm values for the peak of C-F σ^* resonance are 1.42, 1.49, and 1.55 eV for F10H11SH, F8H11SH, and F6H11SH monolayers, respectively. This tendency suggests some minor distortions of the expected helical conformation occurring in the FnH11SH SAMs with smaller *n*.

Fluorine *K*-edge NEXAFS spectra of FnH11SH monolayers acquired at an X-ray incidence angle of 55° are presented in Figure 7.5 (b). These spectra are dominated by two pronounced resonances at ~690.8 eV and ~696.4 eV assigned to the transitions from the F1s core level to the C-F σ^* and C-F´ σ^* orbitals. In addition, these spectra are very similar to those of PTFE[166] as well as FnH11SH monolayers on Au, both of which exhibit the “standard” helical conformation in the fluorocarbon segments, thus, the similarity to them can be considered as additional evidence for the same conformation of the fluorocarbon segments in these FnH11SH/GaAs monolayers.

As introduced about NEXAFS spectra, the information about orientational order and molecular tilt of these FnH11SH SAMs can be obtained from the linear dichroism of the NEXAFS spectra, i.e., their dependence on the X-ray incidence angles.[72] A convenient way to monitor the linear dichroism is to calculate the difference between the spectra acquired at normal (90°) and grazing (20°) incidence of X-rays. Such C *K*-edge difference spectra are presented in Figure 7.6. They exhibit pronounced peaks at the position of the absorption resonances, which highlights the strong dependence of the resonance intensity on the angle of X-ray incidence, typical for well-ordered, densely packed monomolecular films. As expected, the resonances with TDMs oriented perpendicular (e.g., C-F σ^* or R^*) or along (e.g., C-C σ^*) the axis of the fluorocarbon and hydrocarbon segments show opposite behaviors with the varying incidence angles of X-rays. The positive peaks at the positions of the R^* and C-F σ^* resonances and negative peak at the position of C-C σ^* resonance in the difference spectra indicate predominantly perpendicular orientation of both the fluorocarbon and hydrocarbon segments in the FnH11SH SAMs.

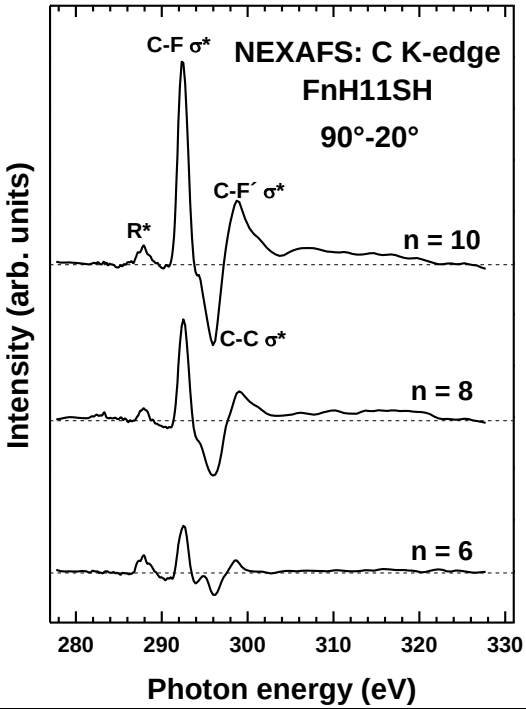

Figure 7.6: Difference between the Carbon K-edge NEXAFS spectra of the FnH11SH (n= 6, 8, and 10) SAMs on GaAs (001) at the normal (90°) and grazing (20°) incidence of X-rays. The difference peaks corresponding to the characteristic absorption resonances are marked.

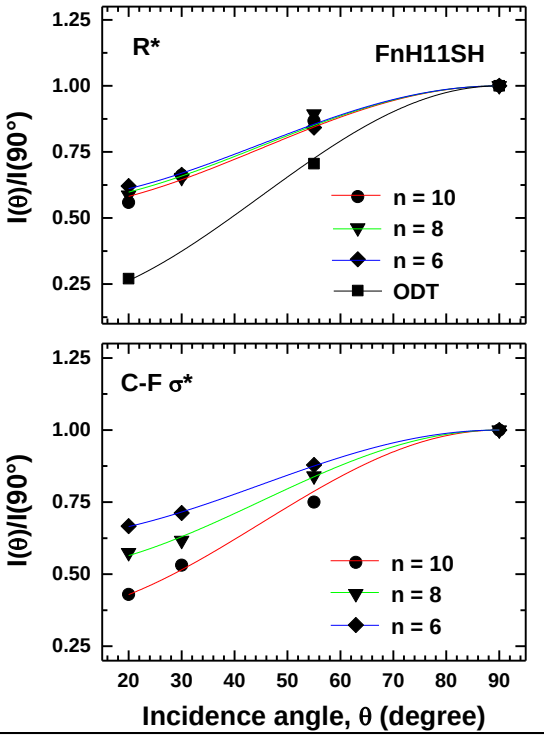

Figure 7.7: The angular dependence of the I(θ)/I(90°) intensity ratios for the R^* (top panel) and C–F σ^* (bottom panel) resonances for the F10H11SH (circles), F8H11SH (triangles) and F6H11SH (diamonds) SAMs on GaAs (001), along with the best theoretical fits (solid lines). In the case of the R^* resonance, ODT SAM (square) is included as a reference; the fitting curves for the FnH11SH SAMs almost coincide practically and are therefore hardly distinguishable.

The above qualitative considerations were complemented by the quantitative analysis of the NEXAFS data within the standard theoretical framework.[72] The average tilt angles of the fluorocarbon and hydrocarbon chains can be derived by a numerical evaluation of the NEXAFS data, analyzing angular dependence of the C-F σ^* and R^* resonance intensities using the standard formula (equation 4–1) for a plane-type orbital:[72]

$$I(\alpha,\theta)=A\left\{P\times\frac{2}{3}\left[1-\frac{1}{4}\cdot(3\cdot\cos^2\theta-1)\cdot(3\cdot\cos^2\alpha-1)\right]+(1-P)\times\frac{1}{2}\cdot(1+\cos^2\alpha)\right\} \quad (4\text{–}1)$$

Where A is a constant, P is the polarization factor of the X-rays, and α is the angle between the sample normal and normal direction of the molecular orbital plane. Here, both C-F σ^* and R^* orbitals were considered as plane ones, which is justified the R^* orbital is composed of two mutually perpendicular orbitals with almost identical intensities,[104] while the C-F σ^* orbital can be related to the CF_2 plane in the same manner as the R^* orbital.[80]

The C-F σ^* resonance was selected because of its high intensity and its separation from the other resonances, while the R^* resonance was chosen as the only distinguishable resonance related to the hydrocarbon chain part in the present case. The extraction of the intensities for these two resonances has been introduced by the example of F10H11SH/Au SAM in chapter 6. To avoid normalization problems, not the absolute intensities but the intensity ratios $I(\theta)/I(90°)$ were analyzed,[72] where $I(\theta)$ and $I(90°)$ are the intensities for σ^* (or R*) resonance at X-ray incidence angles of θ and 90°, respectively. The angular dependences of the intensity ratios for R^* and C–F σ^* resonances are presented in Figure 7.7 along with the best theoretical fits.

The fits of the measured angular dependencies for the R^* resonance intensity by the theoretical expression give average tilt angles of ~39°, ~39°, ~40° for the hydrocarbon segments in F10H11SH, F8H11SH, and F6H11SH SAMs, respectively, suggesting that this parameter does not depend on the length of the fluorocarbon segments. The fitting results of the ODT SAM is also included as a comparison, the resulted value of the average tilt angle (~16°) coincides well with the analogous values (~14°) obtained based on the NEXAFS and IRRAS data.[34] The accuracy of these values is ± 3°. The major source of errors comes from the relatively (as compared to σ^* C–F and σ^* C–C) low intensity of the R^* resonance and the uncertainty of the exact location of the C1s (C–H) absorption edge. Significantly, these obtained values (~39−40°) are noticeably larger than that (~16°) for ODT monolayer, which has a comparable chain length with the studied FnH11SH (n = 6, 8, 10) precursors, and are

close to the optimum tilt value (~27−35°) governed by the bending potential. (the Au-like bending potential has already been discussed in chapter 5)

The fits of the measured angular dependencies for the C-F σ^* resonance intensity by the theoretical expression give average tilt angles of ~30°, ~38°, ~42° for the fluorocarbon segments in F10H11SH, F8H11SH, and F6H11SH SAMs, respectively. It should be noted, however, that these values were obtained assuming that the molecular plane of the CF_2 entities is exactly perpendicular to the fluorocarbon chain axis.[134] In reality, these planes are slightly tilted toward the helix axis with the tilt depending on the helix parameters. Assuming the standard 15/7 helix for the fluorocarbon segments of these FnH11SH SAMs and using the same subtraction procedure described in section 6.1.4,[80,82,139] viz. 8° is subtracted from the above values, the obtained "effective" tilt angles are ~22°, ~29°, ~34° for the fluorocarbon segments in the F10H11SH, F8H11SH, and F6H11SH monolayers, respectively. The accuracy of these values is estimated to be ±3° or even somewhat lower. It is partly related to the uncertainty of the exact geometry of the fluorocarbon helix and to the simple angle subtraction procedure used to correct for the tilt of the CF_2 planes with respect to the chain axis. From these "effective" tilt angles, the general tendency is clear: Orientational and conformational order of the fluorocarbon segments decreases with decreasing fluorocarbon chain length, accompanied, probably, by a slight increase in its inclination (on the average).

In Figure 7.8, the schematic drawings of the molecular orientation in FnH11SH/GaAs SAMs are depicted. The NEXAFS derived average tilt angles of both the fluorocarbon and hydrocarbon chains are indicated. Using the derived tilt angles and assuming a length of 1.3 Å,[62] 1.26 Å,[154] and 2.3 Å[46] for CF_2, CH_2, and −S− units, respectively, the thickness of these FnH11SH SAMs can be calculated, the respective values are 19.4 Å, 22.1 Å, and 25.1 Å for F6H11SH, F8H11SH, and F10H11SH SAMs. Note the NEXAFS derived thickness values are somewhat larger than those derived from XPS results, presumably because the "effective" tilt angles of the fluorocarbon segments mostly reflect the degree of the orientation order rather than the real inclination. (see more in discussion section below)

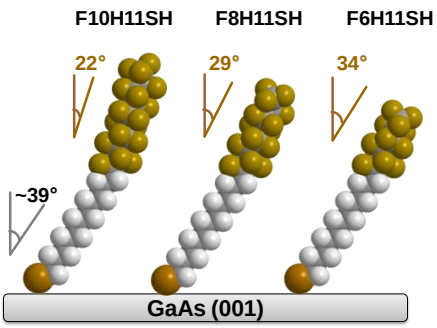

Figure 7.8: Schematic drawing of the molecular orientation in the FnH11SH SAMs on GaAs (001). The average tilt angles of the fluoro- and hydrocarbon segments are marked.

7.2 Discussion

The HRXPS and NEXAFS data indicate that FnH11SH precursors form contamination free, well ordered, and densely packed SAMs on GaAs (001) surface; these layers can passivate the GaAs substrate, further protect it effectively from oxidation. The molecules are strongly bonded to the bare GaAs substrate through the conventional thiolate bond, with predominantly bonding to As atoms. Both the hydrocarbon and fluorocarbon segments in the molecular backbone are orientated upright, as presented in Figure 7.8. The packing density of these PFAT monolayers is primarily governed by the fluorocarbon segments, which, according to HRXPS (packing density), IRRAS (characteristic absorption modes), and NEXAFS (characteristic spectral envelope) data, keep the helical conformation typical of these entities.

7.2.1 Protection Ability – chain length effect

The HRXPS spectra (Figure 7.1 and 7.2b) of the FnH11SH SAMs all exhibit weak oxide-related features, which proves the high quality of these films on GaAs (001) surface.[44,55,58] In addition to this general rule, the oxide-related features were found to be less intense for the FnH11SH SAM with longer fluorocarbon segment, this can be attributed to two effects: on one hand, the "self-cleaning" process[44] is more effective for molecules with longer chain length;[44] on the other hand, the SAM with longer chain can protect the surface more effectively from post-oxidation, which happens mostly during the transport and handling of the samples. Between these two effects, the latter "protection effect" is assumed to be more important in determining the extent of oxidation,[59] in particular taking into account of the strong proneness of GaAs substrate towards oxidation. Despite the substrate is protected by the SAMs, this protection worked presumably to a certain extent only, so the oxidation of the airborne species was in principle possible.

The better protection by the FnH11SH SAM with longer fluorocarbon chain is related to its higher film quality. In chapter 4, by using the example of the NSAT SAMs with different length ($C_nH_{2n+1}SH$), We have demonstrated the chain length dependence for SAMs on GaAs, viz. better film order and higher coverage can be obtained for the SAM with longer molecular chain length.[33,44,45] Later in chapter 5, this chain length effect also contributes to structural building factors in the BPn (n=1 – 6) SAMs, resulting the relatively poor quality for BPn (n=1, 2) SAMs with shorter alkyl linker. The chain length is mainly associated with the intermolecular packing force, which drives the surface GaAs atoms reconstruction during the

molecular assembly. In the present case of more complex SAM system, instead of the hydrocarbon chain, the length of fluorocarbon chain is varied; however, the chain length effect should also apply irrespective of the chain composition (–CF_2– or –CH_2–), and consequently result the higher quality and correlated, better protection property for the FnH11SH monolayer with larger *n*.

7.2.2 Fluorocarbon segments

In the given FnH11SH SAM systems, the length of the fluorocarbon segments is varied, thus the above mentioned chain length effect mainly contributes to the organization of these segments. Note that the organization of the fluorocarbon and hydrocarbon (see below) segments in these monolayers is governed by the different factors (intermolecular interaction and bending potential, respectively), so that the respective parts of the SAMs can be considered as partly decoupled. In this sense, the change in the length of the fluorocarbon segments at going from F10H11SH to F8H11SH and further to F6H11SH is quite essential, resulting in the decaying quality, namely the decreasing packing density and order of these segments. As known from HRXPS, the former parameter decreases slightly with decreasing *n* (the packing density of these FnH11SH SAMs is governed by the fluorocarbon part), however, this tendency does not correlate with the observed change of the average tilt angles of these segments. (22°→29°→34°, see Figure 7.8) For example, if the obtained tilt angles are associated with the inclination, noticeable decrease (~11%) in the packing densities at going from F10H11SH to F6H11SH SAM would be observed, however, such decrease is not detected. As known, an increase in the average tilt angle does not necessarily mean a larger molecular inclination but a higher degree of orientational and conformational disorder. Taking into account of the similar case for the FnH11SH/Au SAMs (chapter 6), the observed increase in the average tilt angle of the fluorocarbon segment with decreasing *n* is also mainly related to progressive deterioration of the orientational order in the fluorocarbon part of the FnH11SH/GaAs SAMs. As to the conformational order, it mostly persists through the FnH11SH series, accompanied by a slight deterioration of the fluorocarbon helix with decreasing *n*; and thus contributes only slightly to the variation of the average tilt angle.

For these FnH11SH SAMs on both GaAs (001) and Au substrates, the average tilt angles of the fluorocarbon segments increase with decreasing the length of these moieties. In addition to this general tendency, it should be noted: for each FnH11SH SAM, the value of this angle is larger for GaAs as compared to Au, (22° versus 18° for F10H11SH, 29° versus 23° for F8H11SH, and 34° versus 30° for F6H11SH); since this average tilt angle, as

discussed above, is mostly a reflection of the orientational order of the fluorocarbon segment, it is suggested that the orientational order of the fluorocarbon part is lower in the FnH11SH SAMs on GaAs as compared to Au, this is presumably related to the relatively shorter range order for the SAMs on GaAs.[33,45]

7.2.3 Hydrocarbon segments

In contrast to the fluorocarbon parts, the hydrocarbon segments exhibit similar orientation (~39°), which is independent of the length of the fluorocarbon segments. The similar tilt of the hydrocarbon segments in these FnH11SH monolayers is presumably caused by the bending potential of the anchoring (GaAs-S-C) bond; this potential enters into the balance of the structure-building interactions and predefines the GaAs-S-C angle, and thus results in a preferred orientation of the hydrocarbon chain. The existence of the bending potential for AT SAMs on GaAs has already been proven by investigating the odd-even effects in the TPn and BPn SAMs in chapter 5; this potential behaves like that for AT SAMs on Au rather than on Ag.[59] In the present FnH11SH/GaAs SAMs, the derived values of the average tilt angles (~39°) are close to the analogous values for both non-substituted alkanethiol (27–35°)[6,7,10-13] and FnH11SH SAMs (~32–34°)[80,139] on Au, suggesting the predominant role of bending potential in determining the orientation of the hydrocarbon segments in these FnH11SH/GaAs SAMs. However, the derived values of the average tilt angles (~39°) are slightly larger than the analogous value determined by the bending potential (27–35°),[59] this presumably suggests some conformational disorder of the hydrocarbon segments in these FnH11SH SAMs, i.e. the conformation of these segments is distorted to some extent as compared to the *all trans* form. Note the deterioration of the conformation order for short hydrocarbon chain, which is just the present case, has been observed in the study of DDT SAM on GaAs (001).[45]

Despite the bending potential model explained the similar tilt of the hydrocarbon segments, it has to be noted the average tilt angles of the hydrocarbon segments coincide with the free joint model. According to this model, the most favorable intermolecular interaction is maximized with the equilibrium chain-chain distance near ≈4.4 Å.[2,14] From the HRXPS results, the lattice distance for these FnH11SH monolayers is calculated to be ~5.7 Å, and these tilt angles (~39°) are well suitable to achieve the equilibrium spacing (4.4 Å) between the hydrocarbon chains. (the intermolecular spacing is equal to the 2D lattice constant multiplied by the cosine of the tilt angle) However, we think that the existing conformation disorder of the hydrocarbon segments is mostly responsible for these slightly larger angles (~39°) within the free joint model.

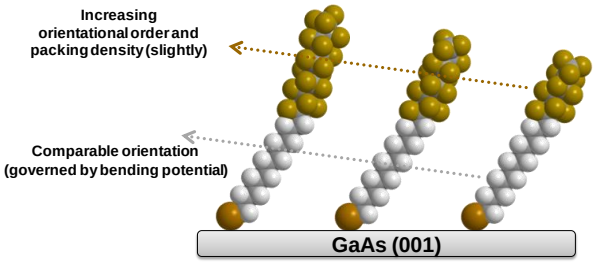

Summary of chapter 7

A series of SAMs formed on GaAs (001) by PFAT molecules with a variable length of the fluorocarbon segment and a constant length of the hydrocarbon segment, viz. FnH11SH (*n* = 6, 8, and 10) was studied using XPS, IRRAS, synchrotron-based HRXPS and NEXAFS spectroscopy. These FnH11SH SAMs were found to be highly ordered and densely packed, and hence able to protect the GaAs substrate from oxidation. This protection is more effective for the FnH11SH film with the longer fluorocarbon segment due to its better film quality. The packing density of these FnH11SH films was governed by the bulky fluorocarbon segments typical of helical conformation, with the average molecular spacing of ~5.7 Å, close to the van der Waals diameter of this segment. The packing density exhibited a slight decrease with decreasing length of the fluorocarbon segment, but this tendency did not correlate with the observed change of the average inclination of these moieties. Thus, similar to the FnH11SH/Au system, the observed change was also mainly associated with a partial deterioration of the orientational order in the fluorocarbon part of the FnH11SH/GaAs SAMs.

In contrast to the fluorocarbon parts, the hydrocarbon segments in FnH11SH/GaAs exhibit similar orientation. The average tilt angles (~39°) of these segments are close to the optimum one (~27 – 35°) determined by the bending potential for AT SAMs on GaAs; this suggests, once more, the predominant role of this potential in determining the orientation of the hydrocarbon segments in substituted AT SAMs on GaAs. The slightly higher values of the average tilt angles on GaAs as compared to Au suggest that the conformation of the hydrocarbon chains in the FnH11SH SAMs is distorted to some extent as compared to the *all trans* form.

Chapter 8: SAM of Non-substituted Alkaneselenolate on GaAs (001)

So far, the most popular headgroup for the preparation of SAMs on metals and semiconductors, in particular GaAs, is thiol, which provides a sufficient strong and stable bonding to the respective surfaces.[6,34] A prospective alternative of the commonly used thiol is selenol, since the chemical properties of sulfur and selenium are quite similar. Both elements have the same valence electron configurations and are neighbors in the VIB column of the periodic table. However, despite these similarities, only limilted work has so far been done on selenol-derived SAMs, and only on metal substrates;[24,25,81-83,120,171-180] these SAMs can be fabricated from the precursors of both selenol[120,171,175-177,179] and diselenide,[24,25,81-83,171-174,177,178,180] with the film quality in some cases superior than the respective thiol analogue.[83]

The Se-based precursors bond to the metal, commonly Au and Ag, substrate through one selenolate bond (metal−Se−C). Compared with the conventional thiolate bond (metal−S−C), this selenolate bond is considered to be stronger and weaker in the case of Au and Ag, respectively.[81] In addition to the strength of the selenolate bond, it has been proven that the bending potential of the selenolate bond mimics that of the thiolate bond; and this potential is the deciding factor in the balance of structural building forces in alkaneselenolate SAMs on metal (Au and Ag) substrates.[24,25]

In contrast to the metal substrates, till now, only thiol-based precursors have been used for molecular assembly on GaAs substrate.[33,55,58,59] Accordingly, instead of the exclusively used thiol, one selenol-based diselenide ($C_{16}H_{33}SeSeH_{33}C_{16}$, denoted as C16Se with its molecular structure shown in Scheme 1.3), the type of which commonly used for growing selenolate SAMs on metals, has been used for molecular assembly on the GaAs (001) substrate. The structure of this non-substituted alkaneselenolate SAM has been studied in detail mainly by synchrotron-based HRXPS and NEXAFS spectroscopy. Both techniques are highly sensitive and chemically specific. They provide complementary information on chemical identity of the C16Se film and the C16Se/GaAs interface as well as give an insight into the film structure.

8.1 Results

8.1.1 HRXPS

The As 3d and Ga 3d HRXPS spectra of C16Se and C16SH (hexadecanethiol, denoted as C16SH in this chapter) SAMs on GaAs (001) are presented in Figure 8.1 and 8.2, respectively; the spectra of C16SH SAM were included for comparison because of its comparable molecular chain length with C16Se in the SAM fashion. These spectra were acquired at photon energies (PEs) of 580 eV and 350 eV, while the latter photon energy (PE) is chosen to achieve a higher surface sensitivity, since the corresponding smaller effective sample depth ($d \approx 3\lambda$, ~35 Å)[70] ensures a larger spectral weight for the contributions from the topmost layers. Both the As 3d and Ga 3d spectra can be tentatively decomposed like ODT SAM, as described in chapter 4.

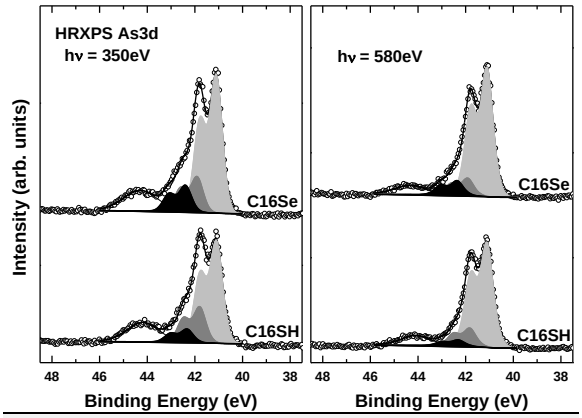

Figure 8.1: As 3d HRXPS spectra of C16Se and C16SH SAMs on GaAs (001). The spectra were acquired at photon energies of 350 (left) and 580 eV (right), respectively. The spectra are decomposed into several doublets related to individual chemical species: Light gray: stoichiometric GaAs; dark gray: elementary As; black: Se-As. The shoulders at the higher binding energy side of the shadowed doublets correspond to As oxides. The assignments were performed in accordance with refs 44, 55, 58.

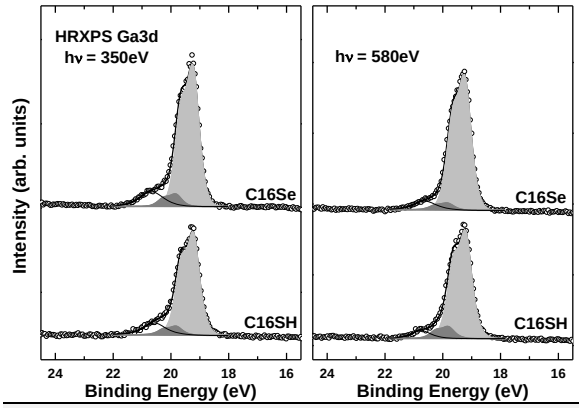

Figure 8.2: Ga 3d HRXPS spectra of C16Se and C16SH SAMs on GaAs (001). The spectra were acquired at photon energies of 350 (left) and 580 eV (right), respectively. The spectra are decomposed into several doublets related to individual chemical species: Light gray: stoichiometric GaAs; dark gray: Ga oxide or surface Ga 3d component. The shoulders at the higher binding energy side of the shadowed doublets correspond to Ga oxides. The assignments were performed in accordance with refs 44, 55, 58.

In Figure 8.1, The As 3d spectra of these two SAMs taken at different PEs are dominated by peaks related to the stoichiometric GaAs (light gray) and elemental As (gray), weak oxidation related features are observed, in particular in the spectra taken at lower PE (350 eV). Like C16SH SAM, one black doublet at ~42.35 eV is observed for the C16Se SAM; this doublet is assigned to the species related to the anchoring group, namely Se-As. This suggests that C16Se molecules predominantly bond to the As atoms of the GaAs substrate, the predominant bonding to As atoms were also observed in alkanethiolate SAMs on GaAs.[44,55,58] In addition, the spectra proportion related to peaks for As-Se species, elemental As, and As oxides increases with decreasing kinetic energy of the photoelectrons, corresponding to the

decreasing sampling depth, which indicates that all these components are located at the near surface region (i.e., at the SAM-GaAs interface).

Similarly, the Ga3d spectra of C16Se and C16SH SAMs acquired at different PEs in Figure 8.2 are dominated by peaks related to the stoichiometric GaAs (light gray), while weak oxidation related features are observed, especially in the spectra acquired at lower PE. Despite the decomposition of the Ga3d spectra does not require an introduction of an additional (with respect to the bulk GaAs component) doublet related to the Ga-Se species, the Ga-Se bonding can not be excluded due to an ambiguity of the spectra fitting in the relevant BE region.

As clearly seen, both the As 3d and Ga 3d spectra of C16Se SAM exhibit weak oxidation related feature, the extent of which is also comparable to that of C16SH monolayer; this suggests the good quality as well as the effective protection property for C16Se SAM.

The formation of contamination-free C16Se SAM was demonstrated in the Se 3d and C 1s HRXPS spectra (spectra of C16SH were included for comparison) in Figure 8.3a and b, respectively, along with the corresponding fits. The results of fitting and a quantitative analysis of these spectra are provided in Table 8.1. The Se 3d spectra of C16Se SAM exhibits only one single doublet, with its BE position (~54.5 eV) distinctly different from that for the bulk diselenide (~55.3 eV);[178] this suggests: upon the adsorption of C16SeSeC16 on GaAs, the covalent Se-Se bonds are cleaved through an oxidative addition mechanism, and selenolate-GaAs bonds are formed.[81,82] Note the BE value is somewhat higher than the analogous one for alkaneselenolate SAMs on metal substrates (54.5 eV versus 54.15 eV),[81] which is caused by the photoscreening effect in the case of metal; the same effect also occurs in the thiolate monolayers on metal and GaAs substrates, resulting the lower BE position (S $2p_{3/2}$) of the S 2p emission in the case of metal.[44] The fwhm value of the $Se3d_{5/2}$ and

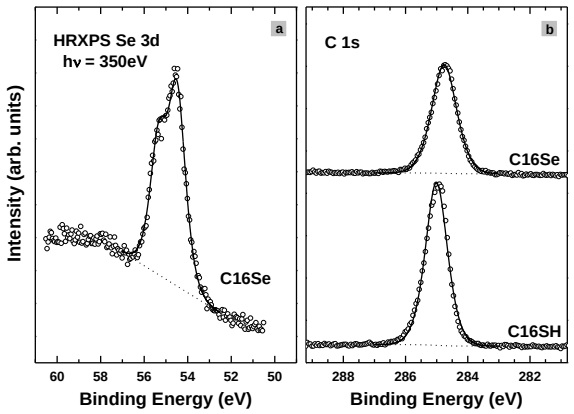

Figure 8.3: Se 3d (a) and C 1s (b) HRXPS spectra of C16Se SAM on GaAs(001). The spectra were acquired at a photon energy of 350 eV. In (b), the C 1s spectra of C16SH SAM on GaAs(001) is included for comparison.

Table 8.1. Binding Energy Positions (eV) and fwhm's (eV; in brackets) of the Photoemission Peaks for C16Se and C16SH SAMs on GaAs (001)

	C16Se	C16SH
C 1s	284.76	285.01
hν = 350 eV	(0.94)	(0.83)
Se 3d or S 2p	54.5	162.44
hν = 350 eV	(0.92)	(0.88)

$Se3d_{3/2}$ peaks is 0.92 eV, which is larger than the analogous ones for alkaneselenolate SAMs Au (~0.74eV) and Ag (~0.51eV) substrates;[81,82] taking into account that the fwhm value is a fingerprint of the homogeneity of the adsorption sites for the selenium head groups, these values suggest the increasing homogeneity of the binding sites for alkaneselenolate SAMs on different substrates, in a sequence of GaAs(001), Au(111), and Ag(111).

The C 1s HRXPS spectra of C16Se and C16SH SAMs both exhibit one single emission peak, with no trace of contamination detected. The peak for C16Se SAM is broader as compared to that for C16SH SAM (0.94eV versus 0.83eV), suggesting the less homogeneity for the former film. In addition, the intensity of the C 1s peak for C16Se SAM is lower as compared to C16SH SAM. Considering these two SAMs have nearly the same molecular chain length in the SAM fashion, the lower intensity for the C16Se monolayer suggests its looser packing as compared to C16SH SAM.

The looser packing of C16Se SAM is further supported by the effective thickness results, which were calculated using equation (5–4) by evaluating the intensity ratios of the C 1s and As 3d emissions, and a high quality ODT SAM with a thickness of 23.8 Å[34] was selected as a reference model. The obtained thickness values are 15.7 Å and 21.2 Å for C16Se and C16SH SAMs, respectively.

8.1.2 NEXAFS spectroscopy

Carbon *K*-edge NEXAFS spectra of C16Se SAM acquired at X-ray incident angles of 90°, 55°, and 20° are presented in Figure 8.4, along with the difference between the 90° and 20° spectra for the C16Se and C16SH SAMs. The spectra exhibit a C1s absorption edge related to C1s → continuum excitations and all characteristic absorption resonances of extended alkyl chains in *all trans* conformation, namely a sharp resonance at ~287.8 eV and two broader resonances at ~293.4 eV and ~301.6 eV. The former resonance, denoted as R^*, is attributed to mixed valence Rydberg states[72,104] with a dominance of Rydberg states,[105,106] while the latter two resonances are commonly related to valence, antibonding C-C σ^* and C-C´ σ^* orbitals.[72,107] The molecular orbitals (plane type) related to

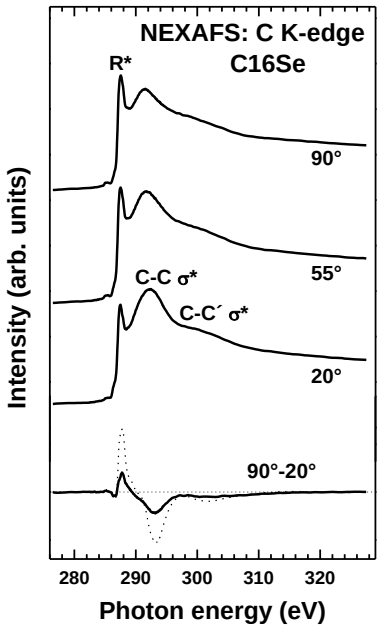

Figure 8.4: Carbon K-edge NEXAFS spectra of C16Se/GaAs SAM acquired at X-ray incident angles of 90°, 55°, and 20°, along with the difference between the 90° and 20° spectra. For comparison, the analogous difference spectrum of C16SH/GaAs is also given by the dotted line. The characteristic absorption resonances are indicated.

the R^* resonance are oriented perpendicular to the alkyl chains,[11,107,108] whereas the TDM of the orbitals (vector type) corresponding to the C-C σ^* and C-C´ σ^* resonances are directed along the chain axis.[108] Thus, the orientation of these orbitals unequivocally determine the orientation of the alkyl chains in the SAMs.

The spectra exhibit pronounced dependence of the absorption resonance intensity on the incidence angle of X-ray, suggesting high orientation order in C16Se SAM. Considering the TDM directions of the R^*, C-C σ^* and C-C´ σ^* orbitals, the positive peak at the position of R^* resonance and the negative peaks at the positions of C-C σ^* and C-C´ σ^* resonances shown in the difference spectra indicate an upright orientation of the alkyl chains in both C16Se and C16SH SAMs. In addition, the peak amplitudes in the difference spectra of C16Se are noticeably smaller than those in the spectra of C16SH, which implies a larger molecular inclination in C16Se SAM, presumably also accompanying the lower orientational order.

Apart from these qualitative considerations, a quantitative analysis can be performed, and the average tilt angles of alkyl chains of C16Se and C16SH SAMs can be determined. For this purpose, the same evaluation method as described in chapter 4 for ODT SAM is applied. The angular dependences of the R^* resonance intensity ratio $I(\theta)/I(20°)$ for the C16Se and C16SH SAMs are presented in Figure 8.5, along with the best theoretical fits. The derived values of the average tilt angles of the alkyl chains in these two SAMs are given at the respective fit curves; they are 18° and 37°, respectively. The accuracy of these values is ± 3–5°, which is just a general accuracy of the NEXAFS experiment and data evaluation procedure.

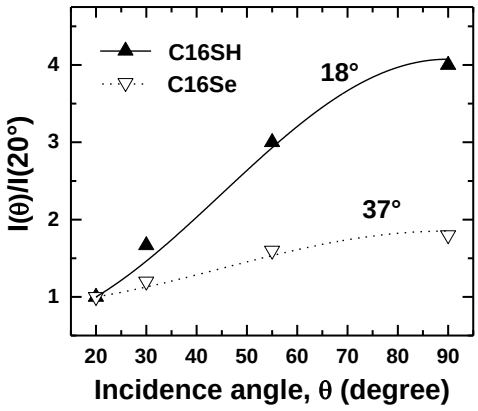

Figure 8.5: The angular dependence of the R^* resonance intensity ratio I(θ)/I(20°) for C16SH/GaAs (up filled triangles) and C16Se/GaAs (down open triangles) along with the best theoretical fits. The derived tilt angles are given at the respective fit curves.

8.1.3 Contact Angle Measurements

The value of static contact angle for C16Se SAM is 102°, which suggests the hydrophobic property of the monolayer surface, and simultaneously indicates the formation of well-ordered C16Se SAM with the CH_3 terminal moiety. In addition, this value is somewhat lower than the analogous ones for C16SH (105°) and ODT (108°) SAMs, suggesting the relatively lower quality of C16Se SAM as compared to these two NSAT SAMs.

8.2 Discussion

The HRXPS, NEXAFS and contact angle data suggest that C16SeSeC16 molecules form contamination-free and well-ordered SAM on GaAs (001) substrate. Like NSAT SAMs, C16Se SAM can protect the GaAs surface effectively from oxidation. The molecules are bound to the substrate via a selenolate bond (GaAs-Se-C), with an upright orientation of the alkyl chain. The selenolate bond is formed after the cleavage of the Se-Se bond, which occurs by an oxidative addition mechanism upon the adsorption, similar to the formation of the thiolate bonds from the disulfide precursors.[81-83] HRXPS results reveal the Se-As as the predominant bond, however, the Se-Ga bond can not be excluded as well; similar case also occurs in the thiolate monolayers on GaAs, i.e. S-As is observed as the predominant bonding mode while the existence of S-Ga bonding can not be ruled out.[59]

The reported binding energy of the thiolate bond on GaAs surface (~2.1 eV) is comparable to that on Au.[46] Here, through analyzing the Se 3d HRXPS spectra, one tentative comparison about the strength of the selenolate and thiolate bond on GaAs can be obtained. In the case of the C16Se/GaAs SAM, the Se 3d doublet (Se $3d_{5/2}$) has 0.35 eV higher BE position than that for alkaneselenolate SAM on Au,[81] whereas the BE position of the S 2p (S $2p_{3/2}$) doublet in ODT/GaAs SAM is 0.5 eV higher than the analogous value in NSAT SAMs on Au.[44] Since a lower BE is indirect indication of a higher extent of the charge transfer, i.e., a stronger bond; it can be assumed that the selenolate bond on GaAs is stronger than the thiolate one.[81] Note, however, this statement is only a tentative one, since the charge transfer is not the only parameter affecting the BE positions of the Se 3d and S 2p doublets. Another parameter, namely the final state effects due to conduction electrons of the substrates (see e.g. Ref [58]) should also be considered, in spite of the semiconductor substrate of GaAs in the present study.

In spite of the effective protection property (Figure 8.1) of C16Se SAM, the quality of this monolayer is lower as compared to that of the C16SH SAM, including its lower coverage, larger molecular tilt, as well as lower orientational order. The observed lower quality is attributed to the difficulty in preparing selenolate SAMs, which is even difficult on Au substrate,[81] and certainly a more complex task on such a substrate as GaAs.

Summary of chapter 8

Instead of the frequently used thiol molecules, a representative selenol-based precursor, namely dihexadecyl diselenide (C16SeSeC16), has been successfully assembled on GaAs (001) surface in the SAM fashion. The molecules bond to the substrate through selenolate-GaAs bond, which is formed after the cleavage of the Se-Se bond upon adsorption. The resulting C16Se SAM was found to be contamination-free and well-ordered, and thus able to protect the GaAs substrate effectively from oxidation.

The structure of the C16Se SAM was compared with the analogous thiolate (C16SH) SAM, the C16Se SAM was found to exhibit lower packing, larger molecular tilt, as well as lower orientational order. These characteristics indicated its lower film quality, primarily due to the difficulty in preparing selenolate SAMs, in particular on the complex GaAs substrate.

Chapter 9: Conclusion

Through careful adjustment and optimization of the preparation conditions, a variety of organothiol precursors, viz. NSATs, specially designed, substituted ATs, such as TPn (n = 0 – 6), BPn (n = 1 – 6) and PFAT, as well as a representative organoselenol molecule have been successfully assembled on the GaAs (001) substrate in the SAM fashion; all these precursors form highly ordered and densely packed SAMs, and thus protect the GaAs surface from oxidation with the extent depending on the film quality. The structure and organization of the above monolayers were investigated in detail by a combination of complementary advanced surface characterization techniques, such as XPS, synchrotron-based HRXPS, NEXAFS spectroscopy, and IRRAS. The aim was to understand the molecular organization in terms of the structure-building interactions, which is essential for application-relevant design of the SAM systems.

Firstly, as a starting point for this thesis work, the most commonly used ODT SAM was prepared on GaAs (001) using the method reported by D. L. Allara et al.,[34] and characterized by a full set of the surface analysis techniques. Its quality was found to be comparable with the best reported one,[34,33] which was essential to perform the further work on molecular assembly on this particular semiconductor substrate. Afterwards, through comparing the structure of the NSAT SAMs with different chain lengths, a pronounced chain length effect, existing also for all other studied SAMs on GaAs (001), was elucidated, viz. the quality of the SAM deteriorates with decreasing length of the molecular chain, which makes the protection of the GaAs substrate less effective, resulting in its partial oxidation.

Secondly, using series of terphenyl- and methyl-terminated biphenyl-substituted AT (TPn and BPn) SAMs, we demonstrated the existence of a bending potential at the headgroup-substrate interface in the AT/GaAs(001) system with a preferable GaAs–S–C angle of ~104°, which is similar to the analogous value for the AT SAMs on Au (111). In the case of TPn and BPn SAMs, this potential plays the dominant role in the balance of the structure-building interactions, mediating the odd-even variation of the molecular orientation and packing density. Therefore, bending potential should always be taken into account for design of future, functional SAMs on technologically important type of semiconductor substrates such as GaAs. For BPn SAMs, in addition to the predominant effect of the bending potential, chain

length effect was also of importance, resulting in relatively poor film quality in the case of the short alkyl linker, such as BP1 and BP2 monolayers.

Thirdly, a series of SAMs formed on Au (111) by PFAT molecules with a variable length of the fluorocarbon segment and a constant length of the hydrocarbon segment, viz. FnH11SH (n = 6, 8, and 10) was studied using XPS, IRRAS, as well as synchrotron-based HRXPS, and NEXAFS spectroscopy. Independent of n, these segments were found to have helical and *all trans* planar conformations, respectively, typical of such entities. The packing density was governed by the bulkier fluorocarbon segments, with the average molecular spacing of 5.7-5.8 Å, close to the van der Waals diameter of these segments. A slight decrease in the packing density was observed with decreasing length of the fluorocarbon segments, which correlated with the increasing average inclination of these segments at going from the F10H11SH to F6H11SH monolayers. The observed change in the inclination was however much stronger than the variation of the packing density, which led us to the assumption that this change was mostly associated with a partial deterioration of the orientational order in the fluorocarbon part of the FnH11SH SAMs. The conformational order of the fluorocarbon segments was mostly persistent through the FnH11SH series, contributing only slightly to the observed variation of the segment inclination.

Whereas the orientational order in the fluorocarbon part of the FnH11SH SAMs varied with varying n and a slight variation of the conformational order could be assumed, the orientation and conformation of the hydrocarbon segments was found to be independent of this parameter. Both tilt and twist angles of the hydrocarbon segments are close to the analogous parameters for the non-substituted AT SAMs on Au (111), which was explained by the effect of the bending potential, predefining the orientation of these segments. The energy contribution associated with this potential is obviously large enough to keep the preferable orientation of the hydrocarbon segments even though they are separated beyond the equilibrium spacing.

The above FnH11SH SAMs on Au served as a reference system for the analogous films on GaAs (001). The latter films were found to be highly ordered and densely packed, and hence able to protect the GaAs surface from the oxidation. This protection was more effective for the FnH11SH film with the longer fluorocarbon segment due to its better quality, in particular in terms of the high orientational order. Similar to the Au substrate, the packing density of the PFAT films on GaAs was governed by the bulky fluorocarbon segments, which had typical helical conformation. The packing density exhibited however, a slight decrease with

decreasing length of the fluorocarbon segment, but this tendency did not correlate with the observed change of the average inclination of these moieties. Thus, similar to the FnH11SH/Au system, the observed change was also mainly associated with a partial deterioration of the orientational order in the fluorocarbon part of the FnH11SH/GaAs SAMs.

In contrast to the fluorocarbon parts, the hydrocarbon segments in FnH11SH/GaAs exhibited similar orientation. The average tilt angles (~39°) of these segments were close to the optimum one (~27 – 35°) determined by the bending potential for AT SAMs on GaAs; this suggests, once more, the predominant role of this potential in determining the orientation of the hydrocarbon segments in substituted AT SAMs on GaAs. The slightly higher values of the average tilt angles on GaAs as compared to Au suggest that the conformation of the hydrocarbon chains in the FnH11SH SAMs was distorted to some extent as compared to the *all trans* form.

Finally, instead of the most frequently used thiol molecules, a representative selenol-based precursor, namely dihexadecyl diselenide (C16Se), was assembled on GaAs (001) in the SAM fashion. Compared with the analogous thiolate monolayer (C16SH/GaAs), the C16Se SAM exhibited lower film quality, in terms of the packing density and orientational order. The poor film quality is attributed to the general difficulty in preparation of selenolate SAMs, which is a particular complex task for such a substrate as GaAs.

To sum up, after unraveling the structure of the NSAT monolayers and the specially designed SAMs, some basic structure-building factors for the molecular assembly on the GaAs (001) substrate such as the bending potential and the chain length effect were derived and studied in detail. The understanding of these factors can help one to design functional SAMs on this technologically important semiconductor substrate, opening an avenue for a variety of useful applications.

Bibliography

(1) Ulman, A. *An Introduction to Ultrathin Organic Films: Langmuir-Blodgett to Self-Assembly*; Academic Press: New York, 1991.

(2) Ulman, A. Formation and Structure of Self-Assembled Monolayers. *Chem. Rev*. **1996**, *96*, 1533-1554.

(3) Ulman, A. (Ed.) *Thin Films: Self-Assembled Monolayers of Thiols*; Academic Press: San Diego, CA, 1998.

(4) Schreiber, F. Structure and Growth of Self-Assembling Monolayers. *Prog. Surf. Sci.* **2000**, *65*, 151-256.

(5) Schreiber, F. Self-Assembled Monolayers: from 'Simple' Model Systems to Biofunctionalized Interfaces. *J. Phys.: Condens. Matter*. **2004**, *16*, R881-R900.

(6) Love, J. C.; Estroff, L. A.; Kriebel, J. K.; Nuzzo, R. G.; Whitesides, G. M. Self-Assembled Monolayers of Thiolates on Metals as a Form of Nanotechnology. *Chem. Rev.* **2005**, *105*, 1103-1169.

(7) Laibinis, P. E.; Whitesides, G. M.; Allara, D. L.; Tao, Y. T.; Parikh, A. N.; Nuzzo, R. G. Comparison of the Structures and Wetting Properties of Self-Assembled Monolayers of N-Alkanethiols on the Coinage Metal Surfaces, Cu, Ag, Au. *J. Am. Chem. Soc*. **1991**, *113*, 7152-7167.

(8) Sellers, H.; Ulman, A.; Shnidman, Y.; Eilers, J. E. Structure and Binding of Alkanethiolates on Gold and Silver Surfaces - Implications for Self-Assembled Monolayers. *J. Am. Chem. Soc*. **1993**, *115*, 9389-9401.

(9) Fenter, P.; Eisenberger, P.; Li, J.; Camillone III, N.; Bernasek, S.; Scoles, G.; Ramanarayanan, T. A.; Liang, K. S. Structure of $CH_3(CH_2)_{17}SH$ Self-Assembled on the Ag (111) Surface: An Incommensurate Monolayer. *Langmuir* **1991**, *7*, 2013–2016.

(10) Nuzzo, R. G.; Dubois, L. H.; Allara, D. L. Fundamental-Studies of Microscopic Wetting on Organic-Surfaces. 1. Formation and Structural Characterization of a Self-Consistent Series of Polyfunctional Organic Monolayers. *J. Am. Chem. Soc*. **1990**, *112*, 558-569.

(11) Hähner, G.; Kinzler, M.; Thümmler, C.; Wöll, C.; Grunze, M. Structure of Self-Organizing Organic Films - a Near Edge X-Ray Absorption Fine-Structure Investigation of Thiol Layers Adsorbed on Gold. *J. Vac. Sci. Technol. A*. **1992**, *10*, 2758-2763.

(12) Fenter, P.; Eisenberger, P.; Liang, K. S. Chain-Length Dependence of the Structures and Phases of $CH_3(CH_2)_{n-1}SH$ Self-Assembled on Au(111). *Phys. Rev. Lett*. **1993**, *70*, 2447-2450.

(13) Fenter, P.; Eberhardt, A.; Eisenberger, P. Self-Assembly of n-Alkyl Thiols as Disulfides on Au(111). *Science* **1994**, *266*, 1216-1218.

(14) Ulman, A.; Eilers, J. E.; Tillman, N. Packing and Molecular-Orientation of Alkanethiol Monolayers on Gold Surfaces. *Langmuir* **1989**, *5*, 1147-1152.

(15) Lee, S.; Puck, A.; Graupe, M.; Colorado, R.; Shon, Y. S.; Lee, T. R.; Perry, S. S. Structure, Wettability, and Frictional Properties of Phenyl-Terminated Self-Assembled Monolayers on Gold. *Langmuir* **2001**, *17*, 7364.

(16) Zharnikov, M.; Frey, S.; Rong, H.; Yang, Y. J.; Heister, K.; Buck, M.; Grunze, M. The Effect of Sulfur-Metal Bonding on the Structure of Self-Assembled Monolayers. *Phys. Chem. Chem. Phys.* **2000**, *2*, 3359-3362.

(17) Rong, H. T.; Frey, S.; Yang, Y. J.; Zharnikov, M.; Buck, M.; Wühn, M.; Wöll, C.; Helmchen, G. On the Importance of the Headgroup Substrate Bond in Thiol Monolayers: A Study of Biphenyl-Based Thiols on Gold and Silver. *Langmuir* **2001**, *17*, 1582-1593.

(18) Heister, K.; Rong, H. T.; Buck, M.; Zharnikov, M.; Grunze, M.; Johansson, L. S. O. Odd-Even Effects at the S-Metal Interface and in the Aromatic Matrix in Biphenyl-Substituted Alkanethiol Self-Assembled Monolayers. *J. Phys. Chem. B* **2001**, *105*, 6888-6894.

(19) Azzam, W.; Fuxen, C.; Birkner, A.; Rong, H. T.; Buck, M.; Wöll, C. Pronounced Odd-Even Changes in the Molecular Arrangement and Packing Density of Biphenyl-Based Thiol SAMs: A Combined STM and LEED Study. *Langmuir* **2003**, *19*, 4958-4968.

(20) Cyganik, P.; Buck, M.; Azzam, W.; Wöll, C. Self-Assembled Monolayers of ω-Biphenylalkanethiols on Au(111): Influence of Spacer Chain on Molecular Packing. *J. Phys. Chem. B* **2004**, *108*, 4989-4996.

(21) Shaporenko, A.; Brunnbauer, M.; Terfort, A.; Grunze, M.; Zharnikov, M. Structural Forces in Self-Assembled Monolayers: Terphenyl-Substituted Alkanethiols on Noble Metal Substrates. *J. Phys. Chem. B* **2004**, *108*, 14462-14469.

(22) Shaporenko, A.; Brunnbauer, M.; Terfort, A.; Johansson, L. S. O.; Grunze, M.; Zharnikov, M. Odd-Even Effects In Photoemission from Terphenyl-Substituted Alkanethiolate Self-Assembled Monolayers. *Langmuir* **2005**, *21*, 4370-4375.

(23) Azzam, W.; Bashir, A.; Terfort, A.; Strunskus, T.; Wöll, C. Combined STM and FTIR Characterization of Terphenylalkanethiol Monolayers on Au (111): Effect of Alkyl Chain Length and Deposition Temperature. *Langmuir* **2006**, *22*, 3647-3655.

(24) Shaporenko, A.; Müller, J.; Weidner, T.; Terfort, A.; Zharnikov, M. Balance of Structure-Building Forces in Selenium-Based Self-Assembled Monolayers. *J. Am. Chem. Soc.* **2007**, *129*, 2232-2233.

(25) Weidner, T.; Shaporenko, A.; Müller, J.; Schmid, M.; Cyganik, P.; Terfort, A.; Zharnikov, M. Effect of the Bending Potential on Molecular Arrangement in Alkaneselenolate Self-Assembled Monolayers. *J. Phys. Chem. C* **2008**, *112*, 12495-12506.

(26) Maoz, R.; Sagiv, J. On the Formation and Structure of Self-Assembling Monolayers. I. A Comparative atr-Wettability Study of Langmuir–Blodgett and Adsorbed Films on Flat Substrates and Glass Microbeads. *J. Colloid Interface Sci.* **1984**, *100*, 465-496.

(27) Stewart, M. P.; Maya, F.; Kosynkin, D. V.; Dirk, S. M.; Stapleton, J. J.; McGuiness, C. L.; Allara, D. L.; Tour, J. M. Direct Covalent Grafting of Conjugated Molecules onto Si, GaAs, and Pd Surfaces from Aryldiazonium Salts. *J. Am. Chem. Soc.* **2004**, *126*, 370-378.

(28) Linford, M. R.; Chidsey, C. E. D. Alkyl Monolayers Covalently Bonded to Silicon Surfaces. *J. Am. Chem. Soc.* **1993**, *115*, 12631-12632.

(29) Buriak, J. M. Organometallic Chemistry on Silicon and Germanium Surfaces. *Chem. Rev.* **2002**, *102*, 1271-1308.

(30) He, J. L.; Lu, Z. H.; Mitchell, S. A.; Wayner, D. D. M. Self-Assembly of Alkyl Monolayers on Ge(111)[1a] *J. Am. Chem. Soc.* **1998**, *120*, 2660-2661.

(31) Kosuri, M. R.; Cone, R.; Li, Q. M.; Han, S. M.; Bunker, B. C.; Mayer, T. M. Adsorption Kinetics of 1-Alkanethiols on Hydrogenated Ge(111). *Langmuir* **2004**, *20*, 835-840.

(32) Han, S. M.; Ashurst, W. R.; Carraro, C.; Maboudian, R. Formation of Alkanethiol Monolayer on Ge(111). *J. Am. Chem. Soc.* **2001**, *123*, 2422-2425.

(33) McGuiness, C. L.; Diehl, G. A.; Blasini, D.; Smilgies, D. M.; Zhu, M.; Samarth, N.; Weidner, T.; Ballav, N.; Zharnikov, M.; Allara, D. L. Molecular Self-Assembly at Bare Semiconductor Surfaces: Cooperative Substrate Molecule Effects in Octadecanethiolate Monolayer Assemblies on GaAs(111), (110), and (100). *ACS Nano* **2010**, *4*, 3447-3465.

(34) McGuiness, C. L.; Shaporenko, A.; Mars, C. K.; Uppili, S.; Zharnikov, M.; Allara, D. L. Molecular Self-Assembly at Bare Semiconductor Surfaces: Preparation and Characterization of Highly Organized Octadecanethiolate Monolayers on GaAs(001). *J. Am. Chem. Soc*. **2006**, *128*, 5231-5243.

(35) Gu, Y.; Lin, Z.; Butera, R. A.; Smentkowski, V. S.; Waldeck, D. H. Preparation of Self-Assembled Monolayers on InP. *Langmuir* **1995**, *11*, 1849-1851.

(36) Yamamoto, H.; Butera, R. A.; Gu, Y.; Waldeck, D. H. Characterization of the Surface to Thiol Bonding in Self-Assembled Monolayer Films of $C_{12}H_{25}SH$ on InP(100) by Angle-Resolved X-ray Photoelectron Spectroscopy. *Langmuir* **1999**, *15*, 8640-8644.

(37) Petrovykh, D. Y.; Smith, J. C.; Clark, T. D.; Stine, R.; Baker, L. A.; Whitman, L. J. Self-Assembled Monolayers of Alkanethiols on InAs. *Langmuir* **2009**, *25*, 12185-12194.

(38) Knoben, W.; Brongersma, S. H.; Crego-Calama, M. Preparation and Characterization of Octadecanethiol Self-Assembled Monolayers on Indium Arsenide (100). *J. Phys. Chem. C* **2009**, *113*, 18331-18340.

(39) Seker, F.; Meeker, K.; Kuech, T. F.; Ellis, A. B. Surface Chemistry of Prototypical Bulk II-VI and III-V Semiconductors and Implications for Chemical Sensing. *Chem. Rev.* **2000**, *100*, 2505–2536.

(40) Lebedev, M. V. Surface Modification of III–V Semiconductors: Chemical Processes and Electronic Properties. *Prog. Surf. Sci.* **2002**, *70*, 153–186.

(41) Luber, S. M.; Adlkofer, K.; Rant, U.; Ulman, A.; Gölzhäuser, A.; Grunze, M.; Schuh, D.; Tanaka, M.; Tornow, M.; Abstreiter, G. Liquid Phase Sensors Based on Chemically Functionalized GaAs/AlGaAs Heterostructures. *Phys. E* **2004**, *21*, 1111-1115.

(42) Gassull, D.; Ulman, A.; Grunze, M.; Tanaka, M. Electrochemical Sensing of Membrane Potential and Enzyme Function Using Gallium Arsenide Electrodes Functionalized with Supported Membranes. *J. Phys. Chem. C* **2008**, *112*, 5736-5741.

(43) Arudra, P.; Nguiffo-Podie, Y.; Frost, E.; Dubowski, J. J. Decomposition of Thimerosal and Dynamics of Thiosalicylic Acid Attachment on GaAs(001) Surface Observed with in Situ Photoluminescence. *J. Phys. Chem. C* **2010**, *114*, 13657-13662.

(44) McGuiness, C. L.; Shaporenko, A.; Zharnikov, M.; Walker, A. V.; Allara, D. L. Molecular Self-Assembly at Bare Semiconductor Surfaces: Investigation of the Chemical and Electronic Properties of the Alkanethiolate-GaAs(001) Interface. *J. Phys. Chem. C* **2007**, *111*, 4226-4234.

(45) McGuiness, C. L.; Blasini, D.; Masejewski, J. P.; Uppili, S.; Cabarcos, O. M.; Smilgies, D.; Allara, D. L. Molecular Self-Assembly at Bare Semiconductor Surfaces: Characterization of a Homologous Series of n-Alkanethiolate Monolayers on GaAs(001). *ACS Nano* **2007**, *1*, 30-49.

(46) Voznyy, O.; Dubowski, J. J. Structure, Bonding Nature, and Binding Energy of Alkanethiolate on As-Rich GaAs (001) Surface: A Density Functional Theory Study. *J. Phys. Chem. B* **2006**, *110*, 23619-23622.

(47) Voznyy, O.; Dubowski, J. J. Structure of Thiol Self-Assembled Monolayers Commensurate with the GaAs (001) Surface. *Langmuir* **2008**, *24*, 13299-13305.

(48) Zhou, C.; Walker, A. V. UV Photooxidation of a Homologous Series of n-Alkanethiolate Monolayers on GaAs(001): A Static SIMS Investigation. *J. Phys. Chem. C* **2008**, *112*, 797-805.

(49) Zhou, C.; Jones, J. C.; Trionfi, A.; Hsu, J. W. P.; Walker, A. V. Electron Beam-Induced Damage of Alkanethiolate Self-Assembled Monolayers Adsorbed on GaAs (001): A Static SIMS Investigation. *J. Phys. Chem. C* **2010**, *114*, 5400–5409.

(50) Aqua, T.; Cohen, H.; Vilan, A.; Naaman, R. Long-Range Substrate Effects on the Stability and Reactivity of Thiolated Self-Assembled Monolayers. *J. Phys. Chem. C* **2007**, *111*, 16313-16318.

(51) Aqua, T.; Cohen, H.; Sinai, O.; Frydman, V.; Bendikov, T.; Krepel, D.; Hod, O.; Kronik, L.; Naaman, R. Role of Backbone Charge Rearrangement in the Bond-Dipole and Work Function of Molecular Monolayers. *J. Phys. Chem. C* **2011**, *115*, 24888–24892.

(52) Wu, L.; Camacho-Alanis, F.; Castaneda, H.; Zangari, G.; Swami, N. Electrochemical Impedance Spectroscopy of Carboxylic-acid Terminal Alkanethiol Self Assembled Monolayers on GaAs Substrates. *Electrochimica Acta* **2010**, *55*, 8758-8765.

(53) Duplan, V.; Miron, Y.; Frost, E.; Grandbois, M.; Dubowski, J. J. Specific Immobilization of Influenza A Virus on GaAs (001) Surface. *J. Biomed. Opt*. **2009**, *14*, 0540421-6.

(54) Krapchetov, D. A.; Ma, H.; Jen, A. K. Y.; Fischer, D. A.; Loo, Y. L. Solvent-Dependent Assembly of Terphenyl- and Quaterphenyldithiol on Gold and Gallium Arsenide. *Langmuir* **2005**, *21*, 5887-5893.

(55) Shaporenko, A.; Adlkofer, K.; Johansson, L. S. O.; Tanaka, M.; Zharnikov, M. Functionalization of GaAs Surfaces with Aromatic Self-Assembled Monolayers: A Synchrotron-Based Spectroscopic Study. *Langmuir* **2003**, *19*, 4992-4998.

(56) Adlkofer, K.; Shaporenko, A.; Zharnikov, M.; Grunze, M.; Ulman, A.; Tanaka, M. Chemical Engineering of Gallium Arsenide Surfaces with 4'-Methyl-4-mercaptobiphenyl and 4'-Hydroxy-4-mercaptobiphenyl Monolayers. *J. Phys. Chem. B* **2003**, *107*, 11737-11741.

(57) Adlkofer, K.; Eck, W.; Grunze, M.; Tanaka, M. Surface Engineering of Gallium Arsenide with 4-Mercaptobiphenyl Monolayers. *J. Phys. Chem. B* **2003**, *107*, 587-591.

(58) Shaporenko, A.; Adlkofer, K.; Johansson, L. S. O.; Ulman, A.; Grunze, M.; Tanaka, M.; Zharnikov, M. Spectroscopic Characterization of 4'-Substituted Aromatic Self-Assembled Monolayers on GaAs(100) Surface. *J. Phys. Chem. B* **2004**, *108*, 17964-17972.

(59) Lu, H.; Terfort, A.; Zharnikov, M. Bending Potential as an Important Factor for the Structure of Monomolecular Thiolate Layers on GaAs Substrates. *J. Phys. Chem. Lett.* **2013**, *4*, 2217-2222.

(60) Zhou, C.; Trionfi, A.; Jones, J. C.; Hsu, J. W. P.; Walker, A. V. Comparison of Chemical Lithography Using Alkanethiolate Self-Assembled Monolayers on GaAs (001) and Au. *Langmuir* **2010**, 26, 4523-4528.

(61) Chesneau, F.; Zhao, J.; Shen, C.; Buck, M.; Zharnikov, M. Adsorption of Long-Chain Alkanethiols on Au(111) - A Look from the Substrate by High Resolution X-Ray Photoelectron Spectroscopy. *J. Phys. Chem. C* **2010**, *114*, 7112–7119.

(62) Brandrup, J.; Immergut, E. H. *Polymer handbook. 3rd ed.*; John Wiley & sons: New York, 1989.

(63) Tamada, K.; Ishida, T.; Knoll, W.; Fukushima, H.; Colorado, Jr., R.; Graupe, M.; Shmakova, O. E.; Lee, T. R. Molecular Packing of Semifluorinated Alkanethiol Self-Assembled Monolayers on Gold: Influence of Alkyl Spacer Length. *Langmuir* **2001**, *17*, 1913-1921.

(64) Bunn, C. W.; Howells, E. R. Structures of Molecules and Crystals of Fluoro-Carbons. *Nature* **1954**, *174*, 549-551.

(65) Alves, C. A.; Porter, M. D. Atomic-Force Microscopic Characterization of a Fluorinated Alkanethiolate Monolayer at Gold and Correlations to Electrochemical and Infrared Reflection Spectroscopic Structural Descriptions. *Langmuir* **1993**, *9*, 3507-3512.

(66) Tsao, M. W.; Hoffmann, C. L.; Rabolt, J. F.; Johnson, H. E.; Castner, D. G.; Erdelen, C.; Ringsdorf, H. Studies of Molecular Orientation and Order in Self-Assembled Semifluorinated n-Alkanethiols: Single and Dual Component Mixtures. *Langmuir* **1997**, *13*, 4317-4322.

(67) Ratner, D. B.; Castner, D. G. *Surface Analysis – The Principal Techniques, 2nd Edi.*; Vickerman, J. C., Ed.; Wiley: Chichester, 2009.

(68) Scofield, J. H. Hartree-Slater Subshell Photoionization Cross-Sections at 1254 and 1487 eV. *J. Electron Spectrosc. Relat. Phenom.* **1976**, *8*, 129-137.

(69) Jablonski, A.; Powell, C. J. The Electron Attenuation Length Revisited. *Surf. Sci. Rep.* **2002**, *47*, 33-91.

(70) Lamont C. L. A. and Wilkes, J. Attenuation Length of Electrons in Self-Assembled Monolayers of *n*-Alkanethiols on Gold**.** *Langmuir* **1999**, *15*, 2037-2042.

(71) Bain, C. D.; Whitesides, G. M. Attenuation Lengths of Photoelectrons in Hydrocarbon Films. *J. Phys. Chem.* **1989**, *93*, 1670-1673.

(72) Stöhr, J. *NEXAFS spectroscopy*; Springer-Verlag: Berlin, 1992.

(73) Watts, B.; Thomsen, L.; Dastoor, P. Methods in Carbon K-edge NEXAFS: Experiment and Analysis. *J. Electr. Spectr. Rel. Phenom.* **2006**, *151*, 105-120.

(74) Hähner, G. Near Edge X-ray Absorption Fine Structure Spectroscopy as a Tool to Probe Electronic and Structural Properties of Thin Organic Films and Liquids. *Chem. Soc. Rev.* **2006**, *35*, 1244-1255.

(75) Tadmor, R. Line Energy and the Relation between Advancing, Receding, and Young Contact Angles. *Langmuir* **2004**, **20**, 7659-7664.

(76) Zharnikov, M. High-Resolution X-Ray Photoelectron Spectroscopy in Studies of Self-Assembled Organic Monolayers. *J. Electr. Spectr. Rel. Phenom.* **2010**, *178-179*, 380-393.

(77) Naud, C.; Calas, P.; Blancou, H.; Commeyras, A. Synthesis of Terminally Perfluorinated Long-Chain Alkanethiols, Sulfides and Disulfides from the Corresponding Halides. *J. Fluor. Chem.* **2000**, *104*, 173-183.

(78) Graupe, M.; Koini, T.; Wang, V. Y.; Nassif, G. M.; Colorado Jr, R.; Villazana, R. J.; H. Dong; Miura, Y. F.; Shmakova, O. E.; Lee, T. R. Terminally Perfluorinated Long-Chain Alkanethiols. *J. Fluor. Chem.* **1999**, *93*, 107-115.

(79) Ballav, N.; Schüpbach, B.; Dethloff, O.; Feulner, P.; Terfort, A.; Zharnikov, M. Direct Probing Molecular Twist and Tilt in Aromatic Self-Assembled Monolayers. *J. Am. Chem. Soc*. **2007**, *129*, 15416-15417.

(80) Lu, H.; Zeysing, D.; Kind, M.; Terfort, A.; Zharnikov, M. Structure of Self-Assembled Monolayers of Partially Fluorinated Alkanethiols with a Fluorocarbon Part of Variable Length on Gold Substrate. *J. Phys. Chem. C* **2013**, *117*, 18967−18979.

(81) Shaporenko, A.; Ulman, A.; Terfort, A.; Zharnikov, M. Self-Assembled Monolayers of Alkaneselenolates on (111) Gold and Silver. *J. Phys. Chem. B* **2005**, *109*, 3898-3906.

(82) Shaporenko, A.; Cyganik, P.; Buck, M.; Ulman, A.; Zharnikov, M. Self-Assembled Monolayers of Semifluorinated Alkaneselenolates on Noble Metal Substrates. *Langmuir* **2005**, *21*, 8204-8213.

(83) Shaporenko, A.; Cyganik, P.; Buck, M.; Terfort, A.; Zharnikov, M. Self-Assembled Monolayers of Aromatic Selenolates on Noble Metal Substrates. *J. Phys. Chem. B* **2005**, *109*, 13630-13638.

(84) Moulder, J. F.; Stickle, W. E.; Sobol, P. E.; Bomben, K. D. *Handbook of X-ray Photoelectron Spectroscopy. A Reference Book of Standard Spectra for Identification and Interpretation of XPS Data*; Chastian, J., Ed.; Perkin-Elmer Corp.: Eden Prairie, 1992.

(85) Band, I. M.; Kharitonov, Y. I.; Trzhaskovskaya, M. B. Photoionization Cross Sections and Photoelectron Angular Distributions for X-ray Line Energies in the Range 0.132−4.509 keV Targets: $1 \leq Z \leq 100$. *At Data Nucl Data Tables*. **1979**, *23*, 443-505.

(86) Goldberg, S. M.; Fadley, C. S.; Kono, S. Photoionization Cross-Sections for Atomic Orbitals with Random and Fixed Spatial Orientation. *J. Electr. Spectr. Rel. Phenom.* **1981**, *21*, 285-363.

(87) Yeh, J. J.; Lindau, I. Atomic Subshell Photoionization Cross Sections and Asymmetry Parameters: $1 \leq Z \leq 103$. *At Data Nucl Data Tables*. **1985**, *32*, 1-155.

(88) Wirde, M.; Gelius, U.; Dunbar, T.; Allara, D. L. Modification of Self-Assembled Monolayers of Alkanethiols on Gold by Ionizing Radiation. *Nucl. Instrum. Meth. B* **1997**, *131*, 245-251.

(89) Jager, B.; Schurmann, H.; Muller, H. U.; Himmel, H. J.; Neumann, M.; Grunze, M.; Wöll, C. X-Ray and Low Energy Electron Induced Damage in Alkanethiolate Monolayers on Au-Substrates. *Z. Phys. Chem*. **1997**, *202*, 263-272.

(90) Heister, K.; Zharnikov, M.; Grunze, M.; Johansson, L. S. O.; Ulman, A. Characterization of X-Ray Induced Damage In Alkanethiolate Monolayers by High-Resolution Photoelectron Spectroscopy. *Langmuir* **2001**, *17*, 8-11.

(91) Zharnikov, M.; Grunze, M. Modification of Thiol-Derived Self-Assembling Monolayers by Electron and X-Ray Irradiation: Scientific and Lithographic Aspects. *J. Vac. Sci. Technol. B* **2002**, *20*, 1793-1807.

(92) Nefedov, A. Wöll, C. Advanced Applications of NEXAFS Spectroscopy for Functionalized Surfaces, in Surface Science Techniques, Bracco, G.; Holst, B. Eds.; *Springer Series in Surface Science* **2013**, *51* 277-306; Springer-Verlag, Berlin, Heidelberg, New York, Tokyo.

(93) Batson, P. E. Carbon-1s Near-Edge-Absorption Fine-Structure in Graphite. *Phys. Rev. B* **1993**, *48*, 2608-2610.

(94) Frisch, M. J.; et al., Gaussian 09, Revision A. 02, Gaussian, Inc., Wallingford, CT, 2009.

(95) Perdew, J. Density-Functional Approximation for the Correlation Energy of the Inhomogeneous Electron Gas. *Phys. Rev. B* **1986**, *33*, 8822–8824.

(96) Becke, A. D. Density-Functional Exchange-Energy Approximation with Correct Asymptotic Behavior. *Phys. Rev. A* **1988**, *38*, 3098–3100.

(97) Weigend, F.; Ahlrichs, R. Balanced Basis Sets of Split Valence, Triple Zeta Valence and Quadruple Zeta Valence Quality for H to Rn: Design and Assessment of Accuracy. *Phys. Chem. Chem. Phys.* **2005**, *7*, 3297–3305.

(98) Lindau, I.; Spicer, W. E. The Probing Depth in Photoemission and Auger-Electron Spectroscopy. *J. Electr. Spectr. Rel. Phenom.* **1974**, *3*, 409-413.

(99) Powell, C. J. Attenuation Lengths of Low-Energy Electrons in Solids. *Surf. Sci*. **1974**, *44*, 29-46.

(100) Heister, K.; Zharnikov, M.; Grunze, M.; Johansson, L. S. O. Adsorption of Alkanethiols and Biphenylthiols on Au and Ag Substrates: A High-Resolution X-Ray Photoelectron Spectroscopy Study. *J. Phys. Chem. B* **2001**, *105*, 4058-4061.

(101) Himmelhaus, M.; Gauss, I.; Buck, M.; Eisert, F.; Wöll, C.; Grunze, M. Adsorption of Docosanethiol from Solution on Polycrystalline Silver Surfaces: an XPS and NEXAFS Study. *J. Electron. Spectrosc*. **1998**, *92*, 139-149.

(102) Zharnikov, M.; Grunze, M. Spectroscopic Characterization of Thiol-Derived Self-Assembled Monolayers. *J. Phys.: Condens. Matter.* **2001**, *13*, 11333-11365.

(103) Heister, K.; Johansson, L. S. O.; Grunze, M.; Zharnikov, M. A Detailed Analysis of the C 1s Photoemission of n-Alkanethiolate Films on Noble Metal Substrates. *Surf. Sci.* **2003**, *529*, 36-46.

(104) Väterlein, P.; Fink, R.; Umbach, E.; Wurth, W. Analysis of the X-Ray Absorption Spectra of Linear Saturated Hydrocarbons Using the X Alpha Scattered-Wave Method. *J. Chem. Phys*. **1998**, *108*, 3313-3120.

(105) Bagus, P. S.; Weiss, K.; Schertel, A.; Wöll, C.; Braun, W.; Hellwig, C.; Jung, C. Identification of Transitions into Rydberg States in the X-Ray Absorption Spectra of Condensed Long-Chain Alkanes. *Chem. Phys. Lett*. **1996**, *248*, 129-135.

(106) Weiss, K.; Bagus, P. S.; Wöll, C. Rydberg Transitions in X-Ray Absorption Spectroscopy of Alkanes: The Importance of Matrix Effects. *J. Chem. Phys*. **1999**, *111*, 6834-6845.

(107) Outka, D. A.; Stohr, J.; Rabe, J. P.; Swalen, J. D. The Orientation of Langmuir-Blodgett Monolayers Using NEXAFS. *J. Chem. Phys*. **1988**, *88*, 4076-4087.

(108) Hähner, G.; Kinzler, M.; Wöll, Ch.; Grunze, M.; Scheller, M. K.; Cederbaum, L. S. Near Edge X-Ray-Absorption Fine-Structure Determination of Alkyl-Chain Orientation - Breakdown of the Building-Block Scheme. *Phys. Rev. Lett*. **1991**, *67*, 851-854.

(109) Porter, M. D.; Bright, T. B.; Allara, D. L.; Chidsey, C. E. D. Spontaneously Organized Molecular Assemblies. 4. Structural Characterization of n-Alkyl Thiol Monolayers on Gold by Optical Ellipsometry, Infrared-Spectroscopy, and Electrochemistry. *J. Am. Chem. Soc*. **1987**, *109*, 3559-3568.

(110) Parikh, A. N.; Allara, D. L. Quantitative Determination of Molecular Structure in Multilayered Thin Films of Biaxial and Lower Symmetry from Photon Spectroscopies. I. Reflection Infrared Vibrational Spectroscopy. *J. Chem. Phys.* **1992**, *96*, 927-945.

(111) Debe, M. K. Extracting Physical Structure Information from Thin Organic Films with Reflection Absorption Infrared Spectroscopy. *J. Appl. Phys*. **1984**, *55*, 3354-3566.

(112) Aspnes, D. E., Studna, A. A. Stability of (100) GaAs surfaces in aqueous solutions. *Appl Phys Lett*. **1985**, *46*, 1071-1073.

(113) Adlkofer, K.; Tanaka, M. Stable Surface Coating of Gallium Arsenide with Octadecylthiol Monolayers. *Langmuir* **2001**, *17*, 4267-4273.

(114) Baum, T.; Ye, S. Formation of Self-Assembled Monolayers of Alkanethiols on GaAs surface with in Situ Surface Activation by Ammonium Hydroxide. *Langmuir* 1999, *15*, 8577-8579.

(115) Scimeca, T.; Muramatsu, Y.; Oshima, M.; Oigawa, H.; Nannichi, Y. Temperature-Dependent Changes on the Sulfur-Passivated GaAs (111)A, (100), and (111)B surfaces. *Phys. Rev. B* **1991**, *44*, 12927-12932.

(116) Ohno, T.; Shiraishi, K. First-Principles Study of Sulfur Passivation of GaAs(001) Surfaces. *Phys. Rev. B* **1990**, *42*, 11194-11197.

(117) Lebedev, M. V.; Mayer, T.; Jaegermann, W. Sulfur Adsorption at GaAs(100) from Solution: Role of the Solvent in Surface Chemistry. *Surf. Sci.* **2003**, *547*, 171-183.

(118) Medvedev, Y. V. Thermodynamic Stability of GaAs Sulfur Passivation. *Appl. Phys. Lett.* **1994**, *64*, 3458-3460.

(119) Spindt, C. J.; Liu, D.; Miyano, K.; Meissner, P. L.; Chiang, T. T.; Kendelewicz, T.; Lindau, I.; Spicer, W. E. Vacuum Ultraviolet Photoelectron Spectroscopy of $(NH_4)_2S$-Treated GaAs (100) Surfaces *Appl. Phys. Lett.* **1989**, *55*, 861-863.

(120) Samant, M. G.; Brown, C. A.; Gordon, J. G. Formation of an Ordered Self-Assembled Monolayer of Docosaneselenol on Gold(111): Structure by Surface X-Ray Diffraction. *Langmuir* **1992**, *8*, 1615–1618.

(121) Cyganik, P.; Buck, M.; Wilton-Ely, J. D. E. T.; Wöll, C. Stress in Self-Assembled Monolayers: ω-Biphenyl Alkane Thiols on Au(111). *J. Phys. Chem. B* **2005**, *109*, 10902-10908.

(122) Chang, C. C.; Citrin, P. H.; Swartz, B. Chemical Preparation of GaAs Surfaces and Their Characterization by Auger Electron and X-ray Photoemission Spectroscopies. *Journal of Vacuum Scienc* **1977**, *14*, 943-952.

(123) Ballav, N.; Schüpbach, B.; Neppl, S.; Feulner, P.; Terfort, A.; Zharnikov, M. Biphenylnitrile-Based Self-Assembled Monolayers on Au(111): Spectroscopic Characterization and Resonant Excitation of the Nitrile Tail Group. *J. Phys. Chem. C* **2010**, *114*, 12719-12727.

(124) Rangan, S.; Gallet, J.-J.; Bournel, F.; Kubsky, S.; Guen, K. Le; Dufour, G.; Rochet, F. Adsorption of Benzonitrile on Si(001)-2×1 at 300 K. *Phys. Rev. B* **2005**, *71*, 1653181-12.

(125) Zharnikov, M.; Küller, A.; Shaporenko, A.; Schmidt, E.; Eck, M. Aromatic Self-Assembled Monolayers on Hydrogenated Silicon. *Langmuir* **2003**, *19*, 4682-4687.

(126) Liu, J.; Schüpbach, B.; Bashir, A.; Shekhah, O.;Nefedov, A.; Kind, M.; Terfort, A.; Wöll C. Structural Characterization of Self-Assembled Monolayers of Pyridine-Terminated Thiolates on Gold. *Phys. Chem. Chem. Phys.* **2010**, *12*, 4459-4472.

(127) Biebuyck, H. A.; Bain, C.D.; Whitesides, G. M. Comparison of Organic Monolayers on Polycrystalline Gold Spontaneously Assembled from Solutions Containing Dialkyl Disulfides or Alkanethiols. *Langmuir* **1994**, *10*, 1825-1831.

(128) Chesneau, F.; Schüpbach, B.; Szelągowska-Kunstman, K.; Ballav, N.; Cyganik, P.; Terfort, A.; Zharnikov, M. Self-Assembled Monolayers of Perfluoroterphenyl-Substituted Alkanethiols: Specific Characteristics and Odd-Even Effects. *Phys. Chem. Chem. Phys.* **2010**, *12*, 12123-12127.

(129) Hamoudi, H.; Döring, K.; Chesneau, F.; Lang, H.; Zharnikov, M. Self-Assembly of Pyridine-Substituted Alkanethiols on Gold: the Electronic Structure Puzzle in the Ortho- and Para-Attachment of Pyridine to the Molecular Chain. *J. Phys. Chem. C* **2012**, *116*, 861–870.

(130) Cyganik, P.; Buck, M.; Strunskus, T.; Shaporenko, A.; Wilton-Ely, J. D. E. T.; Zharnikov, M.; Wöll, C. Competition as a Design Concept: Polymorphism in Self-Assembled Monolayers of Biphenyl-Based Thiols. *J. Am. Chem. Soc.* **2006**, *128*, 13868-13878.

(131) Tao, F.; Bernasek, S. L. Understanding Odd-Even Effects in Organic Self-Assembled Monolayers. *Chem. Rev.* **2007**, *107*, 1408–1453.

(132) However, the packing of ODT/GaAs is similar to that of ODT/Au, which implies the NSAT SAMs on GaAs do not behave totally like those on Ag.

(133) Frey, S.; Stadler, V.; Heister, K.; Eck, W.; Zharnikov, M.; Grunze, M.; Zeysing, B.; Terfort, A. Structure of Thioaromatic Self-Assembled Monolayers on Gold and Silver. *Langmuir* **2001**, *17*, 2408-2415.

(134) Lenk, T. J.; Hallmark, V. M.; Hoffmann, C. L.; Rabolt, J. F.; Castner, D. G.; Erdelen, C.; Ringsdorf, H. Structural Investigation of Molecular-Organization in Self-Assembled Monolayers of a Semifluorinated Amidethiol. *Langmuir* **1994**, *10*, 4610-4617.

(135) Liu, G. Y.; Fenter, P.; Chidsey, C. E. D.; Ogletree, D. F.; Eisenberger, P.; Salmeron, M. An Unexpected Packing of Fluorinated N-Alkane Thiols on Au(111) - a Combined Atomic-Force Microscopy and X-Ray-Diffraction Study. *J. Chem. Phys*. **1994**, *101*, 4301-4306.

(136) Tsao, M.-W.; Rabolt, J. F.; Schönherr, H.; Castner, D. G. Semifluorinated/Hydrogenated Alkylthiol Thin Films: A Comparison Between Disulfides and Thiol Binary Mixtures. *Langmuir* **2000**, *16*, 1734-1743.

(137) Genzer, J.; Sivaniah, E.; Kramer, E. J.; Wang, J.; Xiang, M.; Char, K.; Ober, C. K.; Bubeck, R. A.; Fischer, D. A.; Graupe, M.; Colorado, Jr., R.; Shmakova, O. E.; Lee, T. R. Molecular Orientation of Single and Two-Armed Monodendron Semifluorinated Chains on "Soft" and "Hard" Surfaces Studied Using NEXAFS. *Macromolecules* **2000**, *33*, 6068-6077.

(138) Fukushima, H.; Seki, S.; Nishikawa, T.; Takiguchi, H.; Tamada, K.; Abe, K.; Colorado, Jr., R.; Graupe, M.; Shmakova, O. E.; Lee, T. R. Microstructure, Wettability, and Thermal Stability of Semifluorinated Self-Assembled Monolayers (SAMs) on Gold. *J. Phys. Chem. B* **2000**, *104*, 7417-7423.

(139) Frey, S.; Heister, K.; Zharnikov, M.; Grunze, M.; Tamada, K.; Colorado, Jr., R.; Graupe, M.; Shmakova, O. E.; Lee, T. R. Structure of Self-Assembled Monolayers of Semifluorinated Alkanethiols on Gold and Silver Substrates. *Israel. J. Chem*. **2000**, *40*, 81-97.

(140) Weinstein, R. D.; Moriarty, J.; Cushnie, E.; Colorado, Jr., R.; Lee, T. R.; Patel, M.; Alesi, W. R.; Jennings, G. K. Structure, Wettability, and Electrochemical Barrier Properties of Self-Assembled Monolayers Prepared from Partially Fluorinated Hexadecanethiols. *J. Phys. Chem. B* **2003**, *107*, 11626-11632.

(141) Colorado, Jr., R.; Graupe, M.; Shmakova, O. E.; Villazana, R. J.; Lee, T. R.. Structural Properties of Self-Assembled Monolayers (SAMs) on Gold Generated from Terminally Fluorinated Alkanethiols. In *Interfacial Properties on the Submicron Scale*; J. E. Frommer, R. Overney, Eds.; ACS Symposium Series 781; American Chemical Society: Washington, DC, 2001; pp 276-292.

(142) Colorado, Jr., R.; Lee, T. R. Attenuation Lengths of Photoelectrons in Fluorocarbon Films. *J. Phys. Chem. B* **2003**, *107*, 10216-10220.

(143) Colorado, Jr., R.; Lee, T. R. Wettabilities of Self-Assembled Monolayers on Gold Generated from Progressively Fluorinated Alkanethiols. *Langmuir* **2003**, *19*, 3288-3296.

(144) Alloway, D. M.; Hofmann, M.; Smith, D. L.; Gruhn, N. E.; Graham, A. L.; Colorado, Jr., R.; Wysocki, V. H.; Lee, T. R.; Lee, P. A.; Armstrong, N. R. Interface Dipoles Arising from Self-Assembled Monolayers on Gold: UV-Photoemission Studies of Alkanethiols and Partially Fluorinated Alkanethiols. *J. Phys. Chem. B* **2003**, *107*, 11690-11699.

(145) Yuan, Y. H.; Yam, C. M.; Shmakova, O. E.; Colorado, Jr., R.; Graupe, M.; Fukushima, H.; Moore, H. J.; Lee, T. R. Solution-Phase Desorption of Self-Assembled Monolayers on Gold Derived From Terminally Perfluorinated Alkanethiols. *J. Phys. Chem. C* **2011**, *115*, 19749-19760.

(146) Frey, S.; Heister, K.; Zharnikov, M.; Grunze, M. Modification of Semifluorinated Alkanethiolate Monolayers by Low Energy Electron Irradiation. *Phys. Chem. Chem. Phys*. **2000**, *2*, 1979-1987.

(147) Tamada, K.; Nagasawa, J.; Nakanishi, F.; Abe, K.; Hara, M.; Knoll, W.; Ishida, T.; Fukushima, H.; Miyashita, S.; Usui, T.; Koini, T.; Lee, T. R. Structure of SAMs Generated from Functionalized Thiols on Gold. *Thin Solid Films* **1998**, *329*, 150-155.

(148) Ahn, H.; Zharnikov, M.; Whitten, J. E. Abnormal Pinning of the Fermi and Vacuum Levels in Monomolecular Self-Assembled Films. *Chem. Phys. Lett.* **2006**, *428*, 283-287.

(149) Ge, Y.; Weidner, T.; Ahn, H.; Whitten, J. E.; Zharnikov, M. Energy Level Pinning in Self-Assembled Alkanethiol Monolayers. *J. Phys. Chem. C* **2009**, *113*, 4575–4583.

(150) Ballav, N.; Terfort, A.; Zharnikov, M. Mixing of Non-Substituted and Partly Fluorinated Alkanethiols in a Binary Self-Assembled Monolayer. *J. Phys. Chem. C* **2009**, *113*, 3697-3706.

(151) Venkataraman, N. V.; Zürcher, S.; Rossi, A.; Lee, S.; Naujoks, N.; Spencer, N. D. Spatial Tuning of the Metal Work Function by Means of Alkanethiol and Fluorinated Alkanethiol Gradients. *J. Phys. Chem. C* **2009**, *113*, 5620–5628.

(152) Campbell, I. H.; Rubin, S.; Zawodzinski, T. A.; Kress, J. D.; Martin, R. L.; Smith, D. L.; Barashkov, N. N.; Ferraris, J. P. Controlling Schottky Energy Barriers in Organic Electronic Devices Using Self-Assembled Monolayers. *Phys. Rev. B* **1996**, *54*, R14321-R14324.

(153) Thome, J.; Himmelhaus, M.; Zharnikov, M.; Grunze, M. Increased Lateral Density in Alkanethiolate Films on Gold by Mercury Adsorption. *Langmuir* **1998**, *14*, 7435–7449.

(154) Walczak, M. M.; Chung, C.; Stole, S. M.; Widrig, C. A.; Porter, M. D. Structure and Interfacial Properties of Spontaneously Adsorbed n-Alkanethiolate Monolayers on Evaporated Silver Surfaces, *J. Am. Chem. Soc*. **1991**, *113*, 2370-2378.

(155) Dannenberger, O.; Weiss, K.; Himmel, H. J.; Jager, B.; Buck, M.; Wöll, C. An Orientation Analysis of Differently Endgroup-Functionalised Alkanethiols Adsorbed on Au Substrates. *Thin Solid Films* **1997**, *307*, 183-191.

(156) Naselli, C.; Swalen, J. D.; Rabolt, J. F. Order-Disorder Transition in Langmuir-Blodgett Films. IV Structure of $[F(CF2)_8(CH_2)_{10}COO\text{-}]_2Cd^{2+}$ Multilayers at ambient and elevated temperatures. *J. Chem. Phys.* **1989**, *90*, 3855-3860.

(157) Rabolt, J. F.; Falconi, B. Raman Scattering from Finite Polytetrafluoroethylene Chains and a Highly Oriented TFE-HFP Copolymer Monofilament, *Macromolecules* **1978**, *11*, 740-745.

(158) Snyder, R. G. Vibrational Spectra of Crystalline n-Paraffins. Part I. Methylene Rocking and Wagging Modes. *J. Mol. Spectr.* **1960**, *4*, 411-434.

(159) Greenler, R. G. Infrared Study of Adsorbed Molecules on Metal Surfaces by Reflection Techniques. *J. Chem. Phys.* **1966**, *44*, 310-315.

(160) Ohta, T.; Seki, K.; Yokoyama, T.; Morisada, I.; Edamatsu, K. Polarized XAN ES Studies of Oriented Polyethylene and Fluorinated Polyethylenes. *Phys. Scr.* **1990**, *41*, 150-153.

(161) Castner, D. G.; Lewis, K. B.; Fischer, D. A.; Ratner, B. D.; Gland, J. L. Determination of Surface-Structure and Orientation of Polymerized Tetrafluoroethylene Films by Near-Edge X-Ray Absorption Fine-Structure, X-Ray Photoelectron-Spectroscopy, and Static Secondary Ion Mass-Spectrometry. *Langmuir* **1993**, *9*, 537-542.

(162) Genzler, J.; Efimenko, K.; Fischer, D. A. Molecular Orientation and Grafting Density in Semifluorinated Self-Assembled Monolayers of Mono-, Di-, and Trichloro Silanes on Silica Substrates. *Langmuir* **2002**, *18*, 9307-9311.

(163) Farmer, B. L.; Eby, R. K. Energy Calculations of the Crystal Structure of the Low Temperature Phase (II) of Polytetrafluoroethylene. *Polymer* **1981**, *22*, 1487-1495.

(164) Farmer, B. L.; Eby, R. K. Energy Calculations for the Crystal Structure of the High Temperature Phases (I and IV) of Poly(tetrafluoroethylene). *Polymer* **1985**, *26*, 1944-1952.

(165) Gamble, L. J.; Ravel, B.; Fischer, D. A.; Castner, D. G. Surface Structure and Orientation of PTFE Films Determined by Experimental and FEFF8-Calculated NEXAFS Spectra. *Langmuir* **2002**, *18*, 2183-2189.

(166) Ziegler, Ch.; Schedel-Niedrig, Th.; Beamson, G.; Clark, D. T.; Salaneck, W. R.; Sotobayashi, H.; Bradshaw, A. M. X-ray Absorption Study of Highly Oriented Poly(tetrafluoroethylene) Thin Films. *Langmuir* **1994**, *10*, 4399-4402.

(167) Clark, E. S.; Muus, L. T. Partial Disordering and Crystal Transitions in Polytetrafluoroethylene. *Z. Kristallogr*. **1962**, *117*, 119-127.

(168) Piseri, L.; Powell, B. M.; Dolling, G. Lattice Dynamics of Polytetrafluoroethylene. *J. Chem. Phys*. **1973**, *58*, 158-171.

(169) Wunderlich, B. *Macromolecular Physics*; Academic Press: New York and London, 1973.

(170) Dixon, D. A.; Van-Catledge, F. A. A Molecular-Model for the Helicity of Polytetrafluoroethylene (Teflon®). *Internat. J. Supercomput. Appl.* **1988**, *2*, 62-81.

(171) Dishner, M. H.; Hemminger, J. C.; Feher, F. J. Scanning Tunneling Microscopy Characterization of Organoselenium Monolayers on Au(111). *Langmuir* **1997**, *13*, 4788-4790.

(172) Bandyopadhyay, K.; Vijayamohanan, K. Formation of a Self-Assembled Monolayer of Diphenyl Diselenide on Polycrystalline Gold. *Langmuir* **1998**, *14*, 625-629.

(173) Huang, F. K.; Horton, R. C., Jr.; Myles, D. C.; Myles, D. C.; Garrell, R. L. Selenolates as Alternatives to Thiolates for Self-Assembled Monolayers: A SERS Study. *Langmuir* **1998**, *14*, 4802-4808.

(174) Bandyopadhyay, K.; Vijayamohanan, K.; Venkataramanan, M.; Pradeep, T. Self-Assembled Monolayers of Small Aromatic Disulfide and Diselenide Molecules on Polycrystalline Gold Films: A Comparative Study of the Geometrical Constraint Using Temperature-Dependent Surface-Enhanced Raman Spectroscopy, X-ray Photoelectron Spectroscopy, and Electrochemistry. *Langmuir* **1999**, *15*, 5314-5422.

(175) Nakano, K.; Sato, T.; Tazaki, M.; Takagi, M. Self-Assembled Monolayer Formation from Decaneselenol on Polycrystalline Gold As Characterized by Electrochemical Measurements, Quartz-Crystal Microbalance, XPS, and IR Spectroscopy. *Langmuir* **2000**, *16*, 2225-2229.

(176) Han, S. W.; Lee, S. J.; Kim, K. Self-Assembled Monolayers of Aromatic Thiol and Selenol on Silver: Comparative Study of Adsorptivity and Stability. *Langmuir* **2001**, *17*, 6981-6987.

(177) Han, S. W.; Kim, K. Self-Assembled Monolayers of Organoselenium Compounds on Gold: Surface-Enhanced Raman Scattering Study. *J. Colloid Interface Sci.* **2001**, *240*, 492-497.

(178) Yee, C. K.; Ulman, A.; Ruiz, J. D.; Parikh, A.; White, H.; Rafailovich, M. Alkyl Selenide- and Alkyl Thiolate-Functionalized Gold Nanoparticles: Chain Packing and Bond Nature. *Langmuir* **2003**, *19*, 9450-9458.

(179) Sato, Y.; Mizutani, F. Formation and Characterization of Aromatic Selenol and Thiol Monolayers on Gold: In-Situ IR Studies and Electrochemical Measurements. *Phys. Chem. Chem. Phys.* **2004**, *6*, 1328-1331.

(180) Monnell, J. D.; Stapleton, J. J.; Jackiw, J. J.; Dunbar, T.; Reinerth, W. A.; Dirk, S. M.; Tour, J. M.; Allara, D. L.; Weiss, P. S. Ordered Local Domain Structures of Decaneselenolate and Dodecaneselenolate Monolayers on Au{111}. *J. Phys. Chem. B* **2004**, *108*, 9834-9841.

Appendix

A1: Synthesis of the FnH11SH compounds

The syntheses of the respective thiols mostly have been published,[77,78] but were conducted with some alterations significant enough to be discussed here. For F6H11SH and F8H11SH, compounds with the respective carbon backbone were commercially available carrying a double bond in the vicinity of the perfluoroalkyl chain ($F_nCH=CH(CH_2)_9OH$). This double bond could be hydrogenated in the presence of PtO_2 (Pd on carbon did not work). To activate the carbon atom in 1-position, it was transformed into the respective alkyliodide using phosphorus and iodine. For comparison, the formation of the alkylbromide using PBr_3 did not work out satisfactorily in our hands. The alkyliodides were reacted with thioacetate to form the alkyl thioacetates of which one (F8H11SH) directly was transformed into the thiol under the work-up conditions. For the other thioacetate, a separate hydrolysis step had to be performed.

Since no similar starting material was available for the preparation of F10H11SH, we decided to use a protocol developed by Lee et al.,[78] in which the commercially available perfluorodecyliodide (F10I) was coupled with undec-10-enylthioacetate via a radical addition reaction. To remove the iodine atom, we substituted the toxic tin compound suggested in ref 1 by lithium tetrahydridoaluminate, which not only resulted in the replacement of the iodine atome by a hydrogen atom, but also in the removal of the acetyl group (see scheme below). The physical data of all the compounds fitted the ones given in the literature.[77,78]

Syntheses of F6H11SH and F8H11SH:

Hydrogenation of the 11-(perfluoro-n-hexyl)undec-10-en-1-ol and 11-(perfluoro-n-octyl)undec-10-en-1-ol:

The respective 11-(perfluoro-n-alkyl)undec-10-en-1-ol (5-6 mmol) was hydrogenated in absolute THF (50 ml) in the presence of PtO_2 (80 mg) for 16 h at r.t. and a hydrogen pressure of 100 kPa. After filtration, the solvent was removed under reduced pressure to yield the colorless products (87% for the perfluorohexylderivative, 91% for the perfluorooctyl derivative), which were pure enough for the next step.

1-Iodo-11-(perfluoro-n-hexyl)undecane and 1-iodo-11-(perfluoro-n-octyl)undecane:

To the respective perfluoroalkylundecanol (5 mmol) red phosphorus (64 mg, 2.0 mmol) and iodine (0.66 g, 5.2 mmol) were added and the mixture was heated to 140 °C for 5 h. After

cooling, the product mixture was dissolved in diethyl ether and filtered through a pad of alumina. After removal of the solvent, the products were obtained as colorless solids (91% for the perfluorohexylderivative, 85% for the perfluorooctyl derivative), which were pure enough for the next step.

11-(Perfluoro-n-hexyl)undecan-1-thiol and 11-(perfluoro-n-octyl)undecan-1-thiol via the thioacetates:

To elemental sodium (0.16 g, 7.0 mmol) methanol (20 ml) was cautiously dropped under an atmosphere of nitrogen. After completion of the reaction, thioacetic acid (1.06 ml, 15.0 mmol) was added, followed by iodo compounds (~4.5 mmol). The resulting mixture was heated to 70 °C for 18 h, before the volatiles were removed *in vacuo*. The remaining yellow solid was dissolved in diethyl ether and filtered through a pad of silica and the solvent was removed *in vacuo*.

At this point, it turned out that in case of the perfluorooctyl derivative, the acetyl group was cleaved under the reaction conditions. This material therefore was directly purified by column chromatography (see below).

The perfluorohexylundecyl thioacetate (yellowish oil, 84%) was reacted with NaOH (0.24 g, 6.0 mmol) in methanol (20 ml) at reflux temperature under rigorous exclusion of air. After acidification with conc. HCl (3 ml), the volatiles were removed *in vacuo* and remaining material was chromatographed on silica using a gradient starting from cyclohexane/dichloromethane 99/1 to obtain the products.

F6H11SH: colorless oil, 93%, ^{1}H NMR ($CDCl_3$, 200 MHz): δ/ppm = 1.20-1.48 (m, 15H, $(C\mathbf{H}_2)_7$ and S**H**), 1.51-1.72 (m, 4H, $C\mathbf{H}_2CH_2SH$ and $C\mathbf{H}_2CH_2CF_2$), 1.88-2.24 (m, 2H, $C\mathbf{H}_2CF_2$), 2.54 (q, 2H, *J*=7.3 Hz, $C\mathbf{H}_2SH$); MS (EI): m/z = 505 (4%, $[M-H]^+$), 472 (100%, $[M-H_2S]^+$), 55 (92%, $[C_4H_7]^+$).

F8H11SH: colorless solid, 88%, mp 46-47.5 °C (49.7 °C)[77], ^{1}H NMR ($CDCl_3$, 200 MHz): δ/ppm = 1.21-1.48 (m, 15H, $(C\mathbf{H}_2)_7$ and S**H**), 1.55-1.70 (m, 6H, $C\mathbf{H}_2CH_2SH$, $C\mathbf{H}_2CH_2CF_2$, and $C\mathbf{H}_2CF_2$), 2.54 (q, 2H, *J*=7.4 Hz, $C\mathbf{H}_2SH$); MS (EI): m/z = 605 (6%, $[M-H]^+$), 572 (100%, $[M-H_2S]^+$), 55 (64%, $[C_4H_7]^+$).

Synthesis of F10H11SH:

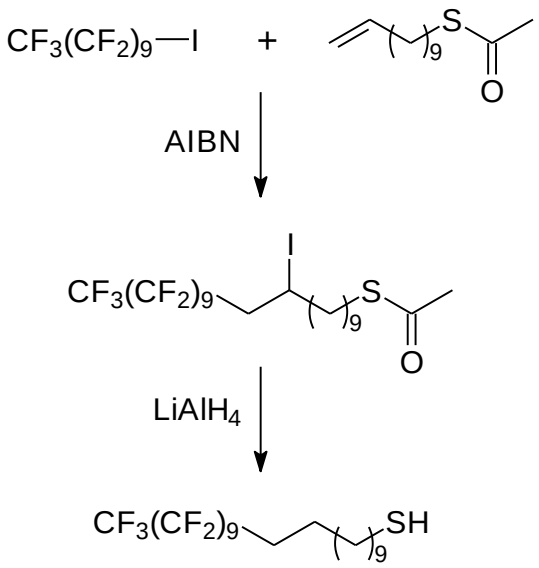

To a mixture of perfluorodecyl-1-iodide (3.55 g, 5.5 mmol) and undec-11-enyl-1-thioacetate (1.14 g, 5 mmol) in a 10 mL Schlenk tube azoisobutyronitrile (AIBN, 10 mg) was added, before the mixture was heated to 90 °C under N_2 for a total of 30 h. The addition of AIBN (10 mg each) was repeated every 3 h.

After cooling, the reaction mixture was dissolved in THF and added dropwise to a suspension of $LiAlH_4$ (0.48 g, 13 mmol) in THF (25 ml) at room temperature. After the mixture was stirred at 50 °C for 16 h, it was quenched with dil. HCl and the THF was removed by rotary evaporation. The product was extracted three times from the heterogeneous mixture with CH_2Cl_2, the organic extracts were washed with water and concentrated *in vacuo*. The crude product was chromatographed on silica using a gradient starting from hexane/dichloromethane 50/1 to obtain a colorless solid (2.0 g, 2.8 mmol, 56%).

F10H11SH: mp 71-72 °C (73.4 °C)[77], ^{1}H NMR ($CDCl_3$, 200 MHz): δ/ppm = 1.24-1.43 (m, 15H, (C**H**$_2$)$_7$ and S**H**), 1.53-1.78 (m, 4H, C**H**$_2$CH$_2$SH and C**H**$_2$CH$_2$CF$_2$), 1.85-2.32 (m, 2H, C**H**$_2$CF$_2$), 2.52 (q, 2H, *J*=7.4 Hz, C**H**$_2$SH).

A2: Additional IR dataset for FnH11SH SAMs on Au

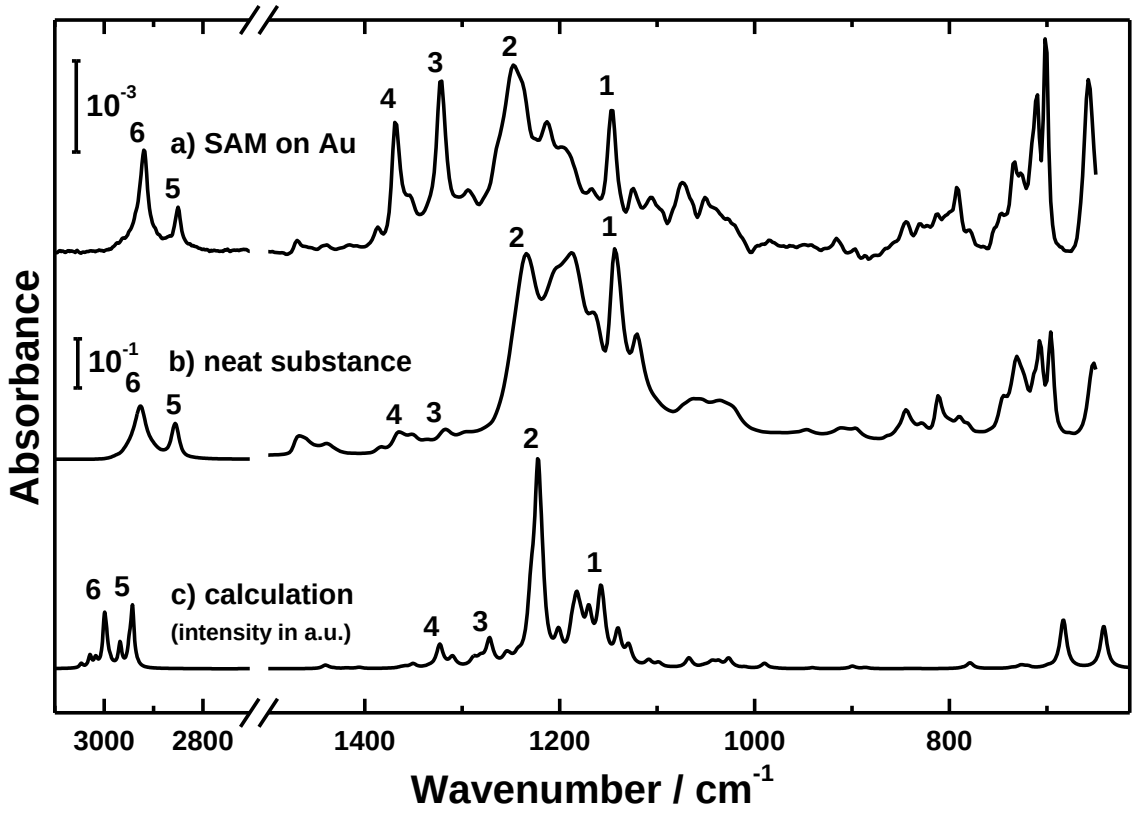

Figure S1: IR spectra of the F6H11SH species. a) IRRA spectrum of the F6H11SH SAM on Au. b) Spectrum of the neat substance, recorded with an ATR unit. c) Spectrum of an isolated molecule, calculated with DFT. Two scale bars indicate the absorbance intensities of the experimental spectra. A couple of bands are marked with numbers. See Table S1 for details.

Table S1. Infrared vibrational modes of F6H11SH, along with the respective assignments. Wavenumbers are given in cm^{-1}.

	mode assignment[a]	IRRAS[b]	neat substance[b]	DFT	TDM[c]
1	ν as CF_2 ω CH_2	1146 s	1143 vs	1158	almost perpendicular to helical axis
2	ν as CF_3 ν as CF_2 τ CH_2	1247 s	1234 vs	1220	almost perpendicular to helical axis
3	ν s CF_2 ν s CF_3	1322 s	1317 m	1272	almost parallel to helical axis
4	ν s CF_2 ν CC helix	1368 s	1365 m	1323	almost parallel to helical axis
5	ν s CH_2	2850 m	2856 m	2943	parallel to CCC backbone plane
6	ν as CH_2	2919 m	2926 m	2998	perpendicular to CCC backbone plane

a) Abbreviations used: ν-stretch, τ-torsion, ω-wagging; as-asymmetric, s-symmetric

b) Abbreviations used: vs-very strong, s-strong, m-medium, w-weak

c) Information on the direction of the vibrational mode's transition dipole moment

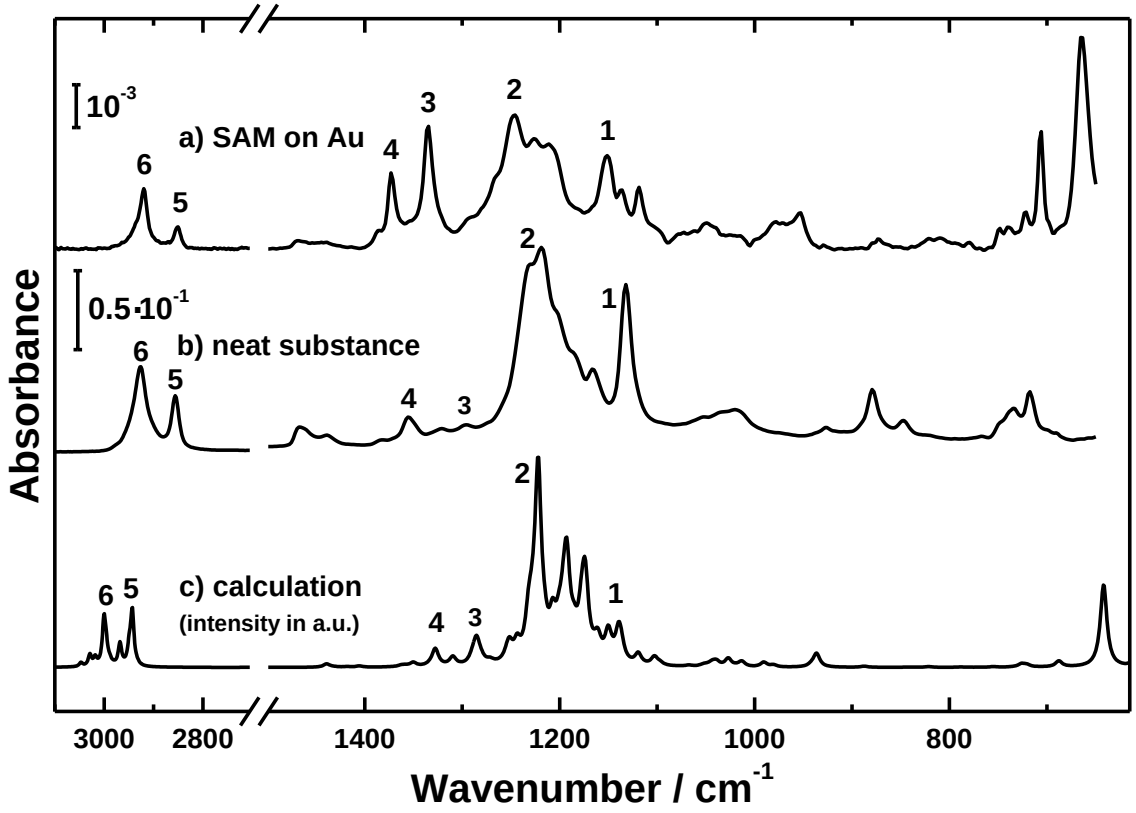

Figure S2: IR spectra of the F8H11SH species. a) IRRA spectrum of the F8H11SH SAM on Au. b) Spectrum of the neat substance, recorded with an ATR unit. c) Spectrum of an isolated molecule, calculated with DFT. Two scale bars indicate the absorbance intensities of the experimental spectra. A couple of bands are marked with numbers. See Table S2 for details.

Table S2. Infrared vibrational modes of F8H11SH, along with the respective assignments. Wavenumbers are given in cm^{-1}.

	mode assignment[a]	IRRAS[b]	neat substance[b]	DFT	TDM[c]
1	ν as CF_2 ω CH_2	1151 m	1166 m	1161	almost perpendicular to helical axis
2	ν as CF_3 ν as CF_2 ω CH_2	1246 s	1231 vs sh	1222	almost perpendicular to helical axis
3	ν s CF_2 ν s CF_3 ν CC helix	1335 s	1321 m	1285	almost parallel to helical axis
4	ν s CF_2 ν s CF_3 ν CC helix	1373 m	1355 m	1328	almost parallel to helical axis
5	ν s CH_2	2851 m	2856 m	2943	parallel to CCC backbone plane
6	ν as CH_2	2920 m	2926 m	3000	perpendicular to CCC backbone plane

a) Abbreviations used: ν-stretch, τ-torsion, ω-wagging; as-asymmetric, s-symmetric

b) Abbreviations used: vs-very strong, s-strong, m-medium, w-weak, sh-shoulder

c) Information on the direction of the vibrational mode's transition dipole moment

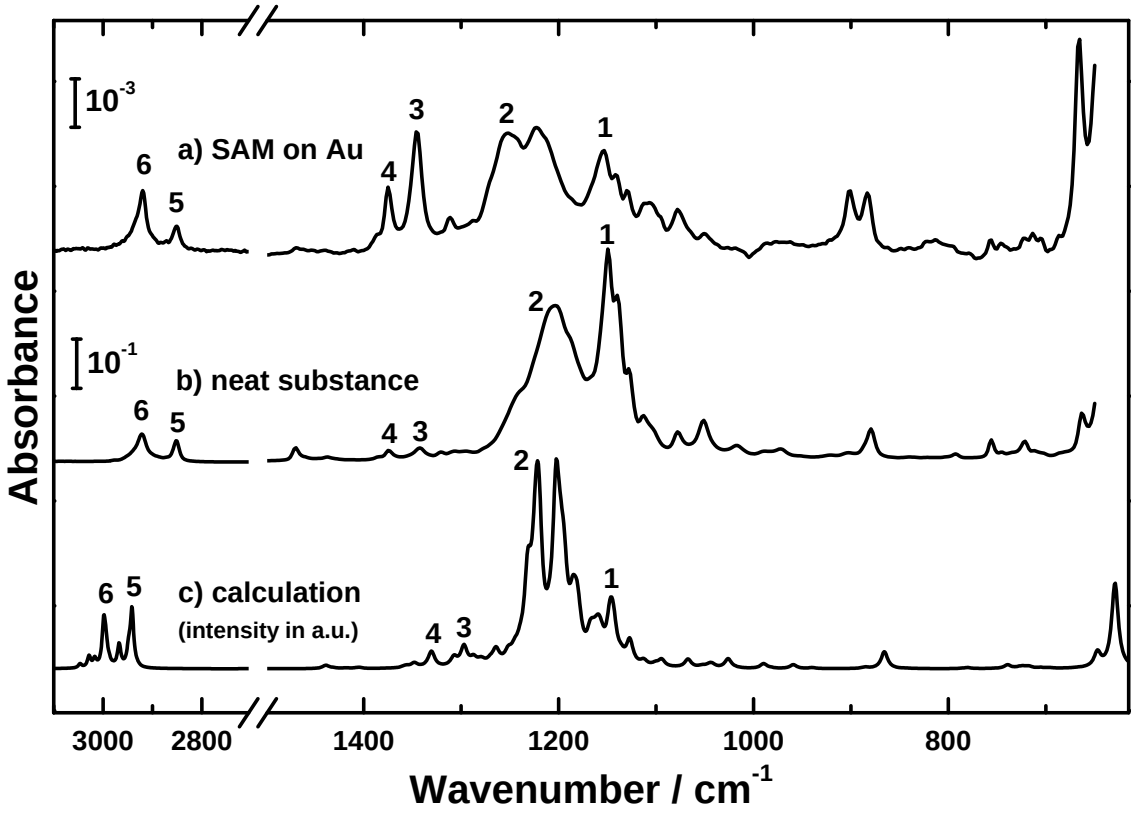

Figure S3: IR spectra of the F10H11SH species. a) IRRA spectrum of the F10H11SH SAM on Au. b) Spectrum of the neat substance, recorded with an ATR unit. c) Spectrum of an isolated molecule, calculated with DFT. Two scale bars indicate the absorbance intensities of the experimental spectra. A couple of bands are marked with numbers. See Table S3 for details.

Table S3. Infrared vibrational modes of F10H11SH, along with the respective assignments. Wavenumbers are given in cm^{-1}.

	mode assignment[a]	IRRAS[b]	neat substance[b]	DFT	TDM[c]
1	ν as CF_2 ω CH_2 τ CH_2	1154 m	1149 vs	1146	almost perpendicular to helical axis
2	ν as CF_3 ν as CF_2 ω CH_2 τ CH_2	1252 s	1240 m sh	1226	almost perpendicular to helical axis
3	ν s CF_2 ν s CF_3 ν CC helix	1345 s	1342 w	1297	almost parallel to helical axis
4	ν s CF_2 ν CC helix	1375 m	1374 w	1330	almost parallel to helical axis
5	ν s CH_2	2851 m	2851 w	2941	parallel to CCC backbone plane
6	ν as CH_2	2920 m	2921 m	2999	perpendicular to CCC backbone plane

a) Abbreviations used: ν-stretch, τ-torsion, ω-wagging; as-asymmetric, s-symmetric

b) Abbreviations used: vs-very strong, s-strong, m-medium, w-weak, sh-shoulder

c) Information on the direction of the vibrational mode's transition dipole moment

A3: Abbreviations

AT	Alkanethiol
ATs	Alkanethiols
BE	Binding Energy
BPn	ω-(4´-methyl-biphenyl-4-yl)-alkanethiols, $CH_3(C_6H_4)_2(CH_2)_nSH$ (n=1 − 6)
C16Se	Dihexadecyl Diselenide, $C_{16}H_{33}SeSeC_{16}H_{33}$
C16SH	Hexadecanethiol, $C_{16}H_{33}SH$
DDT	Dodecanethiol, $C_{12}H_{25}SH$
FnH11SH	$CF_3(CF_2)_{n-1}(CH_2)_{11}SH$
fwhm	full width at half-maximum
HDT	Hexadecanethiol, $C_{16}H_{33}SH$
HRXPS	High Resolution XPS
IRRAS	InfraRed Reflection Absorption Spectroscopy
KE	Kinetic Energy
NEXAFS	Near Edge X-ray Absorption Fine Structure
NSAT	Non-substituted Alkanethiol
NSATs	Non-substituted Alkanethiols
ODT	Octadecanethiol, $C_{18}H_{37}SH$
PE	Photon Energy
PFAT	Partially Fluorinated Alkanethiols
PTFE	Poly(tetrafluoroethylene)
rms	Root mean square
SAM	Self-Assembled Monolayer
SAMs	Self-Assembled Monolayers
TDM	Transition Dipole Moment
TDMs	Transition Dipole Moments
TPn	4,4´-terphenyl-substituted alkanethiols, $C_6H_5(C_6H_4)_2(CH_2)_nSH$ (n=0 − 6)
XPS	X-ray Photoelectron Spectroscopy
vdW	Van der Waals

A4: List of Figures

Figure 1.1: Schematic diagram of an ideal, single-crystalline SAM of alkanethiolates supported on a gold surface with a (111) texture. 1

Figure 1.2: Schematic drawing of the orientation and packing of the terphenyl-substituted AT SAMs on Au and Ag. 3

Figure 1.3: Lattice structure of ODT SAM on GaAs (001). 5

Scheme 1.1: The structures of the TPn (n=0-6), and BPn (n=1-6) precursors. 6

Scheme 1.2: The structures of the FnH11SH SAM precursors. 6

Scheme 1.3: Molecular structure of C16Se and C16SH. 6

Figure 2.1: C 1s HRXPS of F10H11SH SAM on GaAs (001). 9

Figure 2.2: The effect of inelastic collisions of electrons in the substrate on the XPS signal. 10

Figure 2.3: Quantitative calculation for the intensity of the attenuated XPS signal (Beer's law). 11

Figure 2.4: Schematic representation of an ARXPS measurement. 12

Figure 2.5 a: Schematic representation of the processes occurring during a NEXAFS experiment; b: Schematic representation of the different NEXAFS measurement methods. 13

Figure 2.6: Schematic representation of the interaction of X-rays with π^* and σ^* orbitals of a diatomic molecule. 14

Figure 2.7: Schematic setup of an ellipsometry experiment. 15

Figure 2.8a: Schematic representation of a drop on a surface; b: Schematic representation of the advancing contact angle. 16

Figure 3.1: AFM contacting mode topography of the GaAs(001) surface before and after etching. 18

Figure 3.2: A schematic diagram of an XPS spectrometer. 20

Figure 4.1: As 3d and Ga 3d HRXPS spectra of ODT SAM on GaAs (001) and the etched GaAs. 25

Figure 4.2: As 3d and Ga 3d HRXPS spectra of ODT SAM on GaAs (001). The spectra were acquired at PEs of 130 and 300eV. 26

Figure 4.3: S 2p, O 1s and C 1s HRXPS spectra of ODT SAM on GaAs(001). 28

Figure 4.4: C K-edge NEXAFS spectra of ODT/GaAs SAM acquired at X-ray incidence angles of 90°, 55°, and 20°, along with the difference spectra. 29

Figure 4.5: The angular dependence of the intensity ratios for the R^* resonance for ODT/GaAs SAM, along with the best theoretical fits. 30

Figure 4.6: Plots of the intensities of the C-C σ^* difference peaks for HDT/Au and ODT/GaAs

SAMs versus $\cos^2\theta$-$\cos^2$ (55°) along with the respective linear fits using least-squares analysis. 31

Figure 4.7: IRRAS spectra of the C-H stretching region for an ODT monolayer on GaAs (001). 31

Figure 4.8: As 3d and Ga 3d HRXPS spectra of HDT SAM on GaAs(001). 33

Figure 4.9: S 2p, O 1s and C 1s HRXPS spectra of HDT SAM on GaAs(001). 34

Figure 4.10: C K-edge NEXAFS spectra of HDT/GaAs SAM acquired at X-ray incidence angles of 90°, 55°, and 20°, along with the difference spectra. 34

Figure 4.11: As 3d and Ga 3d XPS spectra of DDT SAMs on GaAs(001) prepared with different etching time. 35

Figure 4.12: C 1s XPS spectra of ODT, HDT and DDT SAMs on GaAs(001). 35

Figure 4.13: C 1s XPS spectra of DDT SAMs on GaAs(001) prepared under different incubation time. 36

Figure 4.14: C 1s XPS spectra of DDT SAMs on GaAs(001) prepared with different ammonia concentration in the target solutions. 36

Figure 5.1: As 3d and Ga 3d HRXPS spectra of TPT SAMs on GaAs (001) prepared with different experimental setup. 42

Figure 5.2: As 3d and Ga 3d HRXPS spectra of TPT SAMs on GaAs (001) prepared with different etching methods. 42

Figure 5.3: S 2p HRXPS spectra of TP3 SAMs on GaAs (001) using different rinsing methods. 43

Figure 5.4: As 3d and Ga 3d HRXPS spectra of TPn and TP1-CN SAMs on GaAs(001). 45

Figure 5.5: S 2p and C 1s HRXPS spectra of TPn and TP1-CN SAMs on GaAs(001). 47

Figure 5.6: O 1s HRXPS spectra of TPn SAMs on GaAs(001). 47

Figure 5.7: C K-edge NEXAFS spectra of TP5 SAM on GaAs (001) acquired at an X-ray incident angle of 55°. 47

Figure 5.8: C K-edge NEXAFS spectra of TPn SAMs on GaAs (001) acquired at an X-ray incident angle of 55° as well as at normal (90°) and grazing (20°) incidence of X-rays. 48

Figure 5.9: C K-edge NEXAFS spectra of TP5 SAM on GaAs (001) acquired at an X-ray incident angle of 55° along with the respective fit. 49

Figure 5.10: The angular dependence of the π_1^* resonance intensity ratios for TP5 SAM on GaAs (001), along with the best theoretical fits. 50

Figure 5.11: Carbon K-edge and Nitrogen K-edge NEXAFS spectra of TP1-CN SAM on GaAs (001) acquired at X-ray incidence angles of 90°, 55° and 20°. 51

Figure 5.12: odd-even variation of packing density and molecular orientation in TPn SAMs on GaAs (001). 54

Figure 5.13: odd-even variation of packing density in TPn SAMs on Au. 56

Figure 5.14: As 3d and Ga 3d HRXPS spectra of BPn SAMs on GaAs(001). 59

Figure 5.15: S 2p and C 1s HRXPS spectra of BPn SAMs on GaAs(001). 60

Figure 5.16: the intensities of the S 2p emission of BPn SAMs on GaAs (001). 61

Figure 5.17: O 1s HRXPS spectra of BPn SAMs on GaAs(001). 61

Figure 5.18: C K-edge NEXAFS spectra of BPn SAMs on GaAs (001) acquired at an X-ray incident angle of 55° as well as at normal (90°) and grazing (20°) incidence of X-rays. 62

Figure 5.19: Average tilt angles of biphenyl moieties in BPn/GaAs (001) SAMs. 63

Figure 5.20: The HRXPS-derived effective thickness of BPn SAMs on GaAs (001). 63

Figure 6.1: S 2p HRXPS spectra of the FnH11SH SAMs on Au. 69

Figure 6.2: C 1s HRXPS spectra of the FnH11SH SAMs on Au. 69

Figure 6.3: C 1s HRXPS and XPS spectra of the F10H11SH SAM on Au acquired at different photon energies. 70

Figure 6.4: F 1s HRXPS spectra of the FnH11SH SAMs on Au. 70

Figure 6.5: IR spectra of the FnH11SH SAMs on Au in the range characteristic of the CF_2 vibrations, along with the spectrum of the neat F10H11SH substance and the theoretical spectrum of isolated F10H11SH molecule, calculated using DFT. 73

Figure 6.6: IR spectra of the FnH11SH SAMs on Au acquired in the C-H stretching region. 75

Figure 6.7: C K-edge NEXAFS spectra of the FnH11SH SAMs on Au acquired at an X-ray incident angle of 55°. 77

Figure 6.8: F K-edge NEXAFS spectra of the FnH11SH SAMs on Au acquired at an X-ray incident angle of 55°. 77

Figure 6.9: Difference between the C K-edge NEXAFS spectra of the FnH11SH SAMs on Au acquired at the normal (90°) and grazing (20°) incidence of X-rays. 77

Figure 6.10: A fit of the C K-edge NEXAFS spectra (55°) of F10H11SH SAM on Au. 79

Figure 6.11: The angular dependence of the I(θ)/I(90°) intensity ratios for the R^* and C–F σ* resonances for the FnH11SH SAMs on Au, along with the best theoretical fits. 79

Figure 6.12: Schematic drawing of the molecular orientation in the FnH11SH SAMs on Au. 80

Figure 7.1: As 3d and Ga 3d HRXPS spectra of FnH11SH and ODT SAMs on GaAs (001). 85

Figure 7.2: S 2p, O 1s, F 1s HRXPS spectra of the FnH11SH SAMs on GaAs (001). 87

Figure 7.3: C1s HRXPS spectra of the FnH11SH SAMs on GaAs (001). 88

Figure 7.4: IR spectra of the F10H11SH SAM on GaAs (001) in the range characteristic of the CF_2 vibrations. 91

Figure 7.5: Carbon K-edge and Fluorine K-edge NEXAFS spectra of the FnH11SH SAMs on GaAs (001) acquired at an X-ray incident angle of 55°. 92
Figure 7.6: Difference between the Carbon K-edge NEXAFS spectra of the FnH11SH SAMs on GaAs (001) at the normal (90°) and grazing (20°) incidence of X-rays. 94
Figure 7.7: The angular dependence of the I(θ)/I(90°) intensity ratios for the R^* and C–F σ* resonances for the FnH11SH SAMs on GaAs (001), along with the best theoretical fits. 94
Figure 7.8: Schematic drawing of the molecular orientation in the FnH11SH SAMs on GaAs (001). 96
Figure 8.1: As 3d HRXPS spectra of C16Se and C16SH SAMs on GaAs (001). 102
Figure 8.2: Ga 3d HRXPS spectra of C16Se and C16SH SAMs on GaAs (001). 102
Figure 8.3: Se 3d and C 1s HRXPS spectra of C16Se SAM on GaAs(001). 103
Figure 8.4: Carbon K-edge NEXAFS spectra of C16Se/GaAs SAM acquired at different X-ray incidence, along with the difference (C16SH/GaAs included) between the 90° and 20° spectra. 104
Figure 8.5: The angular dependence of the R^* resonance intensity ratio I(θ)/I(20°) for C16SH/GaAs and C16Se/GaAs SAMs along with the best theoretical fits. 105

A5: List of Tables

Table 4.1: Parameters of Individual Emissions in the Ga 3d and As 3d HRXPS spectra of ODT SAM on GaAs (001). 27

Table 4.2: Advancing and Static Contact Angles of NSAT SAMs on GaAs (001). 33

Table 5.1: Parameters of Individual Emissions in the Ga 3d and As 3d HRXPS Spectra of TPn SAMs on GaAs (001). 45

Table 5.2: Assignments and Positions of the Characteristic NEXAFS Resonances in TPn/GaAs (001). 48

Table 5.3 Tilt and Twist Angles (°) of TP1-CN SAMs on GaAs (001) and Au. 52

Table 6.1: Infrared Vibrational Modes of FnH11SH SAMs, along with the respective assignments. 74

Table 7.1: F 1s Binding Energy Positions for FnH11SH SAMs on GaAs(001) and Au(111). 88

Table 8.1. Binding Energy Positions and fwhm's of the Photoemission Peaks for C16Se and C16SH SAMs on GaAs (001). 103

A6: List of Publications in PhD Period

Journals:

- Lu, H.; Terfort, A.; Zharnikov, M. Bending Potential as an Important Factor for the Structure of Monomolecular Thiolate Layers on GaAs Substrates. *J. Phys. Chem. Lett.* **2013**, *4*, 2217-2222.
- Lu, H.; Zeysing, D.; Kind, M.; Terfort, A.; Zharnikov, M. Structure of Self-Assembled Monolayers of Partially Fluorinated Alkanethiols with a Fluorocarbon Part of Variable Length on Gold Substrate. *J. Phys. Chem. C* **2013**, *117*, 18967−18979.
- Cebula, I.; Lu, H.; Zharnikov, M.; Buck, M. Monolayers of Trimesic and Isophthalic Acid on Cu and Ag: the Influence of Coordination Strength on Adsorption Geometry. accepted by *Chem. Sci.*

- Lu, H.; Terfort, A.; Zharnikov, M. Structure of Self-Assembled Monolayers of Partially Fluorinated Alkanethiols on GaAs (001) Substrate. (manuscript in preparation)
- Lu, H.; Zharnikov, M. Effect of Bending Potential on Molecular Arrangement in Biphenyl-Substituted Alkanethiol Self-Assembled Monolayers on GaAs (001). (manuscript in preparation)

Conference:

Lu, H.; Terfort, A.; Zharnikov, M. Self-Assembled Monolayers of Partially Fluorinated Alkanethiols on Gold and GaAs (001) Substrates. DPG meeting, March 2013, Regensburg, Germany

Acknowledgement

First of all, I would like to express my appreciation to my supervisor Prof. Michael Zharnikov, for his persistent scientific guidance, numerous discussions of my work, as well as his careful correction of my thesis. During past years, his incisive vision and serious attitude in science have deeply influenced me.

I would like to thank Prof. Michael Grunze for giving me the opportunity to be part of the Angewandte Physikalische Chemie (APC) institute, and also for his generosity and good taste of wine during the Christmas parties.

I would like to thank Prof. Hans-Robert Volpp for agreeing to review this thesis work, as well as to be my second examiner.

I would like to thank Prof. Andreas Terfort from Goethe-Universität Frankfurt and Prof. Manfred Buck from University of St Andrews for supplying me the valuable, synthesized chemical compounds to finish this thesis. Thanks also go to Dr. Martin Kind for the DFT calculation for the IR spectra relevant to this thesis.

I am thankful to the current and past members of our Surface Science & Analytics research group for their help and scientific discussions. In particular, I would like to thank Dr. Jianli Zhao who helped me a lot when I just arrived Germany, and Dr. Nikolaus Meyerbröker who helped me to solve different problems of the XPS (Max-200) instrument and also translated the abstract to German in this thesis.

I would like to thank my colleagues at the APC institute, past and present, for making my stay in Heidelberg pleasant and broadening my scientific horizons. Thanks also go to all the support staff in APC institute who have helped me in one way or another.

I would like to thank all my friends in Heidelberg; especially those with me for lunch together, I will remember all of you (Yang, Weibo, Tuo, Tao, Shuai, Lei, Hui, Bin, Yanbiao…) and also the nearly fixed table at the mensa, so called “Beijing Table”.

I would like to thank China Scholarship Council for supporting my living expense during my PhD period in Germany.

Finally, I want to express my deepest gratitude to my parents since their encouragement and never-stop confidence for me are the great treasure in my whole life!